



AKADEMIA GÓRNICZO-HUTNICZA IM. STANISŁAWA STASZICA W KRAKOWIE

DZIEDZINA NAUK INŻYNIERYJNO-TECHNICZNYCH

DYSCYPLINA AUTOMATYKA, ELEKTRONIKA I ELEKTROTECHNIKA

ROZPRAWA DOKTORSKA

*Dynamika i przełączanie magnetyzacji indukowane
prądami spinowymi w heterostrukturach metal
ciężki/ferromagnetyk*

Autor: Stanisław Marek Łazarski

Promotor rozprawy: dr hab. inż. Witold Skowroński, prof. AGH

Praca wykonana: Akademia Górniczo-Hutnicza im. Stanisława Staszica w
Krakowie

Wydział Informatyki, Elektroniki i Telekomunikacji
Instytut Elektroniki
Kraków, 2022



AGH UNIVERSITY OF SCIENCE AND TECHNOLOGY

FIELD OF SCIENCE ENGINEERING AND TECHNOLOGY

SCIENTIFIC DISCIPLINE AUTOMATION, ELECTRONIC AND ELECTRICAL
ENGINEERING

DOCTORAL THESIS

*Dynamics and spin-current induced switching in heavy
metal/ferromagnet heterostructures*

Author: Stanisław Marek Łazarski

First supervisor: dr hab. inż. Witold Skowroński, prof. AGH

Completed in: University of Science and Technology AGH,
Faculty of Computer Science, Electronics and Telecommunications, Institute of
Electronics
Kraków, 2022

Stanisław Łazarski

Dynamics and spin-current induced switching in heavy metal / ferromagnet heterostructures

AGH University of Science and Technology

Copyright © 2022 Stanisław Łazarski

AGH UNIVERSITY OF SCIENCE AND TECHNOLOGY
INSTITUTE OF ELECTRONICS

Supervisor:

dr hab. inż. Witold Skowroński, prof. AGH

Declaration

I hereby declare that the work in this thesis is my own original work, except where indicated in the text.

Section *Inductive determination of magnetization dynamics in MTJ structure* is based on the publication: W. Skowroński, **S. Łazarski**, P. Rzeszut, S. Ziętek, J. Chęciński and J. Wrona, *Influence of a composite free layer structure on thermal stability of perpendicular magnetic tunnel junction*, *Journal of Applied Physics* **124**, 063903 (2018). DOI: doi.org/10.1063/1.5032148

Section *Spin orbit torque induced dynamics and switching in Pt/Co/Pt* is based on the publication: **S. Łazarski**, W. Skowroński, J. Kanak, Ł. Karwacki, S. Ziętek, K. Grochot, T. Stobiecki and F. Stobiecki, *Field-Free Spin-Orbit Torque Switching in Co/Pt/Co Multilayer with Mixed Magnetic Anisotropies*, *Physical Review Applied* **12**, 014006 (2019). DOI: [10.1103/PhysRevApplied.12.014006](https://doi.org/10.1103/PhysRevApplied.12.014006).

Section *Magnetization dynamics in CoFeB/Ta/CoFeB system with mixed anisotropy* is based on the publication: **S. Łazarski**, W. Skowroński, W. Powroźnik, J. Kanak, M. Schmidt and T. Stobiecki, *Spin-orbit torque induced magnetisation dynamics and switching in CoFeB/Ta/CoFeB system with mixed magnetic anisotropy*, *Physical Review B* **103**, 134421 (2021). DOI: [10.1103/PhysRevB.103.134421](https://doi.org/10.1103/PhysRevB.103.134421).

Section *Harmonic Hall voltage measurements in Pt-Ti/CoFeB system* is based on the publication: W. Skowroński, K. Grochot, P. Rzeszut, **S. Łazarski**, G. Gajoch, C. Worek, J. Kanak, T. Stobiecki, J. Langer, B. Ocker and M. Vafaei *Angular Harmonic Hall Voltage and Magnetoresistance Measurements of Pt/FeCoB and Pt-Ti/FeCoB Bilayers for Spin Hall Conductivity Determination*, *IEEE Transactions on Electron Devices* **68**, no. 12, p. 6379-5385 (2021). DOI: [10.1109/TED.2021.3122999](https://doi.org/10.1109/TED.2021.3122999)

July 2022

Acknowledgments

I would like to express my sincere gratitude to my supervisor PROF. WITOLD SKOWROŃSKI for his patient guidance, sharing his knowledge and invaluable advice throughout my Ph.D.

Special thanks to PROF. TOMASZ STOBIECKI for introducing me to the world of nanomagnetism and spintronics along with sharing their experience.

My gratitude to DR. ANTONI ŻYWCZAK for showing me the scientific world, as well as for all of our exchanges of views.

I would like to thank all members of the Magnetic Multilayers and Spin Electronics Group: M.Sc. KRZYSZTOF GROCHOT, M.Sc. PIOTR RZESZUT, DR. SŁAWOMIR ZIĘTEK, DR. MONIKA CECOT, DR. MAREK FRANKOWSKI, DR. JAKUB CHĘCIŃSKI, DR. JAROSŁAW KANAK, DR. WIESŁAW POWROŃNIK, DR. MACIEJ CZAPKIEWICZ, DR. ZBIGNIEW SZKLARSKI for their help and encouragement.

The nanofabrication processes were supported by research infrastructure from the Academic Center for Materials and Nanotechnology AGH.

Various parts of this work were supported by the National Science Center Grant No. UMO-2015/17/D/ST3/0050, the National Science Center Grant No. Spinorbitronics UMO-2016/23/B/ST3/01430 and from the Polish National Centre for Research and Development Grant No. LIDER/467/L-6/14/NCBR/2015.

Finally, I would like to dedicate this work to my wife ZUZIA for her endless support, patience and faith. Without her, I would not have the commitment and courage to pursue it.

Streszczenie

Odkrycie nowych zjawisk fizycznych oraz dalszy postęp w zakresie nanotechnologii w szczególności układów cienkowarstwowych umożliwiły rozwój nowej dziedziny nauki: elektroniki spinowej. W elektronice spinowej (lub krócej, w spintronice) wykorzystywane jest sprzężenie spinu elektronu odpowiedzialnego za magnetyzm cienkich warstw z prądem spinowo spolaryzowanym, który umożliwia m. in. zapisywanie, przechowywanie, procesowanie i odczytywanie informacji zakodowanej w postaci namagnesowania.

Przedstawiona praca opisuje wkład w eksperymentalne badania dynamiki namagnesowania w cienkowarstwowych heterostrukturach spintronicznych wykorzystujących metale ciężkie, które charakteryzują się znacznym sprzężeniem spin-orbita w oddziaływaniu z ferromagnetykami. Do niniejszego manuskryptu w całości lub częściowo włączono cztery wcześniej opublikowane artykuły w renomowanych czasopismach naukowych.

Praca ta wprowadza czytelnika w tematykę rozprawy, a następnie przedstawia podstawowe pojęcia niezbędne do zrozumienia funkcjonowania układów wielowarstw spintronicznych, takie jak magnetyczne złącza tunelowe i zawory spinowe, anizotropia magnetyczna, wymienne sprzężenie międzywarstwowe, transfer spinowego momentu siły i spinowo-orbitalny moment siły, magnetorezystancja i zjawiska Halla. Zostały też opisane nieodzowne w pomiarach dynamicznych układów wielowarstwowych formuła Kittel-a jak również równanie Landau-Lifshitz-Gilbert poszerzone o transfer spinowego momentu siły Slonczewskiego. Następnie, na podstawie publikacji, omówiono szereg eksperymentów, które pozwoliły na zbadanie zachowanie dynamiki w różnorodnych układach opartych na magnetycznych złączach tunelowych lub ich części.

W kolejnej części pracy, omówiono podstawy i rezultaty badań nad układami cienkowarstwowymi, które nie wymagają wykorzystania procesu litografii, są to technika rezonansu ferromagnetycznego przy użyciu wektorowego analizatora sieci, jak również metoda magnetometrii wibracyjnej, które są wykorzystywane do pomiarów niektórych własności statycznych i dynamicznych układów wielowarstwowych. Pozwala to na relatywnie szybki wgląd w parametry takie jak stała tłumienia, anizotropia lub sprzężenie wymiany międzywarstwowej. Kolejne metody pomiarowe w systemach, które wymagają przeprowadzenia procesów mikro- i nanostrukturyzacji (wytworzenia układów planarnych wraz z odpowiednim systemem elektrod)

pomagają w pełnym scharakteryzowaniu struktur - metoda rezonansu ferromagnetycznego diody spinowej, pomiary harmonicznego napięcia Halla lub przełączanie magnetyzacji indukowanej spinowo spolaryzowanym prądem. Metody te umożliwiają pełniejszy opis parametrów magnetycznych i elektrycznych układów wielowarstwowych, jak również z ich pomocą można scharakteryzować kluczowe własności z punktu widzenia zastosowań takie jak efektywny kąt Hall-a, który mówi o procentowej konwersji prądu ładunkowego na prąd spinowy, czy też prąd krytyczny przełączania w asyście lub bez zewnętrznego pola magnetycznego. W ostatniej części pracy doktorskiej zawarto między innymi układy o mieszanych anizotropiach magnetycznych, które wykazują zdolność do przełączania swojego namagnesowania bez obecności zewnętrznego pola magnetycznego, co jest niezwykle istotne w przypadku zastosowań podobnych układów do zapisu informacji w postaci namagnesowania w nowoczesnych układach spintronicznych.

Abstract

The discovery of new physical phenomena and further advances in nanotechnology, in particular thin-film systems, enabled the development of a new field of science: spin electronics. In spin electronics (or, for short, spintronics), the electron spin, responsible for the magnetism of thin films, is coupled with a spin-polarized current, which enables, among others, recording, storing, processing and reading information encoded in the form of magnetization.

The presented thesis describes a contribution into the experimental studies of magnetization dynamics in spintronic heterostructures utilizing heavy metals characterized by significant spin-orbit coupling and ferromagnets. Four previously published articles in scientific journals are fully or partially incorporated into this manuscript.

This work introduces to the topic of the dissertation and presents the basic concepts necessary to understand the functioning of spintronic multilayers, such as magnetic tunnel junctions and spin valves, magnetic anisotropy, interlayer exchange coupling, spin torque transfer and spin-orbit torque, magnetoresistance and Hall phenomena. The Kittel formula, indispensable in the measurement of dynamic multilayer systems, as well as the Landau-Lifshitz-Gilbert equation, extended by the transfer of spin torque by Slonczewski, were also described. Then, based on the publications, a series of experiments were discussed that allowed to study the behavior of dynamics in various systems based on magnetic tunnel junctions or their various subparts.

The next part of the work discusses the basics and the results of research on thin-film systems that do not require the use of lithography, these are the ferromagnetic resonance technique using a vector network analyzer, as well as the vibrating magnetometry method, which are used to measure the static and the dynamic properties of multilayer systems. This allows for relatively quick insight into parameters such as the damping constant, anisotropy or interlayer exchange coupling. Subsequent measurement methods in systems that require micro- and nano-structuring processes (fabrication of planar systems with an appropriate electrode system) help to fully characterize the structures - the spin diode ferromagnetic resonance method, Hall voltage harmonics measurements or switching magnetization induced by spin polarized current. These methods enable a more complete description of the magnetic and electrical parameters of multilayer systems. With their help, it is also possible to character-

ize key properties from the point of view of applications, such as the effective Hall angle, which describes the percentage conversion of the charge current into spin current, or the critical switching current with or without application of an external magnetic field. The last part of the dissertation includes systems with mixed magnetic anisotropy, which show the ability to switch their magnetization without the presence of an external magnetic field, which is extremely important in the case of applications of similar systems for recording information in the form of magnetization in modern spintronic systems.

Contents

<i>Introduction</i>	18
<i>Magnetization and magnetic anisotropy</i>	21
<i>Hall effects</i>	27
<i>Magnetoresistance</i>	29
<i>Spin transfer torque and spin orbit torque</i>	34
<i>Magnetization dynamics</i>	39
<i>Results and discussion</i>	41
<i>Summary and Outlook</i>	67
<i>Appendix</i>	68
<i>Bibliography</i>	73

List of Figures

- 1 Ferromagnetic (a) and antiferromagnetic (b) material. 21
- 2 Energy minima in a function of the angle with respect to the system characteristic axis. 22
- 3 Exemplary magnetization curves of easy axis for a FM (a), paramagnet (b), antiferromagnet (c) and the sum with AFM with induced exchange bias (d). 23
- 4 Anomalous Hall voltage as a function of the perpendicular magnetic field of W/Co/NiO structure. 24
- 5 Illustration of the Hall effect (a) and the anomalous Hall effect (b). 27
- 6 Measured ordinary Hall effect along with AHE. Multilayer stack: Ta(1)Pt(4.3)/FeCoB(2)/Ta(2) (thickness in nm). 27
- 7 Illustration of the SHE (a) and the ISHE (b). J_{SP} and J_S are spin-polarized current and spin current, respectively. 28
- 8 Fermi contour of the spin-split (a) dispersion curves of a Rashba system and topological insulator (b). 28
- 9 Orientation of M and j vectors with respect to thin FM. 29
- 10 Angular dependence for $R(\theta)$ for CoFeB strips with size of $20\mu m \times 30\mu m$. 29
- 11 An example of the Hall bar planar device together with Ti/Au gold contact electrodes. 30
- 12 Voltages acquisition for XX and XY configuration for SMR. 30
- 13 Model of electron scattering in a GMR multilayer. 31
- 14 (a) AF-pinned structure and (b) flux-closed AF-pinned structure with corresponding R vs H hysteresis loop. 32
- 15 STT in the trilayer system. The black arrows represent initial magnetization, while the gray arrows represent final magnetization with applied torque. 34
- 16 SOT induced switching of magnetization with applied external magnetic field (a) and without (b). 35
- 17 Exemplary experimental points along with fitted lines for (a) first and (b) second harmonic. Sample structure: Ta(1)/Pt(t_{Pt})/FeCoB(2)/Ta(2) (thickness in nm) with t_{Pt} varying from 4 to 16 nm 36
- 18 Example of standard SD-FMR resonance line of CoFeB measured at different frequency. The red lines are the fit to Eq.37. 37

- 19 Illustration of precession, damping and STT component directions. 40
- 20 Setup schematic of VNA-FMR measurement. 41
- 21 (a) Resonance frequency in perpendicular magnetic field function for type A pMTJs measured using VNA-FMR. (b) Example of $Im(\chi)$ dependencies measured in a sample with $t_{CoFeB} = 1.2$ nm for three different excitation frequencies. 42
- 22 Dispersion relations for FL of type A and type B pMTJs (a) and (b). Symbols denote experimentally obtained resonance frequencies, solid lines represent modelled values, resulting in the K_{eff} presented in (c) and (d). 43
- 23 Illustration of structure from article. FM₁ is coupled via changing IEC to FM₂. 43
- 24 Pole figures of Pt - measured at (a) Pt(111) and (b) Pt(200) - deposited on the Si/SiO₂ substrate measured in the thick position of the Pt wedge. 44
- 25 The x-ray $\theta - 2\theta$ profiles for multilayer (a) and trilayer (b). The red solid line corresponds to the Pt(111), the green corresponds to the Co(111) peak and the red marked with the arrow to the Pt(111) Laue peak 44
- 26 Simulation of the single Pt layer (a), a single Pt layer ($t=3.8$ nm) with decreased interlayer distance at the bottom of the Pt layer ($t=0.8$ nm) (b) and one dimensional Monte-Carlo simulation of polycrystalline columnar structures sample (d). 44
- 27 The FWHM of the Co(111) and Pt(111) in the Co thickness. 45
- 28 The dependence of the sheet conductivity on the thickness of Pt. 45
- 29 The dependence of the sheet conductance on the thickness of Co. 45
- 30 Illustration of standard SD measurement setup. For the best signal, the sample is placed at 45° in azimuth angle. 45
- 31 Designed stripes structure for SOT induced switching. 54
- 32 Sheet conductance dependence on Ta and CoFeB thickness. 54
- 33 The GIXD profiles measured at different positions of Ta wedge. 54
- 34 Structure illustration from article P3. FM₁ coupled to FM₂ via changing IEC. 55
- 35 Illustration of four-point SD measurement setup. For the best signal, the sample is placed in 0° at azimuth angle 55
- 36 Symmetric and asymmetric part comparison of 2-point and 4-point measurement for 2.34nm CoFeB at 5GHz. 56
- 37 (a) Example of the SD-FMR measured for different excitation frequency for the Hall-bar with $t_{Pt} = 4.3$ nm. (b) Dispersion relation for Pt ($t_{Pt} = 4.3$ nm) and Pt-Ti ($m = 7$) underlayers modeled using Kittel formula. (c) FMR linewidth in function of frequency together with a line fit. (d) α reliance on t_{Pt} and number of Pt-Ti interfaces. 64

- 38 (a) First and (b) second harmonic component in function of in plane magnetic field for $t_{Pt} = 4.3$ nm. (c) AHE measurement. (d) Modeled using Eq.28 second harmonic Hall voltage. (e) H_{FL} in function of inversed applied magnetic field. (f) H_{DL} in function of inversed effective magnetic field. 65
- 39 The spin Hall efficiencies for all devices. 65
- 40 Structure of sample with W as HM and CoFeB as FM. 68
- 41 Comparison between two setup measurements. (a) for 1.16nm of HM and (b) for 9.15nm. Both measurement's frequency was set at 5GHz. 2-point setup was measured at 45° and for 4-point at 0° in azimuth angle. 68
- 42 Exemplary angle measurements of 4-point SD-FMR measurement. 69
- 43 For 4-point measurements. Changing resonance field in azimuth angle for thick (a) and thin (b) FM layer in trilayer structure. (c) and (d) are symmetric and asymmetric part for both FM layers, respectively. All measurements was held at 5GHz. 69
- 44 Damping parameter extracted from SD measurements. 69
- 45 eLINE Plus Electron Beam lithography system from Raith. 70
- 46 MicroWriter ML3 from Durham Magneto Optic Ltd. 70
- 47 IonSYS 500 with integrated etching and magnetron sputtering system from Roth & Rau microsystems. 70
- 48 Exemplary mask developed for nanolithography process. Red and blue color correspond to an active area and contact electrodes respectively 71

List of Abbreviation

AF - antiferromagnet
AC - alternating current
AMR - anisotropy magnetoresistance
AHE - anomalous Hall effect
CIP - current in-plane
CIMS - current induced magnetization switching
CPP - current perpendicular to the plane
DC - direct current
FL - free layer
FM - ferromagnetic layer
FMR - ferromagnetic resonance
GMR - giant magnetoresistance
HDD - hard disk drive
HM- heavy metal
IEC - interlayer exchange coupling
LLG - Landau-Lifshitz-Gilbert equation
MRAM - magnetic random access memory
MTJ - magnetic tunnel junction
NM - nonmagnetic metal
PMA - perpendicular magnetic anisotropy
PVD - physical vapor deposition
RA - resistance area product
RAM - random access memory
RE - Rashba-Edelstein
RF - radio frequency
RKKY - Ruderman-Kittel-Kasuya-Yosida interaction
RL - reference layer
PI - pinned layer
SD - spin diode
SyF - synthetic ferromagnet
FMR - ferromagnetic resonance
SOT - spin-orbit torque
STT - spin transfer torque
STO - spin torque oscillator
TMR - tunneling magnetoresistance
UHF - ultra high vacuum
VCMS - voltage controlled magnetization switching
VNA-FMR - vector network analyser ferromagnetic resonance
VSM - vibrating sample magnetometer

List of Publications

List of all publications with the contribution of the author. Thesis is based on the publications marked in bold.

[P1] W. Skowroński, **S. Łazarski**, P. Rzeszut, S. Ziętek, J. Chęciński and J. Wrona, *Influence of a composite free layer structure on thermal stability of perpendicular magnetic tunnel junction*, *Journal of Applied Physics* **124**, 063903 (2018). DOI: doi.org/10.1063/1.5032148

[P2] W. Skowroński, **S. Łazarski**, J. Mojsiejuk, J. Chęciński, M. Frankowski, T. Nozoki, K. Yakushiji and S. Yuasa, *High frequency voltage-induced ferromagnetic resonance in magnetic tunnel junctions*, *Applied Physics Letters* **115**, 072401 (2019). DOI: 10.1063/1.5113681

[P3] W. Skowroński, Ł. Karwacki, S. Ziętek, J. Kanak, **S. Łazarski**, K. Grochot, T. Stobiecki, P. Kuświk, F. Stobiecki and J. Barnaś *Determination of Spin Hall Angle in Heavy-Metal/Co-Fe-B Based Heterostructures with Interfacial Spin-Orbit Fields*, *Physical Review Applied* **11**, 024039 (2019). DOI: 10.1103/PhysRevApplied.11.024039

[P4] **S. Łazarski**, W. Skowroński, J. Kanak, Ł. Karwacki, S. Ziętek, K. Grochot, T. Stobiecki and F. Stobiecki, *Field-Free Spin-Orbit Torque Switching in Co/Pt/Co Multilayer with Mixed Magnetic Anisotropies*, *Physical Review Applied* **12**, 014006 (2019). DOI: 10.1103/PhysRevApplied.12.014006

[P5] Ł. Karwacki, K. Grochot, **S. Łazarski**, W. Skowroński, J. Kanak, W. Powroźnik, J. Barnaś, F. Stobiecki and T. Stobiecki, *Optimization of spin Hall magnetoresistance in heavy-metal/ferromagnetic-metal bilayers*, *Scientific Reports* **10**, 10767 (2020). DOI: 10.1038/s41598-020-67450-3

[P6] K. Grochot, Ł. Karwacki, **S. Łazarski**, W. Skowroński, J. Kanak, W. Powroźnik, P. Kuświk, M. Kowacz, F. Stobiecki and T. Stobiecki, *Current-Induced Magnetization Switching of Exchange-Biased NiO Heterostructures Characterized by Spin-Orbit Torque*, *Physical Review Applied* **15**, 014017 (2021). DOI: 10.1103/PhysRevApplied.15.014017

[P7] **S. Łazarski**, W. Skowroński, K. Grochot, W. Powroźnik, J. Kanak, M. Schmidt and T. Stobiecki, *Spin-orbit torque induced magnetisation dynamics and switching in CoFeB/Ta/CoFeB system with*

mixed magnetic anisotropy, *Physical Review B* **103**, 134421 (2021). DOI: 10.1103/PhysRevB.103.134421

[P8] A. Magni, V. Basso, A. Sola, G. Soares, N. Meggiato, M. Kuepferling, W. Skowroński, **S. Łazarski**, K. Grochot, M.-V. Khanjani, J. Langer and B. Ocker, *Spin Hall magnetoresistance and spin orbit torque efficiency in Pt/FeCoB bilayers*, *IEEE Transactions on Magnetics* **58**, 4400205 (2021). DOI: 10.1109/TMAG.2021.3084866

[P9] W. Skowroński, K. Grochot, P. Rzeszut, **S. Łazarski**, G. Gajoch, C. Worek, J. Kanak, T. Stobiecki, J. Langer, B. Ocker and M. Vafaei *Angular Harmonic Hall Voltage and Magnetoresistance Measurements of Pt/FeCoB and Pt-Ti/FeCoB Bilayers for Spin Hall Conductivity Determination*, *IEEE Transactions on Electron Devices* **68**, no. 12, p. 6379-5385 (2021). DOI: 10.1109/TED.2021.3122999

[P10] S. Ziętek, J. Mojsiejuk, K. Grochot, **S. Łazarski**, W. Skowroński and T. Stobiecki *Numerical model of harmonic Hall voltage detection for spintronic devices*, Accepted on **10 June 2022** for *Physical Review B*.

Introduction

Since ancient times, humankind has sought to store their knowledge for generations in various forms such as verbal descriptions, paintings, carved stones and finally paper. It was not uncommon, and indeed repeatedly happened, that some of this knowledge was lost in various accidents, which also happens - much less often - in the present times. Nowadays we also store, process and transmit that knowledge in the form of information. Due to the technological spur that started in the twentieth century, the amount of information is growing at an exponentially increasing rate. One of the key aims with such immense supply of data is to secure civilization's knowledge and its culture and for that data centers are there, but in order to maintain and conserve such tremendous amount of information, the need of energy use bursts.¹ As today electronics advances into the nano-regime, where the rate of technological progress is being reduced, and overcoming this process through discovering new phenomena and materials is a new task for scientists and engineers.

Currently in electronic devices, electron charges serve as a form of information representation is accompanied by the by Joule heating ². The new prospect of furthering progress in nanotechnology emerged by means of utilizing electron spin. In contrast to classical electronics, spin electronics (spintronics) takes advantage of the binding electron charge and its spin, which can be used to store information, encoded for example in the ferromagnetic element magnetization. Spintronics, still a relatively young science, has found quite a number of uses and applications in the electronic industry.

First, the computer industry used a new technology based on the AMR effect , significantly increasing the areal density by replacing inductive read-write head with read AMR head for HDD. Later, HDD-heads based on the GMR effect^{3,4} were created, which slowly replaced those based on AMR. In 2004 Seagate introduced and demonstrated TMR effect based heads, further improving the signal strength and resolution.

Since then, various spintronic technologies have been successfully applied in the mass storage devices. Apart from the mass-memory, spintronics devices can be used to produce a random access memory type with a nonvolatile operation. The first commercial MRAM devices were produced by Everspin company, with a capacity limited to 4MB, due to magnetic field controlled writing. Later on in 2016 an increase in capacity (256MB) was possible thanks to the STT

¹ N. Jones. *Nat.*, 561(163), 2018

² James Prescott Joule. *The Royal Society Publishing*, 4, 1843

AMR - anisotropic magnetoresistance

HDD - hard disk drive

³ M. N. Baibich. *Phys. Rev. Lett.*, 61 (2472), 1988

⁴ G. Binasch. *Phys. Rev. B*, 39(4828(R)), 1989

GMR - gigantic magnetoresistance

TMR - tunneling magnetoresistance

MRAM - magnetic random access memory

that allowed for very low dimensions, even smaller with PMA. Everspin has now introduced STT-MRAM devices with 1GB of density that have a DDR4-like interface and work like persistent DRAM. Further increase in capacity and durability, as well as operation speed, is possible thanks to SOT. The read and write paths are separated from each other, leading to a significant improvement in reading reliability⁵. Additionally, the writing current is much lower - lower power consumption as well - and the write time should be much faster, since write paths can now be optimized independently. Due to all the benefits of SOT-MRAM, it can be an important memory for future use. However, more research is required on SOT-MRAM to make it available for commercial use.

In use there are two types of memory - mass memory and operational memory (RAM), the former has been using spintronic elements to a large extent for several decades. The latter is mainly based on volatile dynamic RAM and static RAM memories. Utilizing MRAM which combines non-volatility and efficiency with high operation speed could lead to a further reduction in the power consumption of computers and other electronic devices. In general, successful attempts were made to use PMA with the bits perpendicularly magnetized to increase even more the storage density^{6,7} of MRAM. They are generally based on the MTJs, for the read operation TMR effect and for the writing of the information - the STT effect.⁸

An alternative and energy-efficient way to manipulate magnetization in MTJ is via the voltage control of magnetic anisotropy. In this scheme, a voltage is applied to the interface between a magnetic material and an insulator, which generates an electric field and changes the magnetic anisotropy of the material. The reduction of magnetic layer anisotropy enables magnetization switching with lower power. Because of the promising potential of energy efficiency, the electric field-assisted switching of memory based on voltage control of magnetic anisotropy is catching a lot of interest. Recent studies have been reported on voltage-assisted switching in perpendicular MTJ without external magnetic field^{9,10,11} which can be very promising and has the potential to become a prominent memory in the future. Based on the magnetoresistance effects, commercially used magnetic field sensors are the next spintronics application, in automotive as position or angular velocity sensors and TMR-based sensors¹² for medical devices. In the latter case, the possible application is under intensive investigation throughout the world.¹³ The last but not least group is the microwave devices using magnetization dynamics. STO¹⁴ was created by combination of magnetoresistance effects. Due to the STT effect, direct current can flow and generate the RF signal, or RF current can be rectified and detected via SD^{15,16}. The latter is currently under extensive investigation for low-energy power application^{17,18} but also as a form of useful and practical tool in FMR and standing spin-wave resonance investigation, which are fundamental for dynamic-based devices.

In this thesis, the author focuses his research on magnetization dy-

PMA - perpendicular magnetic anisotropy

⁵ K. Jabeur et al. *World Academy of Science, Engineering and Technology*, 7(8), 2013a

⁶ S. N. Piramanayagam. *J. Appl. Phys.*, 102(011301), 2007

⁷ Jeongmin Hong et al. *Appl. Phys. Lett.*, 114(243101), 2019

MTJ - magnetic tunnel junction

STT - spin transfer torque

⁸ J. C. Slonczewski. *JMMM*, 159(1-2):L1-L7, 1996

⁹ P.K. Amiri et al. *J. Appl. Phys.*, 113(013912), 2013b

¹⁰ L. You et al. *Proc. Natl. Acad. Sci. USA*, 112(10310), 2015

¹¹ W.J. Kong et al. *Nat. Commun.*, 10(223), 2019a

¹² V. Nabaei H. Heidari. *Magnetoresistive Sensors*. Wiley Online Library, November 2019. ISBN 9781119552215

¹³ S. Zuo et al. *Adv. Mat. Techno.*, 5(2000189), 2020a

¹⁴ T. Chen et al. *Proceedings of the IEEE*, 104(10):1919-1945, 2016a

STO - spin torque oscillator

RF - radio frequency

¹⁵ M. Harder et al. *Phys. Rep.*, 661(0370-1573):1-59, 2016b

¹⁶ J. Holanda et al. *Phys. Rev Appl.*, 16:014051, 2021a

SD - spin diode

¹⁷ T. Takahashi et al. *AIP Advances*, 10(085218), 2020b

¹⁸ S. Sayed et al. *Appl. Phys. Lett.*, 118(0052408), 2021b

FMR - ferromagnetic resonance

namics in spintronics devices, especially the SD effect. The comprehension and interpretation of the behavior of vector magnetization - its all dynamics - has an important role to play in RF based spintronic devices. In addition to the magnetization dynamics study, the author explores the SOT induced switching in heavy metal/ferromagnetic system for further application of different multilayers systems in SOT-MRAM devices.

The work is divided into eight chapters, starting with this Introduction, the second, third, fourth and fifth chapters incorporate characterization of fundamental magnetoresistance effects and magnetic properties of thin films. The sixth chapter summarizes the basic principles of magnetization dynamics in short. This thesis ends with a chapter on results such as AHE, VNA-FMR, SD and VCMS^{19,20} and summarizes in discussion. The last is Appendix Section where the more detailed comparison between two SD-FMR measurement setups can be found, in addition, the influence of temperature on the anisotropy and at the end the detailed description of nanolithography process is placed.

AHE - anomalous Hall effect

VNA-FMR - vector network analyzer ferromagnetic resonance

¹⁹ K. L. Wang et al. *IEEE Transactions on Nanotechnology*, 14(6):992–997, 2015a

²⁰ K. Munira et al. *J. Appl. Phys.*, 120 (203902), 2016c

VCMS - voltage controlled magnetization switching

Magnetization and magnetic anisotropy

Information in spintronic elements is stored in form of magnetization. Its direction (left/right or up/down) encodes binary data. The memory unit operates properly, when one can efficiently write (change) magnetization state using magnetic-field or spin polarized current and read it for example using magnetoresistance effect. In the meantime, the magnetization should be stable at desired temperature range, which is achieved by designing a system with a sufficiently high magnetic energy. The following section introduce theoretical concept of magnetic anisotropies, energies and coupling mechanisms.

At first, magnetization known also as magnet polarization, is shown as a vector field and it can be explained as density of magnetic dipole moments that are induced in a magnetic material. This effect in material can also be induced when electrical current passes through the material. The origin of magnetization magnetic moments may be microscopic electric currents resulting from electron movement in atoms, or the spin of electrons or nuclei. Magnetization describes material reaction with the applied magnetic field and how, in turn, this material alter this magnetic field, what can be used to estimate forces resulting from this interaction. There are several known magnetic materials such as diamagnetics, paramagnetics, antiferromagnetics, ferromagnetics or ferrimagnetics. In short, paramagnetic materials have weak, induced magnetic field magnetization that disappears with magnetic field removal. In antiferromagnetic materials, magnetic moments of atoms align in a uniform pattern, while adjacent spins points in the opposite direction. This order exists at sufficiently low temperatures, but vanishes at the Néel temperature turning into paramagnetic.

Ferromagnetic materials manifests an atomic-level and long-range order phenomenon which causes unpaired spins of electrons to align parallel to each other in a region called a domain. Within this domains, the magnetic field is strong, nevertheless, bulk material is usually unmagnetized due to the randomly oriented many domain - often mutually extinguishing. In a ferromagnetic material, presence of small external magnetic field can cause these magnetic domains to align with each other initiating magnetization of the material. All ferromagnets have maximum temperatures at which their properties are disappearing as a result of thermal decomposition. This temperature is called the Curie temperature. This manuscript focuses

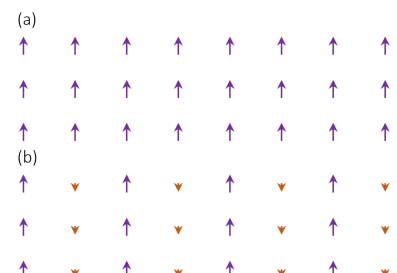


Figure 1: Ferromagnetic (a) and antiferromagnetic (b) material.

primarily on ferromagnetic materials such as Co, CoFe, or CoFeB.

In a low dimensional system, the source of long-range magnetic order is the magnetic anisotropy. It plays an important role in the determination of magnetic properties of magnetic materials and it describes magnetic object behavior, which in turn depends on the magnetic direction. It means that object can be magnetized easier or harder based on how it is placed. Further, magnetic isotropy describes itself as no correlation between any of directions - so with a presence of an external magnetic field, there are no preferable directions (easy or hard).

Most typically, when talking about magnetic materials, which usually consist of thin layers and can be approximated with infinite planes, most have two easy directions where they can be magnetized, typically around 180° apart from each other. These two energetically favorable directions create a parallel line, which is called an easy axis. The remaining of the directions are called the hard axis. Both directions of the easy axes are magnetized just as easily, which means they can be oriented in either direction. It was discovered that in a magnetic object there are several types of magnetic anisotropy. In general, the overall magnetic anisotropy is a combination of these factors. Firstly, magnetocrystalline anisotropy^{21,22} which is basically the atomic structure of crystal, which due to spin orbit interactions and mutual interaction of dipoles induces the preferential direction of magnetization. Compared to other effects, it is a rather weak interaction. Next is the shape anisotropy^{23,24}, which originates from dipole-to-dipole interactions that occur in FM. The demagnetizing field generated by magnetization gives rise to shape anisotropy in FM which has a single magnetic domain, and to those magnetic domains, which in turn make up to larger FM. Another type of magnetic anisotropy is magnetoelastic anisotropy^{25,26} which can be induced by internal stresses and tensions. The lateral lattice in thin films is constrained by the substrate that is not able to expand or condense freely - only out of plane lattice spacing can change candidly. The stress can be induced by magnetoelastic coupling and results in bending of the sample. Finally, the exchange anisotropy^{27,28,29} which describes a magnetic interaction between AFM and FM and also between two FM layers. The origin of this phenomenon is considered to be the coupling between a ferromagnetic spin system and an antiferromagnetic spin system. Antiferromagnets' spin orientation is weakly influenced by the external magnetic field due to the fact that they have no small or any net magnetization.

An interesting phenomenon occurs when AFM and FM are deposited on one another. Ferromagnetic film interfacial spins will be pinned down due to the fact that they are strongly coupled to AFM. It results in different energy reversal costs of the FM's moment corresponding to the energy necessary to create a Néel domain wall within the AFM. The newly added energy shifts the hysteresis loop

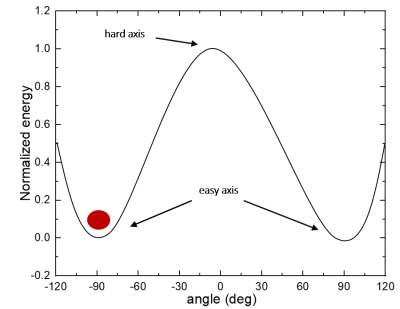


Figure 2: Energy minima in a function of the angle with respect to the system characteristic axis.

²¹ A. E. Clark et al. *Phys. Rev. A*, 42(2), 1972

²² A. Singh et al. *JMMM*, 493(165737), 2020

²³ A. J. Sellmyer et al. *Mat. Sci. and Eng. B*, 6(137-145), 1990

²⁴ A. A. Kusov et al. *Phys. Rev. B*, 46(3123), 1992

²⁵ H. Chiriac et al. *Phys. Rev. B*, 52(10104), 1995

²⁶ A. Zhukov et al. *Nanos. Res. Lett.*, 7(223), 2012

²⁷ AW. H. Meiklejohn and C.P. Bean. *Phys. Rev.*, 102(1413), 1956

²⁸ AW. H. Meiklejohn and C.P. Bean. *Phys. Rev.*, 105(904), 1957

²⁹ AW. H. Meiklejohn. *J. Appl. Phys.*, 33(1328), 2004

of FM also called exchange bias. What is worth noted, annealing process can stabilise and strengthen the exchange bias. But in order to do, the Néel and/or Curie temperature has to be abide or the multilayer stack can be stripped of its desired magnetic properties. Such exchange bias is often used in practical application to created so-called reference layer, which is magnetically harder then the ferromagnet alone.

Magnetostatic energies

The formation of magnetization stems from the arrangement of atomic magnetic moments generated primarily by the electron spin and their interaction with the orbital moment. Moreover, it is ferromagnetic materials' characteristic property. In general, for the FM layer, the E energy consists of several contributions. It is defined as the energy sum of a magnetized sample in the external magnetic field E_Z , the energy of uniaxial anisotropy E_a , the demagnetization energy E_D , the exchange energy E_{ex} , the IEC energy E_{IEC} and the magnetostriction energy E_S :

$$E = E_Z + E_a + E_D + E_{ex} + E_{IEC} + E_S \quad (1)$$

The interaction between H_{ext} and \mathbf{M} is characterized by the Zeeman energy:

$$E_Z = -\mu_0 M_S \int_V (\mathbf{m} \cdot \mathbf{H}) dV \quad (2)$$

where $\mathbf{m} = \mathbf{M}/M_S$ is the magnetization versor. Next, E_a corresponds to:

$$E_a = - \int_V K_1 \sin^2(\alpha) + K_2 \sin^4(\alpha) dV \quad (3)$$

and angle α , which is between the easy axis and \mathbf{m} . E_D - the result of shape anisotropy - is written as:

$$E_D = -\frac{1}{2} \mu_0 M_S \int_V \mathbf{m} \mathbf{H}_D dV \quad (4)$$

where $\mathbf{H}_D = -\hat{\mathbf{N}}\mathbf{M}$ and $\hat{\mathbf{N}}$ is the shape-dependent demagnetization tensor. The following term in Eq.1 is E_{ex} in FM, which is described as follows:

$$E_{ex} = -A \int_V \mathbf{m} \left(\frac{\partial^2 \mathbf{m}}{\partial x^2} + \frac{\partial^2 \mathbf{m}}{\partial y^2} + \frac{\partial^2 \mathbf{m}}{\partial z^2} \right) dV \quad (5)$$

where A is an exchange constant. Next, E_{IEC} , which is given by:

$$E_{IEC} = - \int_S J_1 \mathbf{m}_1 \cdot \mathbf{m}_2 dS - \int_S J_2 (\mathbf{m}_1 \cdot \mathbf{m}_2)^2 dS \quad (6)$$

where \mathbf{m}_1 and \mathbf{m}_2 are normalized magnetization vectors of the two FM. J_1 and J_2 are IEC constants, also called bilinear and biquadratic, respectively. Finally, E_S which can be described as:

$$E_S = - \int_V \left(\frac{3}{2} \lambda \sigma \right) dV \quad (7)$$

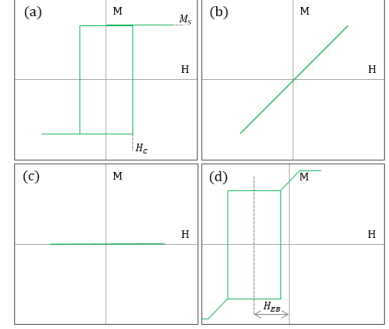


Figure 3: Exemplary magnetization curves of easy axis for a FM (a), paramagnet (b), antiferromagnet (c) and the sum with AFM with induced exchange bias (d).

IEC - interlayer exchange coupling

in which λ is the magnetostriction constant and σ is the strain of the FM material. In general, not all of the energy terms can be present in each system, nevertheless, by taking into account each contribution, the evolution of the magnetization with the magnetic field, as well, as the magnetization dynamics can be simulated and analyzed.

Coupling mechanisms

With two FM layers placed very close to each other, another phenomenon appears, which is called coupling. Apart from the inter-layer exchange coupling, there are a few different coupling mechanisms. For example in MTJ, where two FM are separated by the thin tunnel barrier, a coupling may also occur. In MTJs, the barrier typically is about 0.5 - 3nm, so magnetizations of both layers will be very strongly dependent on each other. The magnetostatic coupling due to stray-field interactions, two dipoles, if placed together, will align themselves antiferromagnetically. Using analytic or numerical micromagnetic simulations, it is possible to estimate the precise evaluation of the coupling energy^{30,31}. Taking into account:

$$J = \mu_0 M_S H_S t_{FM} \quad (8)$$

where M_S is saturation magnetization, H_S is the loop shift, t_{FM} is the FM layer thickness and J is the coupling energy - the hysteresis loop seen in Fig.4 is shifted towards left (negative) fields ($H_S = -31$ Oe), which confirms the present antiferromagnetic coupling.

Lastly, empirically observed by Grünberg³² in 1986, coupling in multilayers caused by interactions between electrons with two FM layers closely together called IEC. Afterwards, the next essential discovery of the oscillating character of ICE was made by Parkin³³ in 1990. He showed that coupling oscillates from antiferromagnetic to ferromagnetic behavior, moreover that it is a function of the spacer thickness. Due to the discovery of ICE's oscillating behavior, the first magnetoresistive read head for HDD was designed using the GMR effect.³⁴

Another coupling mechanism couples nuclear magnetic moments or the localized inner electron spin in a metal through an interaction via the conduction electrons. It is called the RKKY interaction. Firstly, MR Ruderman and C. Kittel proposed a novel interaction to explain unusually wide nuclear spin resonance lines observed in natural metallic silver³⁵. In this article, their approach uses second-order perturbation theory to describe indirect exchange coupling, which involves interfering with one atom's nuclear spin with a conduction electron through hyperfine interaction. Then, this conduction electron interacts with another nuclear spin, causing the energy to be correlated between two nuclear spins. Later, T. Kasuya proposed applying a similar indirect exchange coupling to the localized inner spins of d electrons that interact with conduction electrons³⁶.

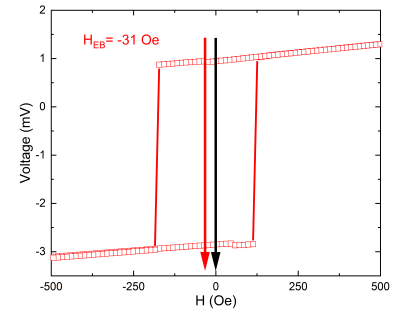


Figure 4: Anomalous Hall voltage as a function of the perpendicular magnetic field of W/Co/NiO structure.

³⁰ R. Engel-Herbert et al. *J. Appl. Phys.*, 97(074504), 2005a

³¹ J. L. O'Connell et al. *IEEE Transactions on Magnetics*, 56(1-8), 2020

³² P. Grünberg et al. *Phys. Rev. Lett.*, 57(2442), 1986

³³ S. S. P. Parkin et al. *Phys. Rev. Lett.*, 64(2304), 1990

³⁴ M. N. Baibich. *Phys. Rev. Lett.*, 61(2472), 1988

RKKY - Ruderman-Kittel-Kasuya-Yosida interaction

³⁵ M.A. Ruderman and C. Kittel. *Phys. Rev.*, 96(99), 1954

³⁶ T. Kasuya. *Prog. of Theor. Phys.*, 16(45), 1956

Then K. Yoshida expanded more entirely to give a Hamiltonian which describes the interactions of d-electron to d-electron spin, nuclear to nuclear spin, and d-electron to nuclear spin³⁷. This mechanism predicts the ferromagnetic/antiferromagnetic oscillation. The RKKY coupling strength between two magnetic planes can be written as³⁸:

$$|J_{12}| = \frac{H_S M t_{FM}}{2n_i} \quad (9)$$

where H_S is the field required to achieve the plateau of the spin engineering structures and complete saturation. As mentioned, the behavior resembles an oscillation around zero. The coupling can take the form of:

$$J_{12} \propto \sin \frac{(\phi + 2\pi t_{HM}/\lambda_F)}{t_{HM}^p} \quad (10)$$

where λ_F is the Fermi wavelength for HM.

Spin polarization

In order to understand the principals of the operation of basically any spintronic device, it is essential to know spin polarization phenomena. Typically, in NM the electrons carry randomly distributed spin and in FM the conducting electrons favor aligning its spins parallel to the magnetization direction, which contributes to positive spin polarization or antiparallel to negative spin polarization. Hence, electrons' injection into thin magnetized layer results in a spin-polarized current at the output. The band structure of the material and density of states at certain energy levels control the spin polarization of a specific FM, which is a sort of inherent property. In order to obtain high spin-polarized currents, spin filtration, the spin Hall effect, Rashba effect or spin-pumping phenomena can be used^{39,40,41}. As the main source of spin polarized current in this manuscript is responsible the spin Hall and Rashba effect (or their inverse equivalents), a separate chapter is devoted to them. Spin filtration and spin pumping effects are briefly explained here. For up and down spin bands, the density of states at the Fermi energy differs by an exchange splitting parameter. From theoretical calculations, the spin polarization can be derived from the density of state according to the equation:

$$\rho = \frac{D_{\uparrow}(E_F) - D_{\downarrow}(E_F)}{D_{\uparrow}(E_F) + D_{\downarrow}(E_F)} \quad (11)$$

Later, the experimental part showed that the spin polarization for specific FM (Fe, Co and Ni) is positive (see Tab.1) and not negative as it should be according to Eq.11 - dominated by electrons with spins down. Also, another detriment of such simple model is impossible influence prediction of tunnel barrier parameters on the spin polarization. Slonczewski⁴² was the first to show a more advanced and complex theoretical model. In his assumptions he stated that

³⁷ K. Yoshida. *Phys. Rev.*, 106(893), 1957

³⁸ S.S.P. Parkin and D. Mauri. *Phys. Rev. B*, 44(7131(R)), 1991

NM - nonmagnetic metal

FM - ferromagnetic layer

³⁹ J. E. Hirsch. *Phys. Rev. Lett.*, 83(1834), 1999

⁴⁰ T.S. Ghiasi et al. *Nano Lett.*, 19(5959), 2019b

⁴¹ Y. Tserkovnyak et al. *Rev. of Mod. Phys.*, 77(1375), 2005b

Material	Spin polarization
Fe	43
Co	45
Ni	37
Co ₂₀ Fe ₆₀ B ₂₀	65
Co ₄₀ Fe ₄₀ B ₂₀	63
Co ₆₀ Fe ₂₀ B ₂₀	57

Table 1: Spin polarization for exemplary FM materials measured by Huang et al.

Adapted from S. X. Huang et al Appl. Phys. Let. 92 (242509) 2008.

⁴² J. C. Slonczewski. *Phys. Rev. B*, 39 (6995), 1989

separated by a thin tunnel barrier FMs are not independent. He calculated the spin polarization of the ferromagnetic-barrier couple by using and solving the Schrödinger equation:

$$p_{fb} = \frac{(k_{\uparrow} - k_{\downarrow})(\kappa^2 - k_{\uparrow}k_{\downarrow})}{(k_{\uparrow} + k_{\downarrow})(\kappa^2 + k_{\uparrow}k_{\downarrow})} \quad (12)$$

where k_{\uparrow} and k_{\downarrow} are the Fermi wave vectors for the up- and down-spin bands, respectively. The first term in Eq.12 correlates with Eq.11 when wave vectors are proportional to the density of states at the Fermi level. The following term relies on the barrier parameters and is able to alter the sign of polarization, which can explain the experimental study.

Spin pumping is another versatile method of creating the spin current and spin accumulation in various conducting materials in nanostructures. In FM/NM bilayers, the magnetization precession in the FM layer yields a DC spin-polarised diffusion current in the NM by an inverse effect of the spin-transfer torque⁴³.

⁴³ Y. Tserkovnyak et al. *Phys. Rev. Lett.*, 88(117601), 2002

Hall effects

Ordinary Hall effect and anomalous Hall effect

Edwin Hall⁴⁴ in 1879 discovered that under the presence of an external magnetic field perpendicular to the current, a conductor shows a transverse voltage due to Lorentz force - it was called the Hall effect (see Fig.5a).

While the ferromagnetic materials are added, the Hall voltage has to include additional contributions which are dependent on the magnetization of the material. Typically, this effect is much larger than the standard or ordinary Hall effect. It is known as the AHE⁴⁵ or the extraordinary Hall effect.

It also depends on both electronic and magnetic properties of the metal. AHE occurs when a charge current going through FM creates a transverse charge current with opposite directions for the different spin polarities. Due to the FM spin orbit coupling, the asymmetric deflection of the charge current - known as side jump⁴⁶ - occurs, and since charge currents of FM typically have a polarization, it results in a net transverse charge current (see Fig.5b).

In Fig.6, one can see that ordinary Hall effect as well as AHE are present. Although measurement in a high perpendicular magnetic field allowed to determine contribution of both effects. Depending on the material system, the magnitudes of AHE and OHE can span over several orders of magnitude⁴⁷.

Spin Hall effect

The next variation is called SHE^{48,49} and appears when a charge current circulates in a material with significant spin-orbit coupling, such as, for example the heavy metal, and a transverse spin imbalance is generated. It is a phenomenon where spins accumulate on the lateral surfaces of the structure which carry electric current. On opposing surface boundaries spins of opposite sign gathers as seen in Fig.7a. In the SHE case, no external magnetic field is needed because of the fact that it is a purely spin-based phenomenon. In short, SHE convert charge currents into spin currents because of spin orbit coupling, which allows SHE to be utilized both for the generation and detection of spin currents and magnetization dynamics. Similar phenomenon but in reverse gives ISHE which simply converts spin current back to charge current⁵⁰.

⁴⁴ E. H. Hall. *American Journal of Mathematics*, 2:287-292, 1879a

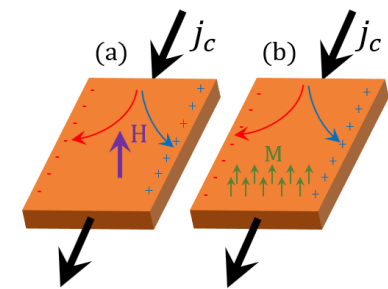


Figure 5: Illustration of the Hall effect (a) and the anomalous Hall effect (b).

⁴⁵ E. H. Hall. *Philosophical Magazine*, 12 (157), 1879b

AHE - anomalous Hall effect

⁴⁶ L. Berger. *Phys. Rev. B*, 2(4559), 1970

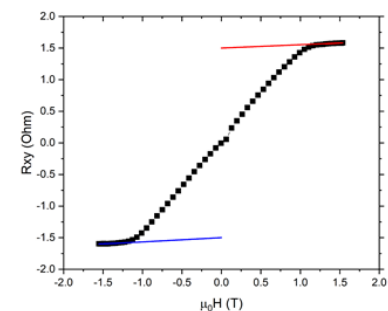


Figure 6: Measured ordinary Hall effect along with AHE. Multilayer stack: Ta(1)Pt(4.3)/FeCoB(2)/Ta(2) (thickness in nm).

⁴⁷ Y. Omori et al. *Phys. Rev. B*, 99 (014403), 2019c

SHE - spin Hall effect

⁴⁸ M. I. Dyakonov and V.I. Perel. *Phys. Lett. A*, 35(6):459-460, 1971

⁴⁹ J. E. Hirsch. *Phys. Rev. Lett.*, 83(1834), 1999

ISHE - inverse spin Hall effect

⁵⁰ M. Ueda E. Saitoh and H. Miyajima. *Appl. Phys. Lett.*, 88(182509), 2006

Rashba–Edelstein effect

The RE, although it does not belong to Hall effects it is one of most important spin-to-charge conversion through an interface-driven effect, which was predicted by V. M. Edelstein⁵¹. The existence of spin-polarized surfaces or interface states can be attributed to its origin. The structural inversion-symmetry breaking induces this effect to occur. This effect breaks the degeneracy of spin in the energy bands, which leads spin polarization to lock momentum in each branch of the dispersion relation. Spin accumulation is generated if, in these spin-polarized surface states, a charge current flows. In the case of topological insulators, there are spin-split surface states as a result of surface topology.

Topological insulators exhibit a spin-split linear dispersion relation on their surface, while exhibiting a narrow band gap on their bulk. Spin and momentum are also locked in this case, and when the charge current flows over these spin polarized surface states, there is spin accumulation. Like with the above effects, the inverse RE effect exists, and it simply converts a spin accumulation into a two-dimensional charge current. The origin of the RE effect is purely intrinsic, whereas the spin Hall effect can be an intrinsic or an extrinsic mechanism. RE effect is typically originating from the interface, whereas, the spin Hall effect originates from the bulk. One can find the field-like torque originates from RE effect and Oersted field while the damping-like consists of both Spin Hall effect and RE effect with addition of thermal effect which was presented very precisely in Du paper⁵². The RE effect has significant role in contribution in current-induced spin orbit torques, especially when the HM layer thickness is becoming thinner than its spin-diffusion length or becomes comparable to RE thickness. As mentioned, these two phenomena often coexist and various experimental techniques and simulation methods need to be utilize in order to separate them.

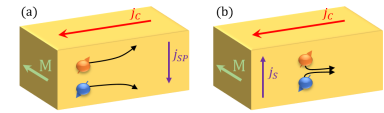


Figure 7: Illustration of the SHE (a) and the ISHE (b). J_{SP} and J_S are spin-polarized current and spin current, respectively.

RE - Rashba-Edelstein effect

⁵¹ V.M. Edelstein. *Solid State Comm.*, 73 (233), 1990

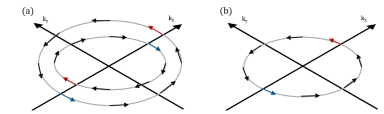


Figure 8: Fermi contour of the spin-split (a) dispersion curves of a Rashba system and topological insulator (b).

⁵² Y. Du et al. *Phys. Rev. Appl.*, 13 (054014), 2020a

Magnetoresistance

The fundamental definitions of different types of magnetoresistance up to the magnetic tunnel junctions where the tunneling mechanism through thin insulating barrier is described. The first one to observe the influence of the magnetic field on resistance in 1857 was William Thomson, also known as Lord Kelvin. He showed that the resistance of Fe and Ni changed with the external magnetic field through the AMR effect⁵³. The discoveries in the late XX century enabled for much stronger magnetoresistance effects such as GMR or TMR (experimentally more than 800% change⁵⁴). The spin polarization, coupling mechanism and STT are also explained.

Anisotropic magnetoresistance

AMR is a special property of material in which electrical resistance is dependent on the angle between the direction of the electric current and the direction of magnetization \mathbf{M} . In general, when an electric field \mathbf{E} is applied to the conductor, a current flows according to the well-known Ohm law:

$$\mathbf{E} = \rho \mathbf{j}, \quad (13)$$

where, ρ is resistivity and \mathbf{j} is current density. If the magnetic field is present and applied to FM with its own \mathbf{M} it causes galvanomagnetic effects. The transportation of electrons depends on the direction of \mathbf{M} and the relation between \mathbf{j} and \mathbf{E} ⁵⁵:

$$\mathbf{E} = \rho_{\perp} \mathbf{j} + \mathbf{m}(\mathbf{j} \cdot \mathbf{m}) \cdot \Delta\rho + \rho_H \mathbf{m} \times \mathbf{j}, \quad (14)$$

where, ρ_{\perp} is resistivity for $\mathbf{m} \perp \mathbf{j}$ and ρ_{\parallel} for $\mathbf{m} \parallel \mathbf{j}$ respectively. $\Delta\rho = \rho_{\parallel} - \rho_{\perp}$, ρ_H is the Hall resistivity and \mathbf{m} is a versor along the magnetization direction. In case of ferromagnets the electric field depends primarily on the magnetization. In case when \mathbf{m} is oriented as the Fig. 9 and $\mathbf{j} = (j, 0, 0)$, \mathbf{E} can be written as:

$$\mathbf{E}(\mathbf{t}) = \begin{pmatrix} E_x \\ E_y \\ E_z \end{pmatrix} = j \begin{pmatrix} \rho_{\perp} + \Delta\rho \sin^2\theta \cos^2\phi \\ \Delta\rho \sin^2\theta \sin\phi + \rho_H \cos\theta \\ \Delta\rho \sin\theta \cos\phi - \rho_H \sin\theta \sin\phi \end{pmatrix} \quad (15)$$

The longitudinal component E_x allows for measurement of the magnetoresistance effect, while the transverse galvanomagnetic is

⁵³ W. Thomson. *Proceedings of the Royal Society of London*, 8(546-550), 1857

⁵⁴ J. Hayakawa. *Appl. Phys. Lett.*, 89 (232510), 2006

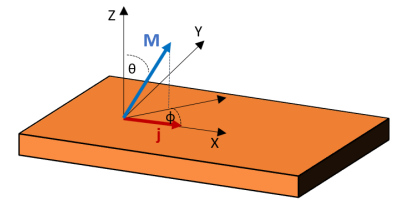


Figure 9: Orientation of \mathbf{M} and \mathbf{j} vectors with respect to thin FM.

⁵⁵ J.-P. Jan. *Solid State Phys.*, 5(1-96), 1957

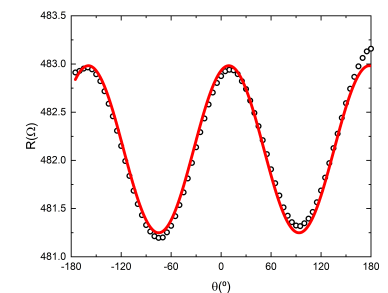


Figure 10: Angular dependence for $R(\theta)$ for CoFeB strips with size of $20\mu\text{m} \times 30\mu\text{m}$.

determined by two remaining component E_y and E_z using Hall-bar configuration (see Fig. 11). Finally, the AMR ratio is defined as follows:

$$AMR = \frac{\rho_{\parallel} - \rho_{\perp}}{\rho_{\perp}} \quad (16)$$

There are many studies on AMR and its dependence on different materials. The McGuire and Potter article sums AMR for Fe, Co, Ni and several more magnetic materials - it is also described how the temperature and thickness of FM affect the AMR.⁵⁶

Spin Hall magnetoresistance

The next transport phenomenon was discovered in a bilayer system where a conductor, typically a metallic layer, is attached to FM and magnetoresistance is influenced due to changes in spin current present in the conductor with a strong spin orbit coupling^{57,58}. This occurrence originates by the simultaneous action of the SHE and ISHE (see Chapter *Hall effects*) thus its name is SMR. Basically, electrons that move through the conductor are being scattered due to SHE in a predetermined direction of its spin orientation. At the edge of the metallic layer, a net accumulation of spins occurs. Through STT (see Chapter *Spin transfer torque and spin orbit torque*), polarized electrons interact with magnetization of FM at the conductor surface⁵⁹. Here are two ways of interaction, where the first is when spins of electrons are aligned parallel to the magnetization direction, in this case, the electrons reflect from the conductors surface and there is no change in its spin. In the second case, if there is any magnetization component that is normal to the electrons' spin orientation, then the spin can flip to the opposite state and in doing so can transfer angular momentum to the FM. As a result, it is observed that spin current which travels at a normal to charge current direction can be modified by changing the magnetization direction. By ISHE, the spin current is deflected and adds or subtracts from the electron momentum depending on the spin Hall angle of the conductor. Through the change in resistivity, the spin current can be estimated⁶⁰:

$$\begin{aligned} R_{XX} &= R_{XX}^0 + \Delta R_{XX}^{AMR} m_x^2 + \Delta R_{XX}^{SMR} m_y^2 \\ &= R_{XX}^0 + \frac{1}{2}(\Delta R_{XX}^{AMR} + \Delta R_{XX}^{SMR}) \sin^2 \theta + \frac{1}{2}((\Delta R_{XX}^{AMR} - \Delta R_{XX}^{SMR}) \sin^2 \theta \cos 2\phi \end{aligned} \quad (17)$$

$$\begin{aligned} R_{XY} &= R_{XY}^0 + \frac{1}{2}\Delta R_{XY}^{AHE} m_z + (\Delta R_{XY}^{AMR} + \Delta R_{XY}^{SMR}) m_x m_y \\ &= R_{XY}^0 + \frac{1}{2}\Delta R_{XY}^{AHE} \cos \theta + \frac{1}{2}(\Delta R_{XY}^{AMR} + \Delta R_{XY}^{SMR}) \sin^2 \theta \sin 2\phi \end{aligned} \quad (18)$$

where θ and ϕ are the magnetization polar and azimuthal angle, respectively. R_{XX}^0 and R_{XY}^0 are the base longitudinal and transverse



Figure 11: An example of the Hall bar planar device together with Ti/Au gold contact electrodes.

Material	°K	AMR ratio (%)
Fe	300	0.2
	77	0.3
Co	300	1.9
	2	0.18
Ni	300	2.02
	77	3.25
Gd	300	0
	77	6.0
Ho	24	22
	4.2	32

Table 2: AMR ratio for different ferromagnetic metals and alloys. *Adapted from D. Ruffer et al APL Mat. 2 (076112) 2014.

⁵⁶ R. Potter T. McGuire. *IEEE Transactions on Magnetics*, 11(4):1018–1038, 1975

⁵⁷ H. Nakayama et al. *Phys. Rev. Lett.*, 110(206601), 2013c

⁵⁸ Y. T. Chen et al. *Phys. Rev. B*, 87 (144411), 2013d

SMR - spin Hall magnetoresistance

⁵⁹ M. Althammer et al. *Phys. Rev. B*, 87 (224401), 2013e

⁶⁰ J. Kim et al. *Phys. Rev. Lett.*, 116 (097201), 2016a

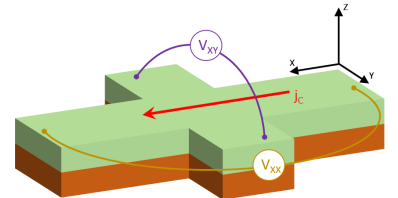


Figure 12: Voltages acquisition for XX and XY configuration for SMR.

resistances. ΔR_{XX}^{AMR} and ΔR_{XY}^{AMR} are the longitudinal and transverse resistance changes due to the anisotropic magnetoresistance - transverse resistance changes are often referred to as planar Hall resistance. ΔR_{XX}^{SMR} and ΔR_{XY}^{SMR} are the longitudinal and transverse resistances arising due to spin Hall magnetoresistance, respectively, and ΔR_{XY}^{AHE} is the transverse resistance change caused by the AHE.

Giant magnetoresistance

Albert Fert⁶¹ and Peter Grunberg⁶² in 1988 discovered simultaneously and independently the GMR effect. Later, due to a significant discovery, they were awarded the Nobel Prize in 2007. The name comes from a much larger change in resistance ratio under the magnetic field than AMR. Basically, the effect occurs when a special combination of multilayers is present: FM/NM/FM where FM can be Fe, Co, CoFe, CoFeB, Ni, NiFe or different alloys highly spin-polarized and NM is typically Co, Cr, Au or Ag.

First, from the FM layer, polarized electrons are injected into the NM layer, where the penetration process goes up to several hundreds of nm, mainly due to the relaxation process^{63,64}.

The penetrated distance is described as the spin diffusion length.⁶⁵ The basis for the GMR phenomenon is the condition that the thickness of the NM layer should be significantly smaller than the spin diffusion length. The resistance of such a multilayer depends on γ between the magnetization vectors of both FM. The Fig.13 represents the Mott two current model, where exactly one can see that the scattering of electrons is much stronger for spins with anti-parallel orientation to the magnetization than for parallel orientation. Typically, there are two basic geometrical configurations in which the GMR effect can be observed - CIP and CPP. As mentioned, resistance depends on the angle between the magnetizations of FL and RL and is expressed by the formula⁶⁶:

$$R(\gamma) = R_P + \frac{R_{AP} - R_P}{2}(1 - \cos\gamma) \quad (19)$$

where R_{AP} is the resistance of the AP state, R_P is the resistance of the P state. The GMR ratio, depending on the type and thickness of the FM and NM layers, can usually be expressed as follows.

$$GMR = \frac{R_{AP} - R_P}{R_P} \quad (20)$$

Magnetic tunnel junction

In 1975, the first to discover the MTJs was Julliere⁶⁷ in Fe/GeO/Co junction at low temperature. Miyazuki⁶⁸ and Moodera⁶⁹ showed that it was possible to use them at room temperature.

At present, MTJs have become a foundation for spintronics devices. The junction construction is similar to that of GMR, but instead of the NM spacer, the nanometer-thick insulating barrier is used. When

⁶¹ M. N. Baibich. *Phys. Rev. Lett.*, 61 (2472), 1988

⁶² G. Binasch. *Phys. Rev. B*, 39(4828(R)), 1989

⁶³ G. Feher and E. A. Gere. *Phys. Rev.*, 114(1245-1256), 1959

⁶⁴ Z. G. Yu. *Phys. Rev. B*, 77(205439), 2008

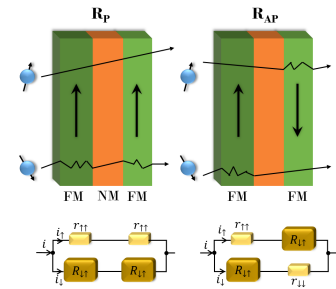


Figure 13: Model of electron scattering in a GMR multilayer.

⁶⁵ M. Isasa et al. *Phys. Rev. B*, 91(024402): 7, 2015b

CIP - current in plane

CPP - current perpendicular to plane

FL - free layer

RL - reference layer

⁶⁶ T. G. S. M. Rijkx et al. *J. Appl. Phys.*, 76(1092), 1994

⁶⁷ M. Julliere et al. *Phys. Lett.*, 51A(225), 1975

⁶⁸ T. Miyazuki and N. Tezuka. *JMMM*, 139(L231-L234), 1995

⁶⁹ J. S. Moodera et al. *Phys. Rev. Lett.*, 74 (3273), 1995

an electric field is applied to the MTJ in order to measure resistance, the voltage potential causes a change of the Fermi levels in the FM, so the electrons start to tunnel through the energy barrier heading to positive voltage potential. With a certain efficiency, called spin polarization, the spin of the electrons should align along with the direction of magnetization for the first FM. Then after the tunneling process, this spin should be kept and enter the second FM layer, where the mechanism depends on the magnetic orientation. With a parallel orientation to the original FM, there should be many unoccupied states in which the electron could tunnel, so the resistance should be smaller. In contrast, when the orientation of the second FM is antiparallel, there are less states available for the electrons to encounter, the probability of reflection is higher - and the resistance increases.

In order for the TMR effect to be experimentally seen, both FM should be characterized by different switching fields for the sake of stable states. Essentially, one of FMs should be magnetically harder, usually called RL, than the other, called FL. This is possible through the use of different materials or thicknesses of FM layers. Generally, in practical applications, it is much easier to do when there is a multilayer structure with an exchange bias⁷⁰ and an AF present. It can be done in two ways (Fig.14), one in which the RL is placed on the additional magnetic layer, which is called PL - and it is separated by a thin spacer layer, typically Ru. This procedure allows the RL and PL layers to be magnetically coupled - called SyF. The second way is where the RL is also the PL without any additional magnetic layer. In both cases, PL is placed directly on AF. To induce exchange bias, the structure is annealed and cooled by Néel temperature of AF.

Tunneling magnetoresistance

Depending on spin polarization of FM material, the TMR ratio compared to GMR is capable of achieving much higher values. Generally, the spins of conducting electrons in FM materials polarize and favor alignment along the magnetization direction. The orientation of both FM layers controls the resistance of MTJ. In the above mentioned Juliere article, the TMR ratio can be calculated as:

$$TMR = \frac{R_{AP} - R_P}{R_P} = \frac{2p_1p_2}{1 - p_1p_2} \quad (21)$$

where R_{AP} and R_P - the resistance in antiparallel and parallel magnetic orientation. p_1 and p_2 are the spin polarization of the FM layers. In case of symmetric electrodes, the spin polarization can be calculated based on the calculated TMR ratio:

$$p = \sqrt{\frac{TMR}{2 + TMR}} \quad (22)$$

Phenomenologically, the resistance of MTJ rely on relative angle between magnetizations of two FM layers, as in the GMR case - it

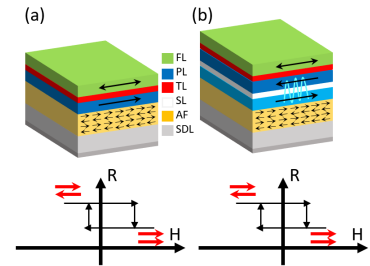


Figure 14: (a) AF-pinned structure and (b) flux-closed AF-pinned structure with corresponding R vs H hysteresis loop.

Addnotation to Fig.14: TB - tunnel barrier, SL - spacer layer, SDL - seed layer

TMR - tunneling magnetoresistance

⁷⁰ J. Nogués and I. K. Schuller. *JMMM*, 192:203-232, 1999

AF - antiferromagnet

PL - pinned layer

SyF - synthetic antiferromagnet

can be described by Eq.19.

Critical switching current

The critical current is the current needed to flip the magnetization from parallel state to antiparallel or in reverse. Generally, the spin-polarized current delivers the energy to the system compared to the energy of FM itself. To estimate that current energy E_I it can be written as:

$$E_I = \eta \frac{\hbar}{2e} I \quad (23)$$

where η is the spin transfer efficiency, \hbar is the reduced Planck constant and e is the electron charge (η originates from STT or SOT what is discussed in the next chapter). The FM's energy can be described as:

$$E_{FM} = \mu M_S H_{eff} A t \quad (24)$$

where A and t are the area and thickness of the FM, respectively, and H_{eff} is the effective magnetic field. If E_{FM} is reduced by an energy loss due to damping α and considered equal to Eq.23, the critical current density - according to Sun⁷¹ - can be estimated as:

$$J_C = \frac{2e\alpha\mu_0 M_S H_{eff} t}{\eta \hbar} = \frac{2e\alpha E_{FM}}{\eta \hbar A} \quad (25)$$

J_C can also serve as a quantitative estimation of the CIMS efficiency. If needed, J_C can be adjusted by changing the energy of FM, α or p . This is a case in single-domain model. In general, the magnetization switching process, even for elements below 100 nm, can be a more complex process, e.g. through nucleation and propagation of the domain wall⁷².

It is also needed to mention different contributions to the magnetic field. The effective field of dated in-plane magnetized FM can be described as the sum of anisotropy field H_{ani} , external magnetic field H_{ext} and demagnetizing field - in-plane magnetized FM - $H_D = \mu M_S/2$ (See chapter *Magnetic anisotropy*):

$$\mathbf{H}_{eff} = H_{ext} \pm H_{ani} \pm \frac{M_S}{2} \quad (26)$$

The H_{eff} can be greatly reduced by using FM with perpendicular magnetic anisotropy⁷³ even though that the anisotropy of such FM is typically higher than for in-plane orientation. In this case, H_{eff} is described as follows:

$$\mathbf{H}_{eff} = H_{ext} \pm (H_{ani} - M_S) \quad (27)$$

All the well-known constants or parameters mentioned in Eqs.25-27 can be measured using static or dynamic magnetometer methods and J_C can be calculated therefrom.

⁷¹ J. Z. Sun. *Phys. Rev. B*, 62(570), 2000

CIMS - current induced magnetization switching

⁷² M. Baumgartner et al. *Nat. Nanotech.*, 12(980), 2017a

⁷³ S. Ikeda et al. *Nat. Mat.*, 9(721-724), 2010

Spin transfer torque and spin orbit torque

Spin transfer torque

The vital matter in designing non-volatile magnetic memories is manipulating the nanoscale elements' magnetization. In general, initial idea of MRAM used Ampere's law, where a high density of current is needed to induce rotation magnetic field to manipulate the magnetic moment of the writing layer. With decreasing dimensions of the storage cell, use of Ampere's law becomes insufficient and as a result it becomes impossible to assess MRAM's high capacities this way. The existence of STT effect was predicted independently by Slonczewski⁷⁴ and Berger⁷⁵ in 1996. The effect describes, in the presence of spin polarized current, the behavior of the magnet. The model also showed that the spin-polarized current flowing through magnet in the nanoscale can affect its own magnetization.

Fig.15 shows a typical structure in MTJ where the STT effect is induced (first experiment with GMR setup⁷⁶). There are two types of alignments: parallel (a) and antiparallel (b). When current is passing from the RL to the FL, parallel magnetization is favored, whereas current passing from the FL to the RL favors antiparallel magnetization.

Generally, RL layer is magnetically hard and separated by a thin tunnel barrier from the magnetically softer FL. Due to the applied voltage, the electrons can tunnel from RL to FL. When polarized electrons pass through RL, magnetization of RL affects them and they become effectively polarized toward it with efficiency depending on the material's polarization. The electron spin is conserved while tunneling through the thin barrier. Then again when penetrating the FL, electrons become polarized along the FL magnetization, but because FL is magnetically soft, FL's magnetization is also affected. This effect is most significant with antiparallel orientation due to different magnetization direction. When the spin of the electrons is transferred to FL, the magnetization's orientation is changed by torque towards parallel to the RL as seen in Fig.15(a).

The case is peculiar when the voltage polarity is applied oppositely. Firstly, electrons pass by FL where they polarize in its direction and then tunnel towards more stable RL. The electrons that have spin in opposite direction to RL's magnetization are reflected, accumulate in FL, and lastly change its magnetization. As mentioned before, this setup favors the antiparallel orientation.

SJT - spin transfer torque

⁷⁴ J. C. Slonczewski. *JMMM*, 159(1-2): L1-L7, 1996

⁷⁵ L. Berger. *Phys. Rev. B*, 54(9353), 1996

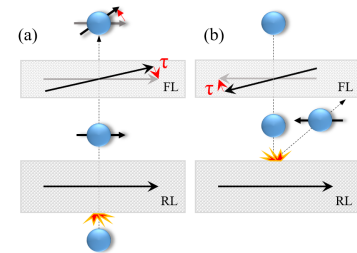


Figure 15: SJT in the trilayer system. The black arrows represent initial magnetization, while the gray arrows represent final magnetization with applied torque.

⁷⁶ E. B. Myers et al. *Sci.*, 285(867), 1999

Spin orbit torque

The new type of current-induced spin torque called SOT was discovered in 2012, which enabled a new type of MRAM, known as SOT-MRAM^{77,78}. Generally, SOT is generated by spin orbit coupling in a single material or material heterostructure, in contrast to STT, where the spin angular momentum is transferred from one FM to another - they also have different geometries, in STT the charge and spin currents are parallel, in SOT they are perpendicular. Typically, with applied voltage, an electric field generates a non-equilibrium orbital occupation that leads to SOT through spin-orbit coupling. There are several types of spin torques studied as SOTs such as the SHE⁷⁹, RE effect⁸⁰, orbital Hall effect⁸¹, thermally generated, phonon driven spin torque⁸² and more. Investigation of SOT allows one to control SOT strength through different external parameters.

In general when speaking of origins of SOTs, these two are well-known models of the SHE and RE effect. The first one assumes that in bi-layer structures, current flows through NM with strong spin-orbit coupling, which generates a spin current perpendicular to the surface. If this spin current impinges on the surface, then a spin transfer torque affects the magnetization of FM. In this case, the bulk spin Hall angle of the material with mixing conductance and strong spin orbit coupling determines the details of the torque. The latter assumes two-dimensional transport, which is described by the Rashba model - similar to SOT in two-dimensional electron gases⁸³. This model gives a direct coupling between the magnetization and the flowing current. Both mentioned models give qualitatively similar results. Such models⁸⁴ that include both the SHE and the interfacial spin-orbit coupling show the existence of two torques: field-like $\mathbf{M} \times (\mathbf{n} \times \mathbf{E})$ and damping-like $\mathbf{M} \times [\mathbf{M} \times (\mathbf{n} \times \mathbf{E})]$, where \mathbf{M} is the magnetization direction, \mathbf{n} is the interface normal direction and \mathbf{E} is the direction of the electric field. The field-like torque has the same form as the precessional torque around an effective field, and the damping-like torque has the same form as the damping torque toward a field in the same direction. Moreover, damping-like torque can also act like an anti-damping torque depending on the details of magnetization and the current direction⁸⁵. The use of SOT driven switching of magnetization with PMA has lately been of much interest because of lower current densities which usually tunnel through thin barrier and in general more application versatility. Generally, using PMA in devices where SOT is used in switching process is challenging task⁸⁶. The parameter which describes the efficiency of the spin to charge current conversion is called the spin Hall angle θ_{SH} and is defined as the ratio of the measured charged current deflected by ISHE in NM and the spin current that is injected into NM. In Fig.16(a), magnetization of FM is not prone to spin current (both vectors are parallel, so torque is zero) - the symmetry breaking mechanism is necessary. In case of (b), the magnetization is tilted similar to article [P4] and can therefore be switched without an applied

SOT - Spin orbit torque

⁷⁷ I. M. Miron et al. *Nat.*, 476(189-193), 2011a

⁷⁸ L. Liu et al. *Sci.*, 336(55), 2012

⁷⁹ M. I. Dyakonov and V.I. Perel. *Phys. Lett. A*, 35(6):459-460, 1971

RE - Rashba-Edelstein

⁸⁰ A. Manchon et al. *Nat. Mat.*, 14(871-882), 2015c

⁸¹ D. Jo et al. *Phys. Rev. B*, 98(214405), 2018

⁸² G. Géranton et al. *Phys. Rev. B*, 91(014417), 2015d

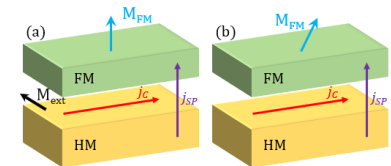


Figure 16: SOT induced switching of magnetization with applied external magnetic field (a) and without (b).

⁸³ Y. A. Bychkov and E.I. Rashba. *JETP. Lett.*, 39(78), 1984

⁸⁴ P. M. Haney et al. *Phys. Rev. B*, 87(174411), 2013

⁸⁵ V. E. Demidov et al. *Phys. Rev. Lett.*, 107(107204), 2011b

⁸⁶ S. Fukami et al. *Nat. Nanotech.*, 11(621), 2016b

external magnetic field.

Torque determination

Phenomenologically, the SOT is divided into two known terms, damping-like and field-like. In the initial studies, it was believed that the damping-like torque originated primarily from SHE in the HM layer⁸⁷, while the RE effect contributed primarily to the field torque⁸⁸. Later, both theoretical and experimental studies indicated mixing of both mechanisms in exertion of damping-like and field-like torques on the FM, which in general convolutes the SOT scenario. In order to extract these torques, one can find several approaches such as SD-FMR line-shape analysis⁸⁹, harmonic Hall voltage analysis^{90,91}, Kerr-effect-based optical determination⁹², SMR⁹³ and threshold current magnetization switching⁹⁴. Here we focus on the first two methods, which are the most known. Harmonic Hall voltage measurements can be divided into field sweeping or angular measurements. In general, harmonic Hall voltage detects the Hall response of harmonic magnetization to a low-frequency AC current, which is commonly used, as this method can simultaneously determine the damping-like and field-like torques. The swinging field at stationary positions is one of the fundamental measurements, but it cannot distinguish the contribution of the Nernst effect from the contribution of the spin. Angular measurements allow one to determine effective torques (See also Chapter *Harmonic Hall voltage measurements in Pt-Ti/CoFeB system*).

However, since this method relies on the AHE and planar Hall effect, materials with a small Hall coefficient will have a meager accuracy due to small Hall voltages. The first (V_{ω}) and second ($V_{2\omega}$) harmonic Hall voltages (see Fig.17) in azimuth angle (ϕ) between the external magnetic field vector and the Hall-bar's long axis are as follows⁹⁵:

$$\begin{aligned} V_{\omega} &= V_P \sin 2\phi \\ V_{2\omega} &= \frac{V_P(H_{FL} + H_{Oe})}{H} \cos \phi \cos 2\phi \\ &+ \left(\frac{V_A H_{DL}}{2H_{eff}} - V_{ANE} \right) \cos \phi \end{aligned} \quad (28)$$

where V_P and V_A are the planar and anomalous Hall voltages, H_{FL} , H_{Oe} and H_{DL} are the field-like, Oersted field and damping-like field components, respectively. $H_{eff} = H + H_k$ is the effective field and is the sum of the external magnetic field and the anisotropy field determined from the AHE measurement in the perpendicular orientation. V_{ANE} describes the additional contribution of the anomalous Nernst effect, which can usually be neglected when bilayers are examined.

SD-FMR is also one of popular methods for measuring the θ_{HM} (See also Chapter *Spin orbit torque induced dynamics and switching in*

HM - heavy metal

⁸⁷ H. Kurebayashi et al. *Nat. Nanotech.*, 9(211), 2014a

⁸⁸ I. M. Miron et al. *Nat. Mater.*, 9(230), 2010a

SD-FMR - spin diode ferromagnetic resonance

⁸⁹ L. Liu et al. *Phys. Rev. Lett.*, 106(036601), 2011c

⁹⁰ J. Kim et al. *Nat. Mater.*, 12(240-245), 2013a

⁹¹ M. Hayashi et al. *Phys. Rev. B*, 89(144425), 2014b

⁹² C. Stamm et al. *Phys. Rev. Lett.*, 119(087203), 2017b

⁹³ H. Nakayama et al. *Phys. Rev. Lett.*, 110(206601), 2013c

⁹⁴ Q. Hao et al. *Phys. Rev. Appl.*, 3(034009), 2015a

AC - alternating current

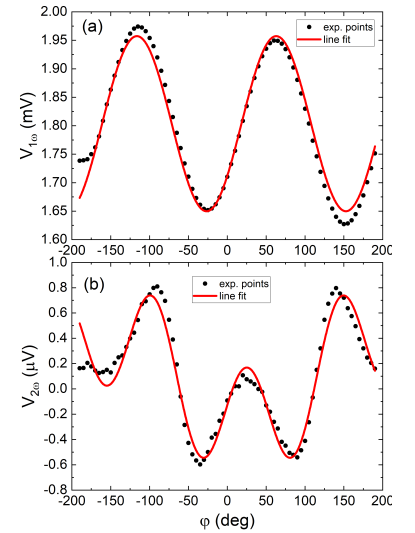


Figure 17: Exemplary experimental points along with fitted lines for (a) first and (b) second harmonic. Sample structure: Ta(1)/Pt(t_{Pt})/FeCoB(2)/Ta(2) (thickness in nm) with t_{Pt} varying from 4 to 16 nm

⁹⁵ K. Fritz et al. *Phys. Rev. B*, 98(094433), 2018a

Pt/Co/Pt), but the acquired data must be carefully analyzed - the resonance linewidth should be determined with an accuracy of an Oe fraction. The mixing signal in response to a combination of in-plane and out-of-plane torques has been calculated in terms of SD-FMR which can be formulated as follows⁹⁶:

$$V_{mix} = -\frac{1}{4} \frac{dR}{d\theta} \frac{\gamma I_{rf} \cos \theta}{\Delta 2\pi (df/dH) |_{H_{ext}=H_0}} [SF_S(H_{ext}) + AF_A(H_{ext})] \quad (29)$$

where $F_S(H_{ext}) = \Delta^2 / [\Delta^2 + (H_{ext} - H_0)^2]$ is denoted as symmetric Lorentzian function centered at the resonant field H_0 with linewidth Δ , $F_A(H_{ext}) = (H_{ext} - H_0) \Delta / [(H_{ext} - H_0)^2 + \Delta^2]$ is an antisymmetric Lorentzian, $S = \hbar J_S / (2e\mu_0 M_S t)$, $A = H_{rf} \left[1 + \left(\frac{4\pi M_{eff}}{H_{ext}} \right) \right]^{1/2}$ and J_S describes the oscillating spin current density. R is the resistance of the strip, f is the resonance frequency and I_{rf} is the rf current through the strip. It is worth noted that this method uses the Oersted field for RF normalization (so I_{rf} is not needed to be known), but neglects the field-like torque which for example in Pt cases is relatively small. A more accurate method, which is based on the analysis of the FMR line shape, requires the measurement of the I_{rf} is described by D. MacNeill⁹⁷

An example SD-FMR resonance measurement can be seen in Fig.18 along with fitted curves - the red lines. In this case, θ_{SH} can be determined according to the following formula⁹⁸:

$$\frac{J_{S,RF}}{J_{C,RF}} = \frac{S}{A} \frac{e\mu_0 M_S t d}{\hbar} \left[1 + \left(\frac{4\pi M_{eff}}{H_{ext}} \right) \right]^{1/2} \quad (30)$$

where $S(A)$ stands for the symmetric (antisymmetric) component part of Lorentzian, μ_0 is the permeability in vacuum, t and d are the thicknesses of the Co and Ir layer, respectively.

For the purposes of this study, a model was developed in cooperation with Ł. Karwacki, which allows the field-like torque and damping-like torque to be analyzed independently, taking into account the evolution of the symmetrical and asymmetric parts as a function of thickness FM⁹⁹.

Magnetization switching

Generally, the key to developing non-volatile memory devices is to control the magnetic state of thin heterostructures with current. STT is used in memories and spin-logic applications to control the state of MTJs. Numerous papers showed that magnetization reversal in spin-valve¹⁰⁰ and MTJ devices¹⁰¹ based on STT allows switching on a timescale of 100 to 1 ns depending on the external field or driving current. STT-based memories are in the process of commercialization and reach a density of 1 GB and a read / write speed of 35ns. Unfortunately, due to non-reproducible dynamic paths and incubation times up to tens of nanoseconds long limits the speed

⁹⁶ L. Liu et al. *Phys. Rev. Lett.*, 106 (036601), 2011c

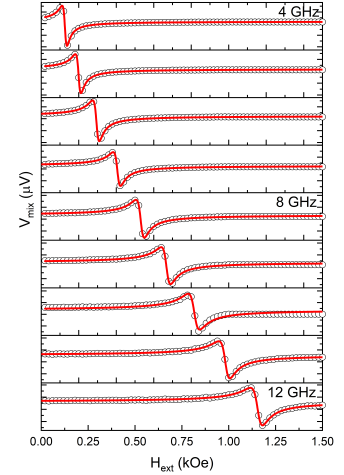


Figure 18: Example of standard SD-FMR resonance line of CoFeB measured at different frequency. The red lines are the fit to Eq.37.

⁹⁷ D. MacNeill et al. *Nat. Phys.*, 13(300-305), 2017c

⁹⁸ L. Liu et al. *Phys. Rev. Lett.*, 106 (036601), 2011c

⁹⁹ W. Skowroński et al. *Phys. Rev. Appl.*, 11(024039), 2019d

¹⁰⁰ H. Liu et al. *J. Magn. Magn. Mater.*, 358-359(233-258), 2014c

¹⁰¹ T. Devolder et al. *Appl. Phys. Lett.*, 108(172409), 2016c

and reliability of the reversal mechanism. SOT may allow to overcome these limitations with in-plane magnetization¹⁰² or perpendicular magnetization¹⁰³. One of its features is due to linking the current injection geometry and conversion of charge to spin mechanism - SOT-switching separates the read and write current paths in the tunnel junction, which minimizes the electrical stress of the tunnel barrier, allowing for independent optimization of the barrier thickness for a high tunnel magnetoresistance. Moreover, the switching speed can be expected to be extremely fast due to the fact that the spin accumulation inducing SOT is orthogonal to the magnetization of FL, thus minimizing the switching incubation time¹⁰⁴. In addition, favoring fast reversal of the magnetization, strong damping in the mono-domain¹⁰⁵ system and fast domain wall motion in multi-domain¹⁰⁶ system control the magnetization dynamic of SOT.

For the purpose of explicating the SOT induced dynamics, several analytical models have been implemented and proposed. The first one based on the macrospin approximation is also the most basic and straightforward¹⁰⁷. In this model, the damping-like torque induces the rotation of the magnetization while the field-like torque facilitates the magnetization's precessional motion around axis orthogonal to the current. It is commonly used to relate the torque amplitude with the critical switching current, even though reversal is still doubtful. The next model based on nucleation at random and magnetic bubble isotropic expansion is induced by domain-wall depinning with help of temperature and the damping-like torque. The most precise micromagnetic model is based on random thermally assisted domain nucleation or simply determined at the sample edge by the competition between an external field and the Dzyaloshinskii-Moriya interaction which is followed by propagation of the domain wall across FM¹⁰⁸. The damping-like torque in this model, which applies to perpendicular magnetization of layers, acts as a z-axis field on the internal domain wall magnetization, which facilitates the expansion of a domain on the side. Although a lot of effort was put in this matter, there are still left a number of unresolved issues such as processes that govern the magnetization dynamics throughout current injection and afterwards, the real timescale, or the initial and intermediate configuration of magnetization preceding switching and lastly the exact role played by both field-like and damping-like torques. The author of this manuscript deals in detail with the switching process through the SOT effect in um-sized structures in Hall strips, focusing mainly on the optimization of the layered structure and magnetic coupling. Further memory development requires miniaturization of elements to sizes of nm order and testing of the three-terminal SOT-MRAM memory¹⁰⁹.

¹⁰² S. Fukami et al. *Nat. Nanotech.*, 11 (621), 2016b

¹⁰³ M. Wang et al. *Nat. Electron.*, 1(582-588), 2018b

¹⁰⁴ K. Garello et al. *Appl. Phys. Lett.*, 105 (212402), 2014d

¹⁰⁵ K. Lee et al. *Appl. Phys. Lett.*, 102 (112410), 2013b

¹⁰⁶ S. Emori et al. *Nat. Mat.*, 12(611-616), 2013

¹⁰⁷ W. Legrand et al. *Appl. Phys. Lett.*, 3 (064012), 2015b

¹⁰⁸ N. Mikuszeit et al. *Phys. Rev. B*, 92 (144424), 2015c

¹⁰⁹ L. Zhu et al. *Adv. Electron. Mater.*, 6 (1901131), 2020b

Magnetization dynamics

Kittel formula

In general, FMR, which is the connection between electromagnetic wave and FM magnetization, is a powerful experimental technique for the characterization of ferromagnetic materials. Such a coupling exhibits power absorption when the frequency of the incident wave is equal to the precession frequency of FM magnetization (called the Larmor frequency^{110,111}). Moreover, the wave polarization and the magnetization orientation must match.

In order to excite precessional motion of the FM magnetization, the ferromagnetic sample is placed under the external magnetic field and the small time-varying RF field. The magnetic field is then swept and, in case this field matches the resonance conditions of the system, the absorption occurs. This specific external magnetic field is called the resonance field H_{res} at a particular microwave frequency. If such measurements are carried out for several frequencies, two important parameters can be obtained - effective magnetization M_{eff} and gyromagnetic ratio γ - from the figure of the frequency vs. resonance field where the formalism described by Charles Kittel¹¹² can be fitted to. This resonance condition formula can be divided for parallel FMR where the external DC field is applied parallel to the thin film and is as follows:

$$\frac{2\pi f}{\gamma} = \sqrt{H_{\parallel}(H_{\parallel} + M_{eff})} \quad (31)$$

where f and H_{\parallel} are the microwave frequency and resonance field, respectively. M_{eff} stands for effective magnetization of the sample. In case where an external field is applied perpendicular to the sample plane - what is called perpendicular FMR - the resonance equation is written as:

$$\frac{2\pi f}{\gamma} = H_{\perp} - M_{eff} \quad (32)$$

Landau Lifshitz Gilbert equation

The LLG formula characterize the dynamical behavior of magnetization in ferromagnetic materials in the presence of an effective magnetic field H_{eff} . The magnetization precession vector appears around the field direction¹¹³ during the application of H_{eff} to the magnet.

¹¹⁰ J. H. E. Griffiths. *Nat.*, 158(670-671), 1946

¹¹¹ E. Zavoisky. *Zhurnal Eksperimental'noi i Teoreticheskoi Fiziki*, 16(7), 1946

¹¹² C. Kittel. *Phys. Rev.*, 73(155), 1948

LLG - Landau Lifshitz Gilbert equation

¹¹³ L. D. Landau and E. Lifshitz. *Physikalische Zeitschrift der Sowjetunion*, 100(1243), 1935

The inherent damping, called the α constant¹¹⁴, causes this precession to fade. In addition, the magnetization damping can be compensated for by the so-called anti-damping term of the STT or SOT. It depends on the polarization of the current. Generally, LLG with an addition of the spin torque components namely anti-damping like and field-like term can be formulated as follows:

$$\frac{dM}{dt} = -\gamma_0 (M \times H_{eff}) + \alpha \left[m \times \frac{dm}{dt} \right] + \frac{\gamma_0}{\mu_0 M_S} \tau \quad (33)$$

where γ_0 is the electron gyromagnetic ratio and α is the Gilbert damping coefficient, $m = M/M_S$ is the normalized vector of the magnetization and τ is components of torque independently anticipated by Slonczewski¹¹⁵ and Berger¹¹⁶. $\tau = a(j)[m \times [m \times p]] + b(j)[m \times p]$ - $a(j)$ and $b(j)$ are the current-dependent functions for the in-plane and the perpendicular torque, respectively, and p is the normalized vector of the fixed layer magnetization. More specialised case for MTJ with two magnetic layers - FL and RL can be shown as:

$$\begin{aligned} \frac{dM_{FL}}{dt} = & -\gamma_0 \times H_{eff} + \alpha M_{FL} \times \frac{dM_{FL}}{dt} \\ & -\gamma_0 \frac{\tau_{\parallel}}{M_S A t} (M_{FL} \times (M_{FL} \times M_{RL})) \\ & -\gamma_0 \frac{\tau_{\perp}}{M_S A t} (M_{FL} \times M_{RL}) \end{aligned} \quad (34)$$

where τ_{\parallel} and τ_{\perp} are Slonczewski components of in-plane and perpendicular torque. M_{RL} and M_{FL} are the magnetization vectors of RL and FL, respectively. In Eq.34, the first term corresponds to Landau-Lifshitz precession motion of M_{FL} around the equilibrium, the second is responsible for energy dissipation called Gilbert damping, the third and the fourth terms describe in-plane torque and perpendicular torque, respectively - see Fig.19. In this case, the STT comes with two components that are perpendicular to each other: τ_{\parallel} and τ_{\perp} . In the event where the material is magnetized in-plane, the component τ_{\parallel} has a direction opposite to the damping torque. Additionally, depending on the bias voltage, different STT component is for the most part responsible for the CIMS. When dealing with low bias voltage, main part is played by τ_{\parallel} in contrast with high bias voltage where τ_{\perp} starts to play an important role in CIMS. In practice, modeling the dispersion relations is complex and numerical models are now used to model experimental curves, as was the case with [P7] *Spin-orbit torque induced magnetisation dynamics and switching in CoFeB/Ta/CoFeB system with mixed magnetic anisotropy* Phys. Rev. B 2021. Model was described in *Numerical model of harmonic Hall voltage detection for spintronic devices*¹¹⁷.

¹¹⁴ T. Gilbert. *Phys. Rev.*, 8(153), 1955

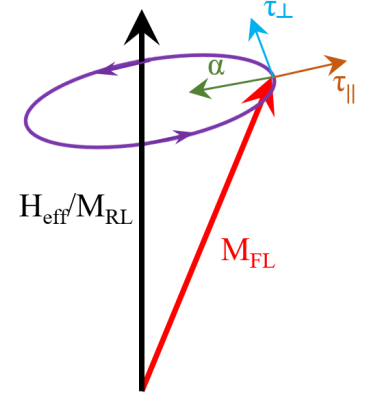


Figure 19: Illustration of precession, damping and STT component directions.

¹¹⁵ J. C. Slonczewski. *JMMM*, 159(1-2): L1-L7, 1996

¹¹⁶ L. Berger. *Phys. Rev. B*, 54(9353), 1996

¹¹⁷ S. Ziętek et al. *accepted for PRB. Arxiv*, 2202.00364, 2022a

Results and discussion

Inductive determination of magnetization dynamics in MTJ structure

One of the simple but powerful tool for understanding the basic dynamics of the multilayer without any need for patterning and lithography is VNA-FMR. The standard setup can be seen in Fig.20. In a standard procedure, the FMR measurement is done by sweeping H_{ext} , while the frequency is kept constant. The sample is placed on a coplanar waveguide. A coplanar waveguide consist of a central stripe line with two ground plane on each side and a ground plane at the bottom of the microware laminate. It is designed to transmit the radio frequency signal up to 20 GHz. The microwave current generated by VNA around the center stripe line which is the signal line induces a microwave magnetic field. Generally, VNA-FMR can give a characterization of a transmitted and reflected signals, which are described by the S-parameters. Depending on the method, one can evaluate the signal data in different ways, but in general use is the S_{21} parameter, which describes a transmission through the coplanar waveguide. There are two modes in which this measurement can be carried out. First, as mentioned, sweeping the field at constant frequency is where the transmission coefficient S_{21} is recorded while varying the field. The second mode is where H_{ext} is set and the frequency of the microwave field is being swept. In this mode signal is obtained from the absolute value of the S_{21} parameter, and in order to subtract the background from the experimental data, two measurements are required, one at low field and the second at maximum field. In both cases, the FMR absorption is of Lorentzian profile.

This section is based on the paper [P1]: *Influence of a composite free layer structure on thermal stability of perpendicular magnetic tunnel junction*. In this article, two types of pMTJ were investigated with varying thicknesses of FM and MgO (capping layer). PMA was achieved for a range of CoFeB and MgO layer. The thermal stability was determined and the field free current induced switching achieved. For the sake of simplicity in listing, the following structure: SyF/W(0.25)/CoFeB(1)/MgO(0.81–0.89)/CoFeB(t_{CoFeB})/W(0.3)/CoFeB(0.5)/MgO(t_{MgO})/ capping layers (thickness in nm) where t_{CoFeB} ranging from 1 to 1.6 nm and t_{MgO} - 0.75 nm is called Type A and second structure with t_{CoFeB} 1.3 nm and t_{MgO} ranging from 0.4 up to 1.4

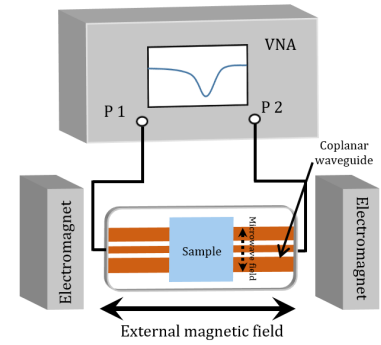


Figure 20: Setup schematic of VNA-FMR measurement.
VNA-FMR - vector network analyzer ferromagnetic resonance

pMTJ - perpendicular magnetic tunnel junction

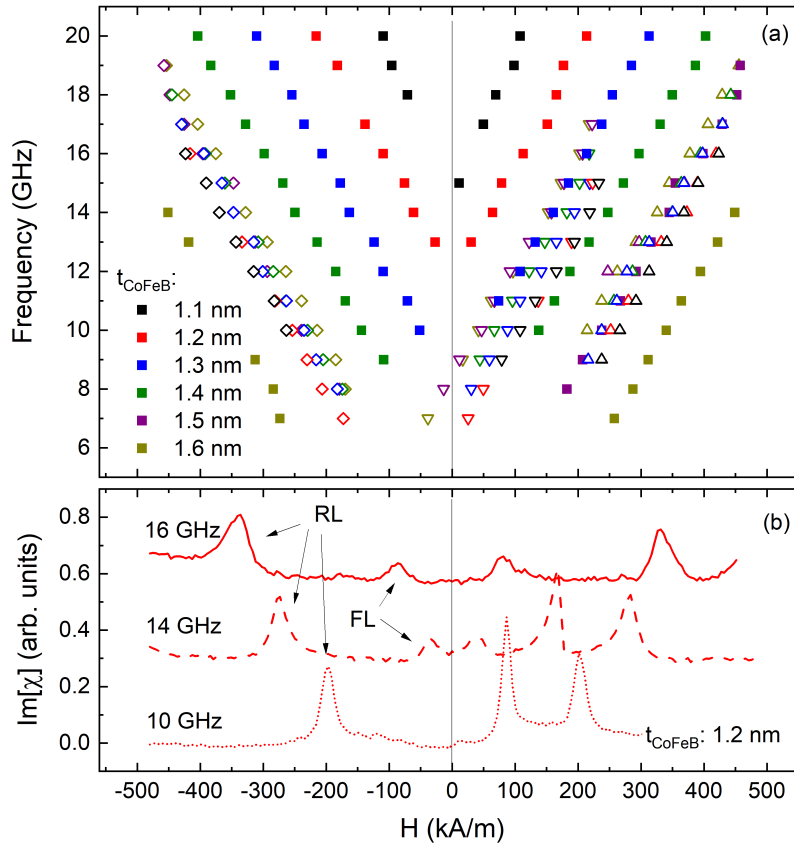


Figure 21: (a) Resonance frequency in perpendicular magnetic field function for type A pMTJs measured using VNA-FMR. (b) Example of $\text{Im}(\chi)$ dependencies measured in a sample with $t_{\text{CoFeB}} = 1.2 \text{ nm}$ for three different excitation frequencies.

nm - Type B. In general, MRAM utilize STT and TMR effects in order to write and read information stored in pMTJ unit cells¹¹⁸. SOT or VCMS are new mechanism incorporated to switch magnetization of FL. One of the critical objectives in data retention is the thermal stability of FL. Typically, the thermal stability factor Δ is the ratio between the FL energy and the thermal energy $k_B T$, where k_B is the Boltzmann constant and T is the temperature. In practical use, it is expected that it should exceed 60 in the case of 10-years data storage¹¹⁹.

Effective PMA was confirmed by VSM measurement in type A pMTJ for $t_{\text{CoFeB}} < 1.6 \text{ nm}$ and in type B pMTJ for $t_{\text{MgO}} > 0.5 \text{ nm}$. The magnetic dead layer along with M_S was extracted and is 0.26 nm and 0.86T up to 1.3T, respectively. In order to quantitatively determine the PMA energy, the VNA-FMR technique was conducted for each t_{CoFeB} and t_{MgO} . An excitation frequency varied between 6 to 20 GHz and a magnetic field was swept from -500 to 500 kA/m at the same time measuring complex magnetic susceptibility (χ) using the VNA. As expected, the resonance peaks for RL and SyF remains constant for different samples, thus significant differences are likely only for the FL. Type A pMTJs all resonance fields for investigated frequencies can be seen in Fig.21. After assigning each branch to an appropriate ferromagnetic layer - open points for RL and full points for FL - the dispersion relation using Kittel's formula¹²⁰ was mod-

¹¹⁸ S. Ikeda et al. *Nat. Mat.*, 9(721-724), 2010

¹¹⁹ D. Apalkov et al. *IEEE Trans. Magn.*, 46(2240-2243), 2010b

¹²⁰ C. Kittel. *Phys. Rev.*, 73(155), 1948

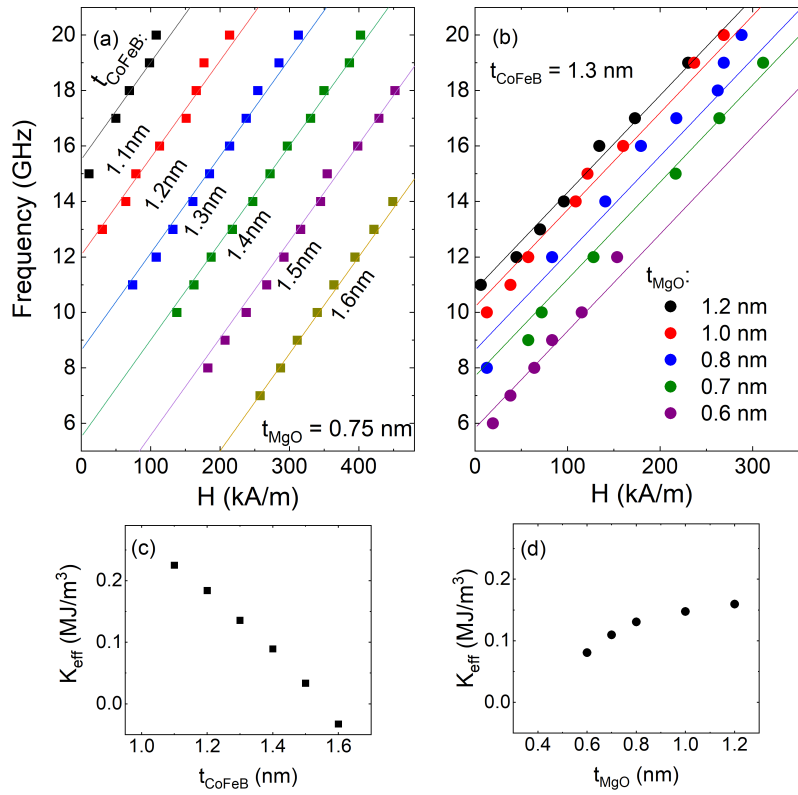


Figure 22: Dispersion relations for FL of type A and type B pMTJs (a) and (b). Symbols denote experimentally obtained resonance frequencies, solid lines represent modelled values, resulting in the K_{eff} presented in (c) and (d).

eled by fixing $\mu_0 M_S$ and fitting energy K_P for each type of pMTJ. It is worth noted that peaks which are observed at higher magnetic fields (up to certain frequency) originate from RL strongly coupled to the top [Co/Pt] superlattice, which forms which compose the purported optical mode¹²¹. Next, for each t_{CoFeB} and t_{MgO} , the effective energy density of PMA was calculated - $K_{eff} = K_P - \mu_0(M_S)^2/2$. The measured dispersion relation (only positive fields) of the FL together with modeled values of type A and type B pMTJs is presented in Fig.22. Undoubtedly, adjusting any of both t_{CoFeB} and t_{MgO} layers allows one to modify the PMA energy, although it has its precise application limitations. While decreasing t_{CoFeB} , the TMR ratio drops due to the fact that the spin polarization of the FL rests on the thickness of the ferromagnetic film¹²². Moreover, when increasing t_{MgO} , the PMA energy can increase, but after reaching the threshold, an additional parasitic serial resistance appears increasing the resistance area product.

Spin orbit torque induced dynamics and switching in Pt/Co/Pt

In the attached article in this chapter [P4]: "Field-Free Spin-Orbit Torque Switching in Co/Pt/Co Multilayer with Mixed Magnetic Anisotropies" the author discuss Anomalous Hall effect loops measurement alongside with structural characterization - X-ray diffraction and X-ray

¹²¹ T. Devolder et al. *Appl. Phys. Lett.*, 108(172409), 2016c

¹²² W. Skowroński et al. *Sci. Rep.*, 7 (10172), 2017d

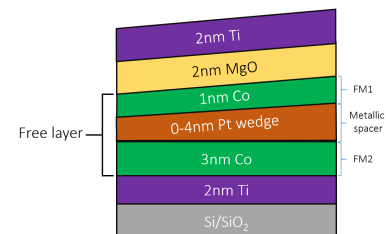


Figure 23: Illustration of structure from article. FM1 is coupled via changing IEC to FM2.

reflectively measurements - SD detection and SOT induced magnetization switching in terms of finding field-free switching of FM. In this manuscript, the author performed micro-fabrications of several samples and performed most measurements, compared and correlated obtained results to sum it up in this manuscript. Typically, AHE loops shows the behaviour of the magnetic layer with perpendicular anisotropy and SD technique is regularly used for local FMR detection in micro- or nano-fabricated devices, while CIMS measurements allow to characterize the type of FM switching. In order to investigate IEC strength and influence on magnetization between two FM layers spaced by Pt layer, the following structure was deposited (See Fig.23) The stripes of size $50 \times 30 \mu\text{m}^2$ were patterned using laser beam lithography. To determine IEC energy in function of Pt spacer, the AHE loops and SD measurements were done. In this work, the field-free switching of FM layer is achieved, furthermore, the neuron-like behaviour of resistance is showed.

To confirm strong texture of Pt, pole figures were measured at the Pt(111) and Pt(200) positions. In former pole figure - See Fig.24 - a spot can be observed in the middle which indicates the growth of the Pt layer towards [111] direction, although the reflections from the (111) planes oriented with respect to each other, form a ring at 70.5° . In the latter pole figure, one's can see ring at 54.7° , - an angle between the (111) and (200) planes - and four strong spots which originate from the single crystal Si(100) substrate. The red circles on Fig.24 (a) and (b) mapped the angles between two (111) planes, and between the (111) and (200) planes as is shown into cubic cell and (c).

SD - spin diode

FMR - ferromagnetic resonance

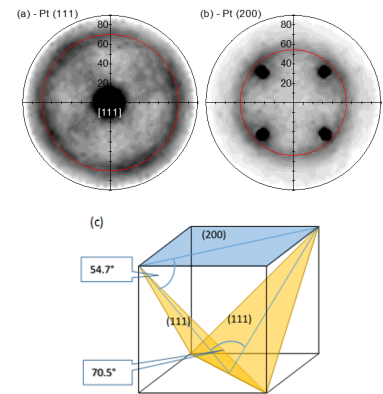


Figure 24: Pole figures of Pt - measured at (a) Pt(111) and (b) Pt(200) - deposited on the Si/SiO₂ substrate measured in the thick position of the Pt wedge.

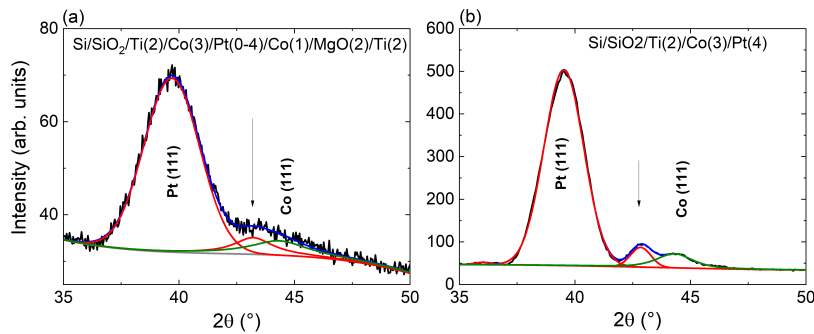


Figure 25: The x-ray $\theta - 2\theta$ profiles for multilayer (a) and trilayer (b). The red solid line corresponds to the Pt(111), the green corresponds to the Co(111) peak and the red marked with the arrow to the Pt(111) Laue peak

The X-ray $\theta - 2\theta$ diffraction profile with theoretical fits of Pt(111) and Co(111) and an unidentified peak superimposed with Co(111) appears (at the position marked with an arrow) and is shown in Fig.25a. To show a more distinct unidentified peak, a simpler trilayer was measured - Fig.25b.

The origin of this unidentified peak is explained by the Monte Carlo simulation described in Ref.¹²³. When the heights of the columnar-shaped Pt grains are comparable with the thickness of the layer, the Laue oscillations appear on both sides of the Pt(111) - Fig.26a. If on the bottom side of the Pt layer the interplanar spacing is lower than

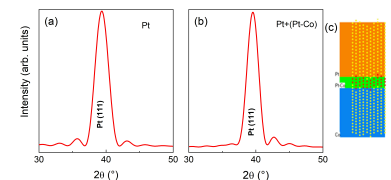


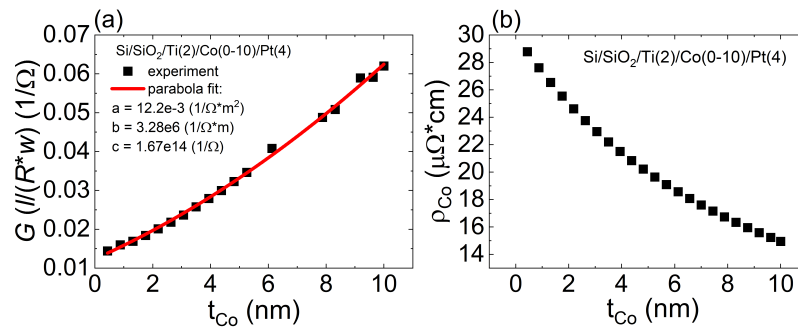
Figure 26: Simulation of the single Pt layer (a), a single Pt layer ($t=3.8$ nm) with decreased interlayer distance at the bottom of the Pt layer ($t=0.8$ nm) (b) and one dimensional Monte-Carlo simulation of polycrystalline columnar structures sample (d).

¹²³ J. Kanak et al. *J. Appl. Phys.*, 113 (023915), 2013

in the middle part of the Pt layer, the oscillations on the left side of the Pt (111) are declined, whereas the oscillations on the right are enhanced - Fig.26b. The simulations represent the grains in the Pt and Co layers and a transition area with the Pt-Co mixed interface. A very good agreement is achieved between the experimental and theoretical values.

The resistivity changes of the Co sublayer as a function of thickness were analyzed by the full width at half maximum (FWHM) rocking curves of the Co(111) texture. As can be seen in Fig.27, the FWHM parameter of the (111) texture of the top Pt with a fixed thickness, remains approximately constant, whereas the FWHM of the Co(111) strongly increasing with decreasing the thickness of the Co layer. The weakening of the Co(111) texture with decreasing Co layer thickness can be the reason for the increase in Co layer resistivity.

Resistances of the stripes were measured using the four-probe method. The sheet resistance, sheet conductance and the resistivity are calculated based on the procedure described in Ref.¹²⁴. In Fig.28, the sheet conductance of the Co (5) / Pt (0-10) bilayer is presented. Using the model and fitting the experimental results the constant value of $\rho_{Pt} = 23\mu\Omega cm$ for Pt greater than 2 nm. For thinner Pt the HM discontinues and the sheet conductance decreases. In contrast to the case of the Pt wedge, the resistivity of the Co layer depends on its thickness. Based on the adapted model, ρ_{Co} decreases from around 29 down to $15\mu\Omega cm$ with increasing Co thickness seen in Fig.29.



In this particular case, the sample was deposited in a wedge form, so wafer-level VNA-FMR measurements were not suitable. Instead, the microstripes were measured using the so-called SD effect, described below. It is one of the really powerful tools for investigating magnetization dynamics in nanofabricated devices. Recently, this technique has attracted many scientists. An illustration with an assembly scheme for such a measurement is in Fig.30 and includes: RF generator, T bias, two electromagnets, power supply and microwave probe. The sample itself was placed on a device that allows you to control the azimuth ($-180 - 180^\circ$) and polar ($-80 - 200^\circ$) angles.

In general, SD detection is based on the RF current rectification effect, where when the RF current and oscillating magnetization are

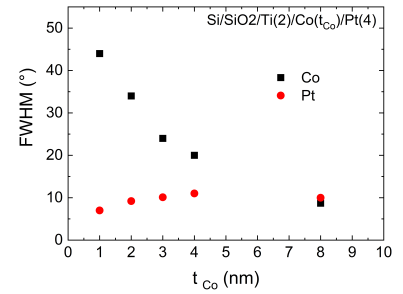


Figure 27: The FWHM of the Co(111) and Pt(111) in the Co thickness.

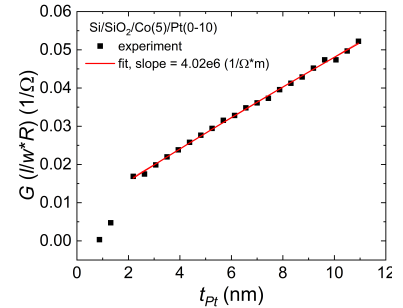


Figure 28: The dependence of the sheet conductivity on the thickness of Pt.

¹²⁴ M. Kawaguchi et al. *Appl. Phys. Lett.*, 112(202405), 2018

Figure 29: The dependence of the sheet conductance on the thickness of Co.

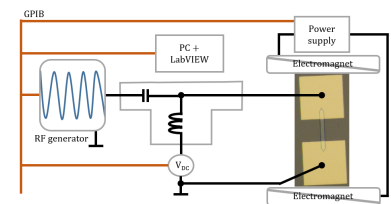


Figure 30: Illustration of standard SD measurement setup. For the best signal, the sample is placed at 45° in azimuth angle.

mixed, a DC voltage is generated. In order to observe this effect, there is required condition - a coupling between the RF current and a magnetization precession. When the requirement is met, the magnetoresistance effect induces resistance oscillations^{125,126}. There are two possible cases where this coupling can be realized - a magnetic field torque or STT/STO. The former is the case where the generated RF magnetic field contributes to the field torque, which in turn drives the magnetization. While in the latter, the spin-polarized current induced by STT/STO via SHE¹²⁷ drives the magnetization precession. The mixing of RF current with oscillation resistance consists of DC and AC voltages, where the first is SD voltage and the second is an excitation signal of the second harmonic. It can be written as follows.

$$V_{out} = V_{DC} + V_{AC} = \delta R \cos(\omega t + \psi) \times I_0 \cos(\omega t) = \frac{\delta R I_0}{2} (\cos \psi + \cos(2\omega t + \psi)) \quad (35)$$

where I_0 and ω are the amplitude and angular frequency of the RF current, respectively. δR expresses the oscillation amplitude of the resistance and ψ represents the phase difference between the current and the dynamic resistance.

A simplified equation can be expressed by Eq36 due to the fact that bias-T filters the signal by separating the AC and DC parts, leaving the latter for measurement purpose:

$$V_{DC} = \frac{\delta R I_0}{2} \cos \psi \quad (36)$$

The symmetric and antisymmetric parts can be described using Lorentz curves as:

$$V_{mix} = V_S \frac{\Delta H^2}{(\Delta H^2 + (H - H_0)^2)} + V_A \frac{\Delta H(H - H_0)}{\Delta H^2 + (H - H_0)^2} \quad (37)$$

where V_S and V_A are the magnitudes of the symmetric and antisymmetric Lorentz curve, respectively. ΔH is the linewidth and H_0 is the resonance field.

DC - direct current

¹²⁵ A. Yamaguchi et al. *Phys. Rev. B*, 78 (104401), 2008

¹²⁶ M. Harder et al. *Phys. Rep.*, 661(0370-1573):1-59, 2016b

¹²⁷ L. Liu et al. *Phys. Rev. Lett.*, 106 (036601), 2011c


Field-Free Spin-Orbit-Torque Switching in Co/Pt/Co Multilayer with Mixed Magnetic Anisotropies

Stanisław Łazarski,^{1,*} Witold Skowroński,¹ Jarosław Kanak,¹ Łukasz Karwacki,^{1,2} Sławomir Ziętek,¹ Krzysztof Grochot,^{1,3} Tomasz Stobiecki,^{1,3} and Feliks Stobiecki²

¹*Department of Electronics, AGH University of Science and Technology, Al. Mickiewicza 30, 30-059 Kraków, Poland*

²*Institute of Molecular Physics, Polish Academy of Sciences, ul. Smoluchowskiego 17, 60-179 Poznań, Poland*

³*Faculty of Physics and Applied Computer Science, AGH University of Science and Technology, Al. Mickiewicza 30, 30-059 Kraków, Poland*

 (Received 13 March 2019; revised manuscript received 9 May 2019; published 2 July 2019)

Spin-orbit-torque- (SOT) induced magnetization switching in a Co/Pt/Co trilayer, with two Co layers exhibiting magnetization easy axes orthogonal to each other is investigated. A Pt layer is used as a source of spin-polarized current as it is characterized by relatively high spin-orbit coupling. The spin Hall angle of Pt, $\theta = 0.08$, is quantitatively determined using the spin-orbit-torque ferromagnetic resonance technique. In addition, Pt serves as a spacer between two Co layers and depending on its thickness, different interlayer-exchange-coupling (IEC) energy between ferromagnets is induced. Intermediate IEC energies, resulting in a top Co magnetization tilted from the perpendicular direction, allows for SOT-induced field-free switching of the top Co layer. The switching process is discussed in more detail, showing the potential of the system for neuromorphic applications.

DOI: [10.1103/PhysRevApplied.12.014006](https://doi.org/10.1103/PhysRevApplied.12.014006)

I. INTRODUCTION

Manipulation of the magnetization of micro and nanostructures by electrical means allows for the design of low-energy and scalable spintronic devices [1]. A number of applications taking advantage of magnetic tunnel junctions (MTJs) and spin-valve structures, which utilize magnetoresistance and spin-transfer-torque (STT) [2,3] effects for operation, have been proposed. Magnetic tunnel junctions with an in-plane magnetic easy axis based on MgO have been among the most studied devices due to a high tunneling magnetoresistance (TMR) ratio [4], and current-induced magnetization switching [5] observed in the absence of an external magnetic field. Unfortunately, in general, they require high critical-current densities for the magnetization switching. Recently, MTJs with a perpendicular easy axis have been proposed to reduce this switching current and to enhance thermal stability of the free layer [6–8]. Nonetheless, the current densities used for switching may degrade MgO tunnel barrier properties with time, which hampers potential endurance of the device. On the other hand, spin-orbit-torque- (SOT) driven switching of magnetization with perpendicular magnetic anisotropy (PMA) has emerged and gained a lot of attention as it does not require high-density current flow via a thin MgO tunnel

barrier. Initially, SOT switching of perpendicularly magnetized ferromagnets has relied on an external magnetic field to break the time-reversal symmetry [9–11]. However, it would be impractical to use the external field for device application. By using antiferromagnets, the symmetry can be broken and magnetization switching in the absence of the external magnetic field can be achieved [12–17].

In this work, we present another concept utilizing two Co layers with orthogonal easy axes [18,19] that are coupled via interlayer exchange coupling (IEC) across a Pt spacer as for example in Ref. [20] to achieve SOT switching without the external magnetic field [21,22]. The magnetization of the top Co layer is tilted from the perpendicular direction due to ferromagnetic coupling with an in-plane magnetized bottom Co layer. In addition, the Pt spacer serves as a source of the spin current due to spin-orbit coupling characterized by the moderate spin Hall angle (θ_{SHE}) [10,23,24]. Moreover, the nonorthogonal direction of Co-layer magnetizations results in analogue-like switching behavior. This property of the device is potentially useful as a building block of a neuromorphic network utilizing spintronic elements [15].

II. EXPERIMENT

The following multilayer structure is investigated: Si/SiO₂/Ti(2)/Co(3)/Pt(t_{Pt})/Co(1)/MgO(2)/Ti(2) (thickness in nm) with t_{Pt} varying from 0 to 4 nm. The

*lazarski@agh.edu.pl

thicker Co layer exhibits in-plane anisotropy, whereas the thinner one is characterized by effective perpendicular anisotropy. In order to determine the resistivity and SOT dynamics of Pt and Co, additional multilayer structures of Si/SiO₂/Co(5)/Pt(0-10) and Si/SiO₂/Ti(2)/Co(0-10)/Pt(4) are prepared. All samples are deposited using a magnetron sputtering system in an Ar atmosphere. After the deposition process, all samples are characterized by x-ray diffraction (XRD). X-ray reflectivity (XRR) measurements are made in order to control the thickness of particular layers in the system [25]. The texture is inspected using rocking-curve and polar-figure methods (see the Supplemental Material [26]). The Hall bars and stripes dedicated for spin-orbit-torque ferromagnetic resonance (SOT FMR) measurements are fabricated using electron-beam lithography, ion-beam etching, and a lift-off process. The nominal dimensions of samples are $w \times l$, where $w = 10, 20, 30 \mu\text{m}$ and $l = 100 \mu\text{m}$ for SOT-induced dynamics measurements and Hall bars of $w = 10, 20, 30 \mu\text{m}$ and $l = 24 \mu\text{m}$ for current-induced magnetization-switching experiments, Fig. 1. Electrical connections are fabricated using Al(20)/Au(30) contact pads of $100 \times 100 \mu\text{m}$. A dedicated multiprobe system, which enables sample rotation in a given plane under the external magnetic field, is used.

The resistivities of Co and Pt layers are determined in a Pt and Co wedge sample, as described in Ref. [27]. The Pt resistivity is almost constant $\rho_{\text{Pt}} \approx 23 \mu\Omega\text{cm}$, whereas the Co resistivity, ρ_{Co} , varied from 15 to 29 $\mu\Omega\text{cm}$ with decreasing thickness. Detailed information is presented within the Supplemental Material [26]. We note that ρ_{Pt} is smaller than in our previous work [28] because in this case Pt is deposited on high-textured Co, in contrast to Pt deposited on amorphous Co-Fe-B. The SOT FMR measurements are conducted in an in-plane magnetic field applied at an 45° angle with respect to the long stripe axis and rf-signal power of 16 dBm. The dc voltage

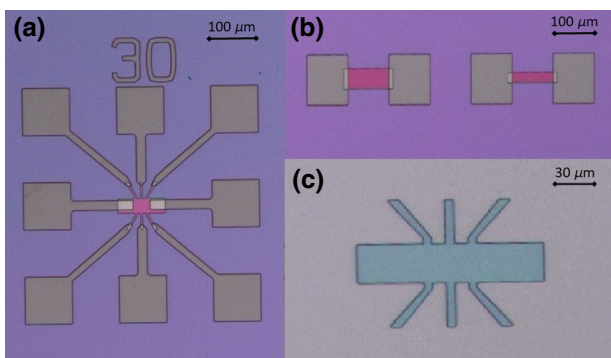


FIG. 1. Layout of the fabricated devices used for different measurements: (a) Hall bar for SOT-induced switching, (b) stripes of different width for SOT dynamics. Detailed dimensions of the Hall bar are given in (c).

originating from the mixing between oscillating resistance (due to SOT and magnetoresistance) and in-phase charge current are measured using a lock-in amplifier, which is synchronized with an amplitude modulated rf source. The SOT-induced switching experiment is performed in both in-plane and perpendicular magnetic fields. In order to show the analoguelike behavior, the experiment with varying time of the switching pulses between 500 μs and 500 ms is performed.

III. RESULTS AND DISCUSSION

Spin-transport properties of Pt, such as the spin Hall angle and spin-diffusion length, are determined using a dedicated model based on Ref. [28]. Mixing voltage, V_{mix} , is obtained from the SOT FMR measurement as a function of magnetic field, H , and the results are presented in Fig. 2. The signal consists of two parts (symmetric and antisymmetric), which are modeled using Lorentz curves,

$$V_{\text{mix}} = V_S \frac{\Delta H^2}{\Delta H^2 + (H - H_0)^2} + V_A \frac{\Delta H(H - H_0)}{\Delta H^2 + (H - H_0)^2}, \quad (1)$$

where V_S (V_A) is the magnitude of symmetrical (antisymmetrical) Lorentz curve, ΔH is the linewidth, and H_0 is the resonance field.

We assume that the greatest contribution to magnetoresistance comes from the spin Hall magnetoresistance (SMR) effect, which can be described in this case via the model developed in Ref. [29],

$$\frac{\Delta R}{R_{\text{Pt}}} \approx \frac{\theta^2 \lambda}{t_{\text{Pt}}} \left[\frac{g_{\text{Pt}}^R}{1 + g_{\text{Pt}}^R} - \frac{g_{\text{Pt}}^{\text{Co}}}{1 + g_{\text{Pt}}^{\text{Co}} \coth(t_{\text{Pt}}/\lambda)} \right] \times \tanh \frac{t_{\text{Pt}}}{\lambda} \tanh^2 \frac{t_{\text{Pt}}}{2\lambda}, \quad (2)$$

where $R_{\text{Pt}} = l\rho_{\text{Pt}}/(t_{\text{Pt}}w)$, and λ is the resistance, the spin Hall angle, and the spin-diffusion length of Pt. Respectively, $g_{\text{Pt}}^R = 2e^2/\hbar\lambda\rho_{\text{Pt}}G^R \coth(t_{\text{Pt}}/\lambda)$ is the real part of

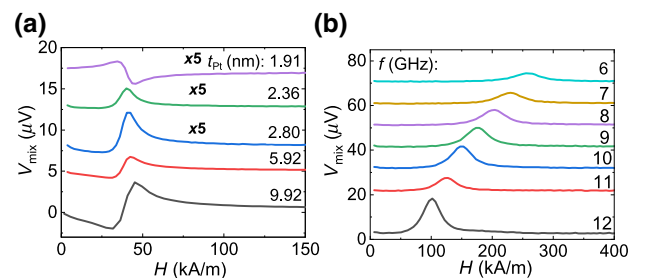


FIG. 2. V_{mix} as a function of magnetic field measured in bilayers for different Pt thicknesses with excitation frequency $f = 4 \text{ GHz}$ (a) and fixed $t_{\text{Pt}} = 2.36 \text{ nm}$ with different f (b). Curves are artificially offset for clarity.

dimensionless spin-mixing conductance with G^R being the real part of spin-mixing conductance, and

$$g_{\text{Pt}}^{\text{Co}} = \frac{(1 - p^2)\rho_{\text{Pt}}\lambda}{\rho_{\text{Co}}\lambda_{\text{Co}}\coth(t_{\text{Co}}/\lambda_{\text{Co}})} \quad (3)$$

is the dimensionless spin conductivity of the Pt/Co interface, where p is the spin polarization of Co at the Fermi level, and λ_{Co} is the spin-diffusion length in the Co layer [29].

The symmetric component to the signal is known to originate from the spin Hall effect induced antidampinglike field [28],

$$H_{\text{DL}} \approx -\frac{\hbar j_c^{\text{Pt}}}{2eM_s t_{\text{Co}}} \theta \left[1 - \text{sech} \frac{t_{\text{Pt}}}{\lambda} \right] \frac{g_{\text{Pt}}^R}{1 + g_{\text{Pt}}^R}, \quad (4)$$

where M_s is the saturation magnetization of Co, and j_c^{Pt} is the current density in the Pt layer. Moreover, in the derivation of formula (3) we assume a negligible imaginary part of spin-mixing conductance. The antisymmetric component, on the other hand, is dominated by contributions from the Oersted field,

$$H_{\text{Oe}} = -\frac{j_c^{\text{Pt}} t_{\text{Pt}}}{2}, \quad (5)$$

and interfacial Rashba-Edelstein contribution,

$$H_{\text{SO}} = \Gamma_{\text{SO}}, \quad (6)$$

which is determined by thickness-independent spin-orbit coupling strength Γ_{SO} [28]. We consider here this contribution as originating from interfacial spin-orbit coupling, and distinct from spin Hall contribution, as predicted theoretically [30], although it is still the subject of an ongoing debate. Experimental works, however, seem to confirm the possible Rashba-Edelstein origin of the field [31,32]. Note that an interfacial contribution might be also attributed to the magnetic proximity effect from a ferromagnet [33,34], which was recently discussed by Zhu *et al.* [35]. The authors showed that the proximity effect in Co/Pt and $\text{Au}_{25}\text{Pt}_{75}/\text{Co}$ interfaces has minimal correlation on either dampinglike or fieldlike spin-orbit torques compared to other interfacial effects like interfacial spin-orbit scattering. The relevant parameters used to model the effective fields are summarized in Table I.

The components V_S and V_A , obtained from Lorentz curve modeling for Co/Pt bilayers, are presented in Figs. 3(a) and 3(c) as functions of t_{Pt} . These dependencies are further fitted with Eqs. (4)–(6). As a result, the spin Hall angle of $\theta = 0.08$ is obtained, which agrees with literature values for this material [28,36]. Note, that in Fig. 3(d) the effective spin Hall angle, $\theta^{\text{eff}} \approx 0.1$, obtained roughly from ratio V_S/V_A is slightly larger than the spin Hall angle

TABLE I. Magnetotransport parameters of the modeled Co/Pt bilayer system.

Model	Value	Fitted	Value
λ_{Co}	1 nm ^a	θ	0.08
p	0.75 ^a	λ	2.17 nm
$G^R/(e^2/\hbar)$	$3.9 \times 10^{19} \Omega^{-1} \text{cm}^{-2}$	Γ_{SO}	119 A/m

^aRef. [29].

of Pt, $\theta = 0.08$, obtained from fitting the model derived in Ref. [28] to the data. As shown there, the spin Hall angle is treated as a bulk property of heavy metal layer and agrees with the effective spin Hall angle for thick Pt.

Next, we focus on multilayer structures with two Co layers (3 and 1 nm) separated by a Pt spacer of different thickness. Thicker (thinner) Co is characterized by in-plane (perpendicular) magnetic anisotropy, which is manifested by the shape of the anomalous Hall effect (AHE) hysteresis loop [Fig. 4(a)]. In addition, these two layers are ferromagnetically coupled, and the energy of this coupling varies with t_{Pt} [20]. To quantitatively determine the coupling energy, AHE curves for different Pt spacers are modeled using a macrospin approach [37], and the energy values are depicted in Fig. 4(c). For high coupling energies (corresponding to $t_{\text{Pt}} < 3$ nm) the AHE loop is hysteresis-free. For the spacer thickness of $t_{\text{Pt}} > 3$ nm, hysteresis in AHE is observed, which enables the SOT-induced switching presented below.

As shown above, the top Co layer is tilted from the perpendicular direction due to ferromagnetic coupling with

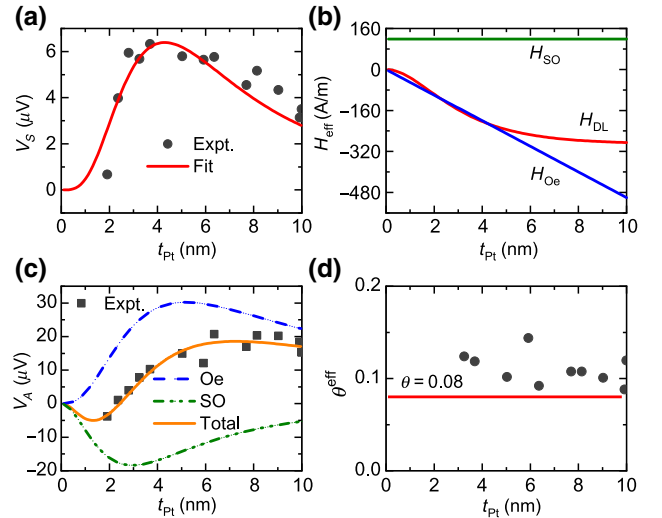


FIG. 3. Experimental and fitted amplitudes, from Eqs. (4)–(6), of symmetric, V_S , and antisymmetric, V_A , components to the signal, V_{mix} , are shown as functions of thickness t_{Pt} in (a) and (c), respectively. The contribution of each effective field is shown in (b). Effective spin Hall angle and spin Hall angle of Pt obtained from fitting Eq. (4) to the data are shown in (d).

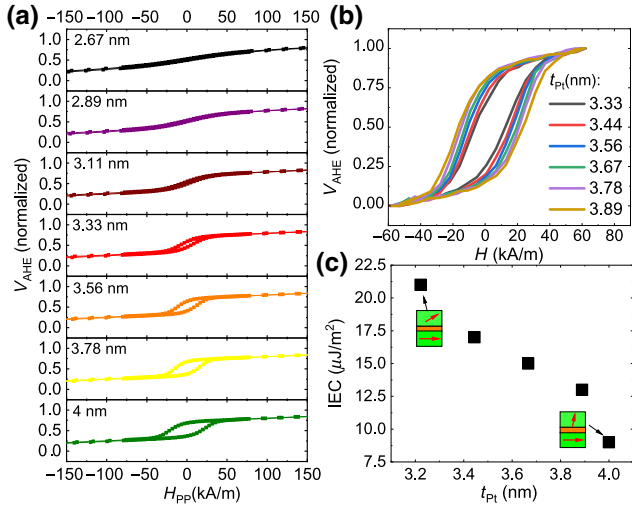


FIG. 4. AHE hysteresis loops measured in trilayers with different Pt spacer thicknesses (a). Open hysteresis loops are measured for $t_{\text{Pt}} > 3$ nm (b). IEC energy as a function of t_{Pt} is depicted in (c). The image presents effective magnetization direction in the top and bottom Co layers.

a bottom in-plane magnetized Co layer. Such symmetry breaking is essential for a field-free SOT-induced magnetization switching. Figures 5(a) and 5(b) present the magnetization state of the top Co (described with AHE voltage) as a function of an in-plane current (I) for different in-plane magnetic fields, when the magnetic field is increased (a) and decreased (b). The measurement protocol is the following: first, the sample is magnetized in a saturating negative magnetic field. Next, the field is set to -160 kA/m and the current is swept from 0 to -100 mA, then to positive 100 mA and back to 0 mA. Counterclockwise V_{AHE} versus I loops are measured with magnetic fields up to around 12 kA/m. Greater field values result in clockwise V_{AHE} versus I loops. Afterwards, the sample is magnetized in positive saturating magnetic field and V_{AHE} versus I loops are measured at H starting from 160 kA/m to -160 kA/m. In contrast to the previous case, clockwise loops change to counterclockwise at $H = -12$ kA/m. The switching current depends linearly on the magnetic field value according to Ref. [38]. The change in transition from 12 kA/m to -12 kA/m originates from the in-plane magnetized bottom Co switching, and is different than in the case of heterostructures using antiferromagnets [15].

The critical currents and current densities for several Pt thicknesses are summarized in Table II. As expected, the critical current needed to switch top Co magnetization without the external magnetic field decreases with increasing IEC energy.

Finally, we move on to the description of the analog SOT switching of a thin Co layer. As seen in SOT-switching experiments, AHE voltage changes

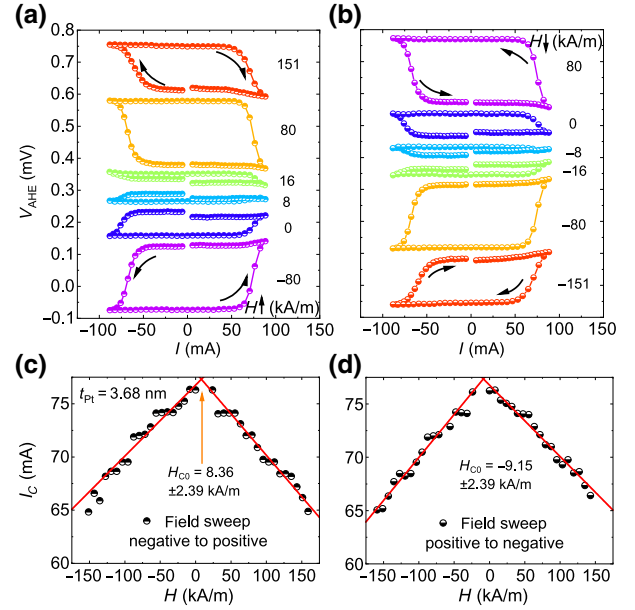


FIG. 5. SOT-induced switching process under different external magnetic fields for a trilayer with a spacer thickness of $t_{\text{Pt}} = 3.68$ nm. Hall voltage hysteresis loops as a function of in-plane current measured under various in-plane magnetic fields changed from negative to positive (a) and positive to negative (b) values. Corresponding critical currents for different fields are presented in (c),(d).

gradually with the current, in contrast to the current-induced switching required typically for digital memory applications [11]. Figure 6(a) presents Hall resistance $R_H = V_{\text{AHE}}/I$ of a trilayer with a Pt spacer thickness of $t_{\text{Pt}} = 3.2$ nm.

After initialization in a saturating perpendicular magnetic field, R_H changes from a minimal value of $R_{H-\text{min}} = -0.14 \Omega$ to around 0.07Ω upon negative current application. Note that maximal resistance for this spacer thickness is $R_{H-\text{max}} = 0.14 \Omega$, so no saturation is achieved during SOT switching. Sweeping the current from negative to positive values induces switching to a lower R_H ; however, only down to around $R_H = -0.07 \Omega$, which is above $R_{H-\text{min}}$. Therefore, during SOT-induced switching, the magnetization state is not reversed fully, but possibly

TABLE II. Summary of critical switching currents, I_{c0} , and current densities, J_{c0} , of Co/Pt/Co trilayers for different Pt thickness, t_{Pt} .

t_{Pt} (nm)	I_{c0} (mA)	J_{c0} (A/m ²)
3.7	77	$7.00 \cdot 10^{11}$
3.6	70	$6.50 \cdot 10^{11}$
3.4	61	$6.02 \cdot 10^{11}$
2.9	51	$5.95 \cdot 10^{11}$

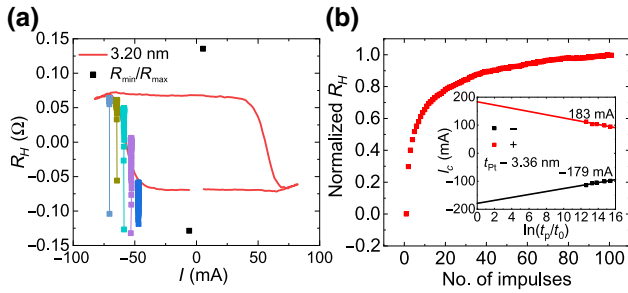


FIG. 6. Hall resistance loops as a function of current for $t_{Pt} = 3.2$ nm. Full black squares in (a) corresponds to the initial resistance after saturation in a magnetic field. Squares of different colors indicate the resistance state after application of up to a hundred current pulses of given amplitude. Normalized resistance after a different number of pulses of around 60-mA amplitude is presented in (b). Both (a),(b) highlight the neuromorphiclike behavior of the sample. Inset: the switching-current density dependence on the switching-pulse duration (t_p). t_0 is the inverse of the attempt frequency equal to 1 ns.

a magnetization domain state is formed. A detailed discussion on the switching mechanism in a similar stack is presented in Refs. [39] and [40]. Moreover, R_H depends also on the number of pulses of the same amplitude, as well as the pulse duration, Fig. 6(b). By decreasing the switching-pulse duration time (t_p) from 500 ms down to 500 μ s, the absolute value of the critical current increases according to Ref. [41]. Nonetheless, such a gradual change in Hall resistivity mimics the behavior of a neuron, whose resistive potential changes based on electrical signals delivered by synapses in an analog manner [42].

IV. SUMMARY

In summary, SOT-induced switching in the Co/Pt/Co structure with in-plane and perpendicular anisotropy of Co layers coupled ferromagnetically by the Pt spacer with varying thickness is investigated. The spin Hall angle and spin-diffusion length are determined using the SOT FMR method, the results of which are analyzed using the dedicated theoretical model. The coupling between two Co layers is tuned by the Pt spacer thickness and for intermediate thickness, 2.9 nm $< t_{Pt} < 3.7$ nm, field-free SOT-induced switching of the perpendicularly magnetized Co layer is observed. For a range of the Pt spacer thicknesses, gradual magnetization change with in-plane current is obtained, which may be useful for the hardware implementation of a spintronic neuromorphic network.

ACKNOWLEDGMENTS

This work is supported by the National Science Centre, Grant No. UMO-2015/17/D/ST3/00500, Poland. S.Z. acknowledges Grant No. LIDER/467/L-6/14/NCBR/2015 by the Polish National Centre for Research and

Development. S.L., Ł.K., K.G., and T.S. acknowledge National Science Centre Grant Spinorbitronics UMO-2016/23/B/ST3/01430. Nanofabrication is performed at the Academic Centre for Materials and Nanotechnology of AGH University of Science and Technology.

- [1] S. Bhatti, R. Sbiaa, A. Hirohata, H. Ohno, Sh. Fukami, and S. N. Piramanayagam, Spintronics based random access-memory: A review, *Mater. Today* **20**, 530 (2017).
- [2] J. C. Slonczewski, Current-driven excitation of magnetic multilayers, *J. Magn. Mater.* **159**, L1 (1996).
- [3] L. Berger, Emission of spin waves by a magnetic multilayer traversed by a current, *Phys. Rev. B* **54**, 9353 (1996).
- [4] S. Ikeda, J. Hayakawa, Y. Ashizawa, Y. M. Lee, K. Miura, H. Hasegawa, M. Tsunoda, F. Matsukura, and H. Ohno, Tunnel magnetoresistance of 604% at 300 K by suppression of Ta diffusion in CoFeB/MgO/CoFeB pseudo-spin-valves annealed at high temperature, *Appl. Phys. Lett.* **93**, 082508 (2008).
- [5] Y. Huai, F. Albert, P. Nguyen, M. Pakala, and T. Valet, Observation of spin-transfer switching in deep submicron-sized and low-resistance magnetic tunnel junctions, *Appl. Phys. Lett.* **84**, 3118 (2004).
- [6] S. Ikeda, K. Miura, H. Yamamoto, K. Mizunuma, H. D. Gan, M. Endo, S. Kanai, J. Hayakawa, F. Matsukura, and H. Ohno, A perpendicular-anisotropy CoFeB-MgO magnetic tunnel junction, *Nat. Mater.* **9**, 721 (2010).
- [7] M. Nakayama, T. Kai, N. Shimomura, M. Amano, E. Kitagawa, T. Nagase, M. Yoshikawa, T. Kishi, S. Ikegawa, and H. Yoda, Spin transfer switching in TbCoFe/CoFeB/MgO/CoFeB/TbCoFe magnetic tunnel junctions with perpendicular magnetic anisotropy, *J. Appl. Phys.* **103**, 07A710 (2008).
- [8] P. K. Amiri, Z. M. Zeng, J. Langer, H. Zhao, G. Rowlands, Y.-J. Chen, I. N. Krivorotov, J.-P. Wang, H. W. Jiang, J. A. Katine, Y. Huai, K. Galatsis, and K. L. Wang, Switching current reduction using perpendicular anisotropy in CoFeB-MgO magnetic tunnel junctions, *Appl. Phys. Lett.* **98**, 112507 (2011).
- [9] I. M. Miron, K. Garello, G. Gaudin, P.-J. Zermatten, M. V. Costache, S. Auffret, S. Bandiera, B. Rodmacq, A. Schuhl, and P. Gambardella, Perpendicular switching of a single ferromagnetic layer induced by in-plane current injection, *Nature* **476**, 189 (2011).
- [10] L. Liu, O. J. Lee, T. J. Gudmundsen, D. C. Ralph, and R. A. Buhrman, Current-Induced Switching of Perpendicularly Magnetized Magnetic Layers Using Spin Torque from the Spin Hall Effect, *Phys. Rev. Lett.* **109**, 096602 (2012).
- [11] L. Liu, C.-F. Pai, Y. Li, H. W. Tseng, D. C. Ralph, and R. A. Buhrman, Spin-torque switching with the giant Spin hall effect of tantalum, *Science* **336**, 555 (2012).
- [12] J. B. S. Mendes, R. O. Cunha, O. A. Santos, P. R. T. Ribeiro, F. L. A. Machado, R. L. Rodríguez-Suárez, A. Azevedo, and S. M. Rezende, Large inverse spin Hall effect in the antiferromagnetic metal Ir₂₀Mn₈₀, *Phys. Rev. B* **89**, 140406(R) (2014).

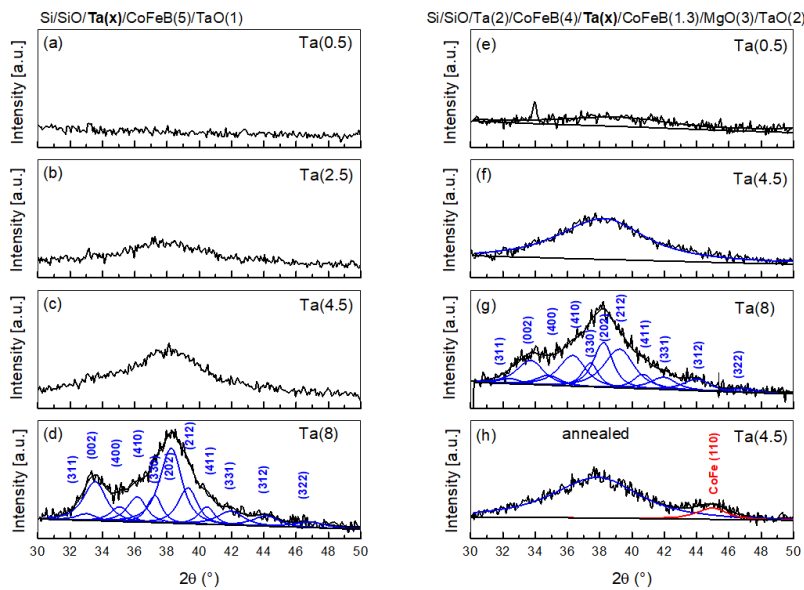
- [13] Y. Ou, S. Shi, D. C. Ralph, and R. A. Buhrman, Strong spin Hall effect in the antiferromagnet PtMn, *Phys. Rev. B* **93**, 220405(R) (2016).
- [14] Y.-W. Oh, S.-H. Ch. Baek, Y. M. Kim, H. Y. Lee, K.-D. Lee, Ch.-G. Yang, E.-S. Park, K.-S. Lee, K.-W. Kim, G. Go, J.-R. Jeong, B.-Ch. Mim, H.-W. Lee, K.-J. Lee, and B.-G. Park, Field-free switching of perpendicular magnetization through spin-orbit torque in antiferromagnet/ferromagnet/oxide structures, *Nat. Nanotechnol.* **11**, 878-884 (2016).
- [15] S. Fukami, C. Zhang, S. DuttaGupta, A. Kurenkov, and H. Ohno, Magnetization switching by spin-orbit torque in an antiferromagnet-ferromagnet bilayer system, *Nat. Mater.* **15**, 535 (2016).
- [16] D. Wu, G. Yu, C.-T. Chen, S. A. Razavi, Q. Shao, X. Li, B. Zhao, K. L. Wong, C. He, Z. Zhang, P. K. Amiri, and K. L. Wang, Spin-orbit torques in perpendicularly magnetized Ir₂₂Mn₇₈/Co₂₀Fe₆₀B₂₀/MgO multilayer, *Appl. Phys. Lett.* **109**, 222401 (2016).
- [17] S. A. Razavi, D. Wu, G. Yu, Y.-C. Lau, K. L. Wong, W. Zhu, C. He, Z. Zhang, J. M. D. Coey, P. Stamenov, P. K. Amiri, and K. L. Wang, Joule Heating Effect on Field-Free Magnetization Switching by Spin-Orbit Torque in Exchange-Biased Systems, *Phys. Rev. Appl.* **7**, 024023 (2017).
- [18] P. Baláz, M. Gmitra, and J. Barnaś, Current-induced dynamics in noncollinear dual spin valves, *Phys. Rev. B* **80**, 174404 (2009).
- [19] Y.-Ch. Lau, D. Betto, K. Rode, J. M. D. Coey, and P. Stamenov, Spin-orbit torque switching without an external field using interlayer exchange coupling, *Nat. Nanotechnol.* **11**, 758-762 (2016).
- [20] M. Matczak, R. Schafer, M. Urbaniak, B. Szymański, P. Kuświk, A. Jarosz, M. Schmidt, J. Aleksiejew, S. Jurga, and F. Stobiecki, Domain wall generated by graded interlayer coupling in Co/Pt/Co film with perpendicular anisotropy, *Appl. Phys. Lett.* **107**, 012404 (2015).
- [21] G. Yu, P. Upadhyaya, Y. Fan, J. G. Alzate, W. Jiang, K. L. Wong, S. Takei, S. A. Bender, L.-T. Chang, Y. Jiang, M. Lang, J. Tang, Y. Wang, Y. Tserkovnyak, P. K. Amiri, and K. L. Wang, Switching of perpendicular magnetization by spin-orbit torques in the absence of external magnetic fields, *Nat. Nanotechnol.* **9**, 548 (2014).
- [22] L. You, O.-J. Lee, D. Bhowmik, D. Labanowski, J. Hong, J. Bokor, and S. Salahuddin, Switching of perpendicularly polarized nanomagnets with spin orbit torque without an external magnetic field by engineering a tilted anisotropy, *Proc. Natl. Acad. Sci. U. S. A.* **112**, 10310 (2015).
- [23] S. Emori, U. Bauer, S. M. Ahn, E. Martinez, and G. S. D. Beach, Current-driven dynamics of chiral ferromagnetic domain walls, *Nat. Mater.* **12**, 611 (2013).
- [24] S. Woo, M. Mann, A. J. Tan, L. Garetta, and G. S. D. Beach, Enhanced spin-orbit torques in Pt/Co/Ta heterostructures, *Appl. Phys. Lett.* **105**, 212404 (2014).
- [25] J. Kanak, P. Wiśniowski, T. Stobiecki, A. Zaleski, W. Powroźnik, S. Cardoso, and P. P. Freitas, X-ray diffraction analysis and Monte Carlo simulations of CoFeB-MgO based magnetic tunnel junctions, *J. Appl. Phys.* **113**, 023915 (2013).
- [26] See Supplemental Material at <http://link.aps.org/supplemental/10.1103/PhysRevApplied.12.014006> for a detailed description of the structural characterization, the resistivity analysis and magnetisation saturation measurements.
- [27] M. Kawaguchi, D. Towa, Y.-C. Lau, S. Takahashi, and M. Hayashi, Anomalous spin Hall magnetoresistance in Pt/Co bilayers, *Appl. Phys. Lett.* **112**, 202405 (2018).
- [28] W. Skowroński, Ł. Karwacki, S. Ziętek, J. Kanak, S. ŁazarSKI, K. Grochot, T. Stobiecki, P. Kuświk, F. Stobiecki, and J. Barnaś, Determination of Spin Hall Angle in Heavy-Metal/Co-Fe-B-Based Heterostructures with Interfacial Spin-Orbit Fields, *Phys. Rev. Appl.* **11**, 024039 (2019).
- [29] J. Kim, P. Sheng, S. Takahashi, S. Mitani, and M. Hayashi, Spin Hall Magnetoresistance in Metallic Bilayers, *Phys. Rev. Lett.* **116**, 097201 (2016).
- [30] P. M. Haney, H.-W. Lee, K.-J. Lee, A. Manchon, and M. D. Stiles, Current induced torques and interfacial spin-orbit coupling: Semiclassical modeling, *Phys. Rev. B* **87**, 174411 (2013).
- [31] A. Kawasuso, Y. Fukaya, M. Maekawa, H. Zhang, T. Seki, T. Yoshino, E. Saitoh, and K. Takanashi, Current-induced spin polarization on a Pt surface: A new approach using spin-polarized positron annihilation spectroscopy, *J. Magn. Magn. Mater.* **342**, 139 (2013).
- [32] G. Allen, S. Manipatruni, D. E. Nikonov, M. Doczy, and I. A. Young, Experimental demonstration of the coexistence of spin Hall and Rashba effects in β -tantalum/ferromagnet bilayers, *Phys. Rev. B* **91**, 144412 (2015).
- [33] T. Koyama, Y. Guan, Y. Hibino, M. Suzuki, and D. Chiba, Magnetization switching by spin-orbit torque in Pt with proximity-induced magnetic moment, *J. Appl. Phys.* **121**, 123903 (2017).
- [34] T. A. Peterson, A. P. McFadden, C. J. Palmström, and P. A. Crowell, Influence of the magnetic proximity effect on spin-orbit torque efficiencies in ferromagnet/platinum bilayers, *Phys. Rev. B* **97**, 020403(R) (2018).
- [35] L. J. Zhu, D. C. Ralph, and R. A. Buhrman, Irrelevance of magnetic proximity effect to spin-orbit torques in heavy-metal/ferromagnet bilayers, *Phys. Rev. B* **98**, 134406 (2018).
- [36] J. C. Rojas-Sánchez, N. Reyern, P. Laczkowski, W. Savero, J. P. Attané, C. Deranlot, M. Jamet, J. M. George, L. Vila, and H. Jaffrès, Spin Pumping and Inverse Spin Hall Effect in Platinum: The Essential Role of Spin-Memory Loss at Metallic Interfaces, *Phys. Rev. Lett.* **112**, 106602 (2014).
- [37] M. Czapkiewicz, M. Żołądź, J. Wrona, P. Wiśniowski, R. Rak, T. Stobiecki, C. G. Kim, C. O. Kim, M. Takahashi, and M. Tsunoda, Magnetization process and domains in MTJ, *Phys. Status Solidi* **241**, 1477 (2004).
- [38] K.-S. Lee, S.-W. Lee, B.-C. Min, and K.-J. Lee, Threshold current for switching of a perpendicular magnetic layer induced by spin Hall effect, *Appl. Phys. Lett.* **102**, 112410 (2013).
- [39] M. Baumgartner, K. Garello, J. Mendil, C. O. Avci, E. Grimaldi, C. Murer, J. Feng, M. Gabureac, C. Stamm, Y. Acremann, S. Finizio, S. Wintz, J. Raabe, and P. Gambardella, Spatially and time-resolved magnetization

- dynamics driven by spin-orbit torques, *Nat. Nanotechnol.* **12**, 980 (2017).
- [40] M. M. Decker, M. S. Wörmle, A. Meisinger, M. Vogel, H. S. Körner, G. Y. Shi, C. Song, M. Kronseder, and C. H. Back, Time Resolved Measurements of the Switching Trajectory of Pt/Co Elements Induced by Spin-Orbit Torques, *Phys. Rev. Lett.* **118**, 257201 (2017).
- [41] H. Kubota, A. Fukushima, Y. Ootani, S. Yuasa, and K. Ando, Dependence of spin-transfer switching current on free layer thickness in Co-Fe-B/MgO/Co-Fe-B magnetic tunnel junctions, *Appl. Phys. Lett.* **89**, 032505 (2006).
- [42] P. Krzysteczko, G. Reiss, and A. Thomas, Memristive switching of MgO based magnetic tunnel junctions, *Appl. Phys. Lett.* **95**, 112508 (2009).

Magnetization dynamics in CoFeB/Ta/CoFeB system with mixed anisotropy

In this chapter, the author attached the second article [P7]: *Spin-orbit torque induced magnetization dynamics and switching in a CoFeB/Ta/CoFeB system with mixed magnetic anisotropy* which contains experiments similar to the first. This article shows the changing IEC strength extracted from SD-FMR measurements, structural characterization, and SOT induced switching with and without an external magnetic field. The author designed special microstrips that are specifically convenient for switching measurements, as seen in Fig.31.

The incident grazing x-ray diffraction (GIXD) profiles measured at different positions of the Ta wedges (x): 0.5nm, 2.5nm, 4.5nm and 8nm are shown in Fig.33. For both structures, the profiles of 4.5 nm thick Ta layers and below show a very broad low-intensity peak, indicating an amorphous-like disordered structure. On the other hand, the profiles of thicker Ta layer 8 nm contain peaks that originate from a polycrystalline tetragonal β phase of Ta¹²⁸. Annealing in vacuum at 300 °C for 10 min of the sample 4.5 nm thick Ta causes a partial crystallization of the amorphous CoFeB layer to the cubic CoFe phase, without changing the amorphous state of Ta layer. As in the case with the previous structure, the resistivities of CoFeB and Ta were extracted - see Fig.32 - from the Kawaguchi¹²⁹ model and values are 160 $\mu\Omega cm$ and 170 $\mu\Omega cm$, respectively.



Smit-Belgers¹³⁰ and LLG formulas allowed simulation of the IEC energy in which the change in the special characteristic behavior was observed. There are basically two regimes, ferromagnetic IEC and antiferromagnetic IEC, where the change from one regime to the other is around 1.3nm. The author showed that in the former regime



Figure 31: Designed stripes structure for SOT induced switching.

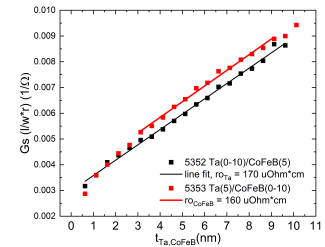


Figure 32: Sheet conductance dependence on Ta and CoFeB thickness.

¹²⁸ P. T. Moseley and C.J. Seabook. *Acta Crystal.*, B29(1170), 1973

¹²⁹ M. Kawaguchi et al. *Appl. Phys. Lett.*, 112(202405), 2018

Figure 33: The GIXD profiles measured at different positions of Ta wedge.

¹³⁰ S. Serrano-Guisan et al. *J. Appl. Phys.*, 110(023906), 2011d

the SOT-induced switching without any external magnetic field is possible. The sample structure - which can be seen in Fig.34 - is similar to the previous article and is based on the same principles.

The design of elements such as those in Fig.31 allows for variation in the SD-FMR measurement. For example, using perpendicular Hall electrodes (four-points of connections), where the standard two are for pumping current, and the second pair is for measuring the process as seen in Fig.35. Generally, for in-plane magnetized FM the two-point method shows a stronger SOT-FMR signal, while more suitable for FM with effective perpendicular magnetic anisotropy is the four-point method¹³¹. The two-point technique requires magnetoresistance in the form of AMR, GMR, SMR, or TMR, while the four-point method is based on PHE and AHE. Below, the spin-torque mixing voltage in conventional and transverse ST-FMR can be written as¹³²:

$$\begin{aligned} V_{XX}^{mix} &= \frac{I_{rf} R_{AMR}}{2\alpha\omega_+} \sin(2\phi) \cos(\phi) \\ &\times \left(S(H_{ext})\tau_{DL}^0 + A(H_{ext})\frac{\omega_2}{\omega} \tau_z^0 \right) \end{aligned} \quad (38)$$

where $S(H_{ext})$ and $A(H_{ext})$ are the symmetric and antisymmetric Lorentzian (see Eq.29), respectively. R_{AMR} includes contributions from both the AMR in the magnet and the SMR. $\omega_1 = \gamma H_0$, $\omega_2 = \gamma(H_0 + \mu_0 M_{eff})$ and $\omega_+ = \omega_1 + \omega_2$. $\tau_z^0 = \tau_{FL}^0 + \tau_{DL}^0$ where τ_{FL}^0 and τ_{DL}^0 are field-like and damping-like torques, respectively.

$$\begin{aligned} V_{XY}^{mix} &= V_{XY}^{mix} = -\frac{I_{rf} R_{PHE}}{2\alpha\omega_+} \cos(2\phi) \cos(\phi) \\ &\times \left(S(H_{ext})\tau_{DL}^0 + A(H_{ext})\frac{\omega_2}{\omega} \tau_z^0 \right) \\ &\quad + \frac{I_{rf} R_{AHE}}{2\alpha\omega_+} \cos(\phi) \\ &\times \left(S(H_{ext})\tau_z^0 + A(H_{ext})\frac{\omega_1}{\omega} \tau_{DL}^0 \right) \end{aligned} \quad (39)$$

In addition, the amplitudes of the symmetric and antisymmetric components of the total longitudinal and transverse ST-FMR signals have an angular dependence:

$$\begin{aligned} S_{XX}(\phi) &= \left(\frac{I_{rf}}{2\alpha\omega_+} R_{AMR} \tau_{DL}^0 - \frac{L}{2} E_{art}^0 \right) \sin(2\phi) \cos(\phi) \\ A_{XX}(\phi) &= \frac{I_{rf}}{2\alpha\omega_+} R_{AMR} \frac{\omega_2}{\omega} \tau_z^0 \sin(2\phi) \cos(\phi) \\ S_{XY}(\phi) &= -\left(\frac{I_{rf}}{2\alpha\omega_+} R_{PHE} \tau_{DL}^0 - \frac{W}{2} E_{art}^0 \right) \cos(2\phi) \cos(\phi) \\ &\quad + \left(\frac{I_{rf}}{2\alpha\omega_+} R_{AHE} \tau_z^0 - \frac{W}{2} E_{art}^0 \right) \cos(\phi) \\ A_{XY}(\phi) &= -\frac{I_{rf}}{2\alpha\omega_+} R_{PHE} \frac{\omega_2}{\omega} \tau_z^0 \cos(2\phi) \cos(\phi) \\ &\quad - \frac{I_{rf}}{2\alpha\omega_+} R_{AHE} \frac{\omega_1}{\omega} \tau_{DL}^0 \cos(\phi) \end{aligned} \quad (40)$$

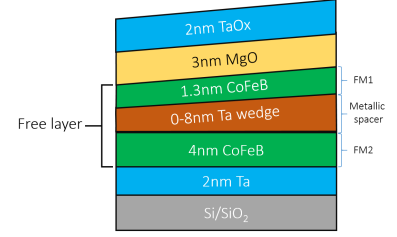


Figure 34: Structure illustration from article P3. FM1 coupled to FM2 via changing IEC.

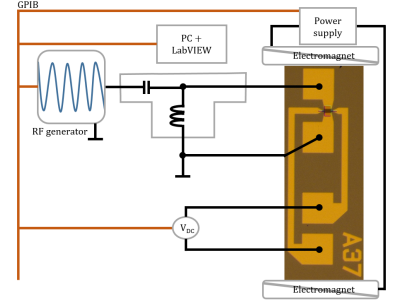


Figure 35: Illustration of four-point SD measurement setup. For the best signal, the sample is placed in 0° at azimuth angle

¹³¹ M. Harder et al. *Phys. Rep.*, 661(0370-1573):1-59, 2016b

¹³² S. Karimeddiny et al. *Phys. Rev. Appl.*, 14(024024), 2020c

The angle SD-FMR measurements for a comparison purposes were carried out at 5GHz, for the same sample stripe as can be seen in the Fig.36. The sample structure was as follows: W(5)/CoFeB(0-10)/MgO(2)/Ta(1) (layer thickness in nanometers).

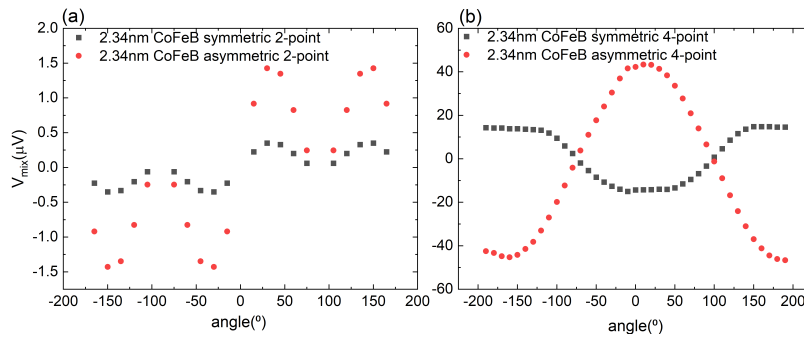


Figure 36: Symmetric and asymmetric part comparison of 2-point and 4-point measurement for 2.34nm CoFeB at 5GHz.

Several measurements in the new setup were performed for the paper attached below; a more detailed comparison of both methods is presented in *Appendix* in the chapter *SD-FMR setup measurements comparison*.


Spin-orbit torque induced magnetization dynamics and switching in a CoFeB/Ta/CoFeB system with mixed magnetic anisotropy

Stanisław Łazarski^{1,*}, Witold Skowroński^{1,†}, Krzysztof Grochot^{1,2}, Wiesław Powroźnik¹, Jarosław Kanak¹, Marek Schmidt³ and Tomasz Stobiecki^{1,2}

¹*Institute of Electronics, AGH University of Science and Technology, Al. Mickiewicza 30, 30-059 Kraków, Poland*

²*Faculty of Physics and Applied Computer Science, AGH University of Science and Technology, Al. Mickiewicza 30, 30-059 Kraków, Poland*

³*Institute of Molecular Physics, Polish Academy of Sciences, ul. Smoluchowskiego 17, 60-179 Poznań, Poland*

 (Received 25 June 2020; revised 22 March 2021; accepted 29 March 2021; published 15 April 2021)

Spin-orbit torque (SOT) induced magnetization switching in CoFeB/Ta/CoFeB trilayer with two ferromagnetic CoFeB layers exhibiting in-plane and perpendicular magnetic anisotropy (PMA), respectively, is investigated. Interlayer exchange coupling (IEC), measured using the ferromagnetic resonance technique is modified by varying thickness of the heavy metal Ta spacer (t_{Ta}). The evolution of the IEC with t_{Ta} leads to different orientations of the magnetic anisotropy axes of two CoFeB layers: for $t_{\text{Ta}} > 1.3$ nm, magnetization prefers antiferromagnetic alignment, whereas for $t_{\text{Ta}} < 1.3$ nm, ferromagnetic coupling is measured. The magnetization state of the CoFeB layer exhibiting PMA is controlled by the spin-polarized current originating from the Ta layer in micrometer sized Hall bars. The SOT induced critical current density with Ta spacer thickness is presented, showing an increase with decreasing t_{Ta} , which coincides with the CoFeB coercive field dependence. In a narrow range of t_{Ta} corresponding to the ferromagnetic IEC, the field-free SOT induced magnetization switching is achieved.

DOI: [10.1103/PhysRevB.103.134421](https://doi.org/10.1103/PhysRevB.103.134421)

I. INTRODUCTION

Conventional electronic devices based only on the electric charge are facing energy efficiency issues due to the use of high current densities needed to control the device state that dissipates a lot of heat. Moreover, digital data stored in the form of electric charge, for example, in dynamic and static random access memories are volatile and, thus, need periodic refreshment. Spintronic devices, on the other hand, use both charge and spin of the electron to process and store information. Magnetism-based spintronic elements are by nature nonvolatile and potentially more energy efficient, nonetheless, there is still a need for further development of magnetization control mechanisms [1]. Digital information can be encoded in the magnetization state of a nanoscale magnet in a non-volatile way. Research on various control mechanisms has recently received extensive attention due to the demand for a scalable and low-energy write and read processes [2]. Outstanding developments have been made in switching magnetic tunnel junctions (MTJs) and spin-valve structures via spin-transfer torque (STT) [3,4], electric fields [5,6], and recently vastly explored spin-orbit torque (SOT) [7–9]. MgO-based MTJs with in-plane magnetic anisotropy have been initially proposed as a main building block of a memory unit due to its high tunneling magnetoresistance ratio [10] and current induced switching [11]. Unfortunately, in general, STT-based devices require high critical current densities (J_C) via a thin

tunnel barrier for the magnetization switching and have the disadvantage of low thermal stability. Perpendicularly magnetized MTJs using both interface perpendicular magnetic anisotropy (PMA) [12–14] and shape anisotropy [15] have been proposed to enhance thermal stability and to reduce J_C , however, a MgO tunnel barrier can still degrade its own properties over time due to high switching currents. To overcome this problem, the SOT effect in which spin currents are generated in layers with high spin-orbit couplings, such as heavy metals (HMs) [16] and topological insulators [17] has been studied. The switching of the magnetization driven by SOT with PMA does not require such a high- J_C tunneling through a MgO barrier [16]. In addition, SOT induced magnetization switching enables the magnetization reorientation in the subnanosecond regime [18]. Originally, an external magnetic field had to be applied to assist SOT switching in order to break the time-reversal symmetry. Although the need for an external field in device applications would not be practical, therefore, numerous alternatives have been proposed, such as coupling to the antiferromagnets [19–25] or to another ferromagnet [26,27], use of interface torques [28], combination of STT and SOT effects [29], or using a dipolar field from an additional magnetic layer [30]. The use of a trilayer structure with two ferromagnets with different magnetic anisotropies coupled by a Ta layer forming a so-called T-type structure has led to the observation of robust field-free switching [31–33].

In this paper we study the $\text{Co}_{20}\text{Fe}_{60}\text{B}_{20}/\text{Ta}/\text{Co}_{20}\text{Fe}_{60}\text{B}_{20}$ trilayer structure in order to determine the coupling via the Ta spacer and SOT induced magnetization switching of CoFeB. Similar to Ref. [31] Ta serves as the coupling layer, but in the presented case it also acts as a source of the spin current.

*lazarski@agh.edu.pl

†skowron@agh.edu.pl

By carefully selecting the CoFeB layer thicknesses, the deposition condition, and the thermal treatment, we are able to control the magnetic anisotropy. The interlayer exchange coupling (IEC) [34] across a Ta spacer is investigated using the ferromagnetic resonance (FMR) measurements. This coupling induces different magnetic orientations of two CoFeB layers, which results in a nontrivial dependence of the switching field and critical SOT induced current dependence as a function of Ta thickness.

II. EXPERIMENT

All samples were magnetron sputtered on a thermally oxidized Si wafer with a wedged-shaped Ta layer deposited using a moving shutter technique. The investigated multilayer structure is as follows:

Ta(2)/Co₂₀Fe₆₀B₂₀(4)/Ta(t_{Ta})/Co₂₀Fe₆₀B₂₀(1.3)/MgO(3)/TaOx(2) (thickness in nanometers) with t_{Ta} varying from 0 to 8 nm. The bottom (thicker) and the top (thinner) Co₂₀Fe₆₀B₂₀ layers exhibit in-plane (IMA) and perpendicular magnetic anisotropy (PMA), respectively. Additional multilayers with single FM layers and variable thicknesses of Ta or CoFeB were deposited: Ta(0–10)/Co₂₀Fe₆₀B₂₀(5)/Ta(1) and Ta(5)/Co₂₀Fe₆₀B₂₀(0–10)/Ta(1) for resistivity analysis and PMA measurements using the anomalous Hall effect (AHE). Weak effective PMA of the top CoFeB layer was observed in the as-deposited state for a limited thickness of CoFeB around 1 nm. After annealing at 300 °C for 10 min, the range of CoFeB thicknesses for which effective PMA was found increased, which is confirmed by the evolution of the AHE signal in a half-stack with variable thickness of FM: Ta(5)/Co₂₀Fe₆₀B₂₀(0–2)/MgO(2)/Ta(1). The resistivity of CoFeB and Ta was determined in bilayers of variable thicknesses according to the model presented in Ref. [35]. After the deposition process, all samples were characterized by x-ray diffraction (XRD) and x-ray reflectivity measurements using a X'Pert-MPD diffractometer with a Cu anode to assist in controlling the thickness of particular layers in the system and phase analysis.

For the thinnest wedge thicknesses of $t_{\text{Ta}} < 2$ nm, the grazing incident angle profile measurements show no peaks. For $2 < t_{\text{Ta}} < 6$ nm, a broad peak corresponding to the amorphous Ta appears. Finally, for $t_{\text{Ta}} > 6$ nm the measurement results contain peaks that originate from a disoriented polycrystalline tetragonal β phase [36]. For more details see the Supplemental Material [37].

For magnetotransport measurements, the Hall bars along with the rectangular stripes were fabricated using 385-nm projection lithography, ion-beam etching, and the liftoff process. The elements dimensions were: $10 \mu\text{m} \times 100 \mu\text{m}$ for SOT dynamics measurements, $30 \mu\text{m} \times 10 \mu\text{m}$ stripes for current induced magnetization switching and Hall bars, and $10 \mu\text{m} \times 80 \mu\text{m}$ for AHE measurements. An example of the fabricated Hall bar with additional contact electrodes made of Al(20)/Au(30) is presented in Fig. 1. The long axes of the fabricated devices are perpendicular to the wedge direction, and the t_{Ta} variation within a single device is below 0.05 nm.

The AHE was measured in a perpendicular magnetic field with constant current flowing through the long axis of the Hall bar. Spin-orbit torque ferromagnetic resonance

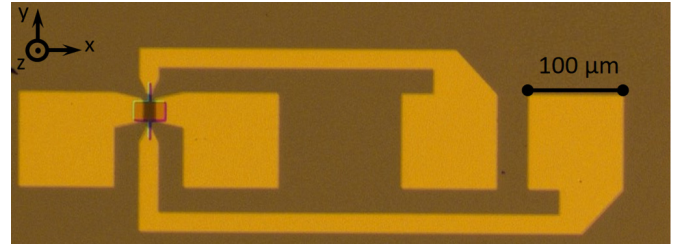


FIG. 1. Micrograph of the Hall-bar structure used for SOT current induced magnetization switching measurements.

(SOT-FMR)—with a rf signal of the constant frequency (f) applied where DC voltage was measured—was determined using the same electrodes (two-point) and perpendicular Hall electrodes (four-point) with the in-plane magnetic field (H) swept along a 45° axis with respect to the long axis of the stripe. In general, the stronger SOT-FMR signal is measured using the two-point method for in-plane magnetized CoFeB, whereas the four-point method is more suitable for CoFeB with effective perpendicular magnetic anisotropy Ref. [38].

III. RESULT AND DISCUSSION

A. Anomalous Hall effect

CoFeB and Ta layers resistivity determined in bilayers are as follows: $\rho_{\text{Ta}} = 170 \mu\Omega \text{cm}$ and $\rho_{\text{CoFeB}} = 160 \mu\Omega \text{cm}$. The presence of the PMA in thin CoFeB was confirmed by the AHE measurements. The maximum coercivity (H_C) was found for $t_{\text{CoFeB}} = 1.3\text{--}1.5$ nm. Thinner (thicker) CoFeBs are characterized by perpendicular (in-plane) magnetic anisotropy, which is shown in Fig. 2(a). Figure 2(b) presents the AHE loops evolution of CoFeB/Ta/CoFeB trilayers as a function of the Ta spacer thickness.

Clearly, the magnetic behavior of the top CoFeB layer is modulated by the spacer thickness. For t_{Ta} below 0.7 nm, the

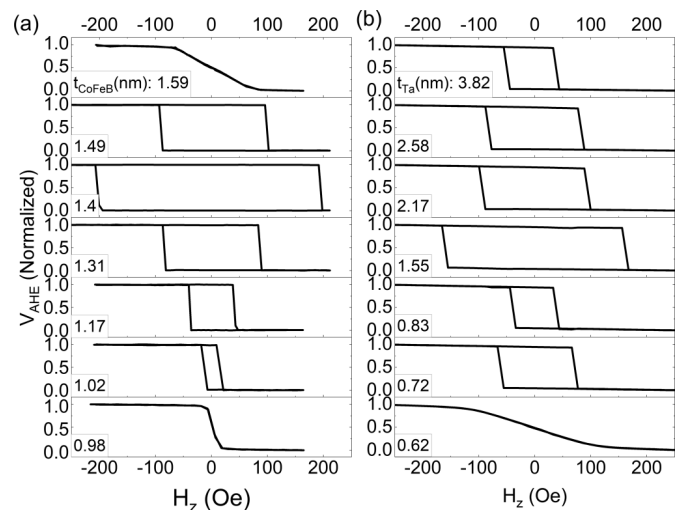


FIG. 2. AHE hysteresis loops measured in (a) a bilayer with a single FM as a function of CoFeB thickness: Ta(5)/CoFeB(0–2)/MgO(2)/Ta(1), (b) trilayers with two FM layers separated by different Ta spacer thicknesses: Ta(2)/CoFeB(5)/Ta(0–8)/CoFeB(1)/MgO(2)/Ta(1). Both samples were annealed at 300 °C.

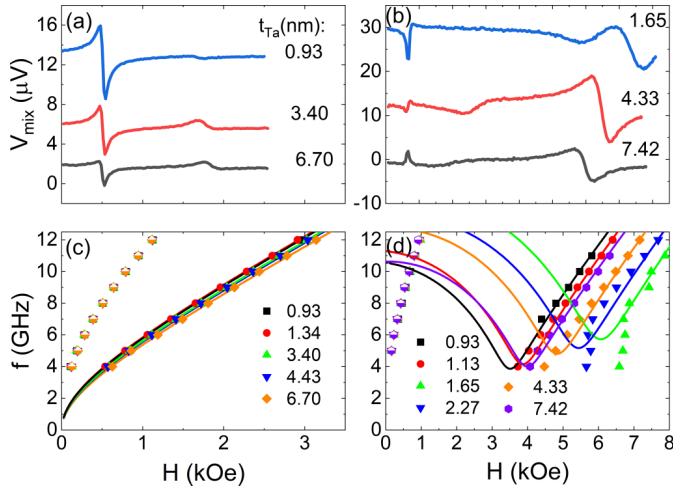


FIG. 3. Ferromagnetic resonance measurements on Hall-bar devices with different t_{Ta} 's. (a) and (b) show exemplary SOT-FMR curves for 8 GHz in as-deposited and 10 GHz in annealed states, respectively. The Kittel relation, i.e., the resonance frequency vs magnetic-field dependence of IMA CoFeB (open symbols) and PMA CoFeB (full symbols) for both cases are presented in (c) and (d). Macrospin simulation results are drawn with solid lines.

hard-axis closed hysteresis loop corresponding to the strong ferromagnetic coupling to the bottom in-plane magnetized CoFeB layer is measured. For thicker Ta the H_C of the top CoFeB is modulated, which is a signature of the antiferromagnetic coupling of different energies as proposed in Ref. [39].

However, the magnetization switching process in micron-scale Hall bars is determined by the domain nucleation and propagation, therefore, precise determination of the coupling energy is challenging. Moreover, conventional magnetometry cannot be used for the determination of the IEC energy in the presented case where magnetic anisotropy axes of two CoFeB layers are orthogonal. For this purpose, we performed SOT-FMR measurements of the coupled CoFeB/Ta/CoFeB system.

B. Interlayer exchange coupling

Representative SOT-FMR spectra measured for a trilayer in an as-deposited and annealed state are presented in Figs. 3(a) and 3(b). Two peaks in the magnetic-field domain correspond to the resonance frequency of the in-plane magnetized thick CoFeB (low field) and out-of-plane magnetized thin CoFeB (high field). The extracted signal V_{mix} consists of two parts—symmetric and antisymmetric—which are modeled by Lorentz curves,

$$V_{\text{mix}} = V_S \frac{\Delta H^2}{\Delta H^2 + (H - H_0)^2} + V_A \frac{\Delta H(H - H_0)}{\Delta H^2 + (H - H_0)^2}, \quad (1)$$

where V_S (V_A) is the magnitude of symmetrical (antisymmetrical) Lorentz curve, ΔH is the linewidth, and H_0 is the resonance field.

Figures 3(c) and 3(d) present the $f(H)$ dependencies measured for different thicknesses of the Ta spacers. Strong dependence of the resonance peak on t_{Ta} is observed in the annealed sample, which indicates that the coupling is greatly

enhanced after the thermal treatment [40]. It was found in the XRD measurements, that after the annealing process, the intensity of the Ta peak increases together with the appearance of the peak from CoFeB, which indicates an improvement of the crystallization process. Detailed crystallographic analysis is presented in the Supplemental Material [37].

The $f(H)$ dependence was analyzed using the macrospin model as follows. First, taking into account the saturation magnetization M_S of each layer, magnetic anisotropy energy (K), and the coupling energy between them, the total energy term was minimized, which resulted in the orientation of the magnetization vector of two CoFeB layers. Next, the FMR frequency of each layer was calculated based on Smit-Beljers resonance formula, which resulted in two theoretical $f(H)$ dependencies Ref. [41].

It was assumed, that for the thickest Ta spacer, the IEC energy is negligibly small and the experimental points were fitted by adjusting the anisotropy energy alone. Parameters used in the modeling were as follows: $\mu_0 M_{S1} = 1.4$ and $\mu_0 M_{S2} = 0.5$ T for the bottom and top CoFeBs were measured using a vibrating sample magnetometer, the anisotropy energies were determined from an independent electrical transport measurement (anomalous Hall effect and magnetoresistance—see in detail in the Supplemental Material [37]): $K_{A1} = 5 \times 10^3$ and $K_{A2} = 1.75 \times 10^5$ J/m³ for the bottom and top CoFeB layers, respectively. The magnetic anisotropy values of the bottom and top CoFeB layers correspond to the effective anisotropies of $K_{\text{eff}1} = 7.73 \times 10^5$ and $K_{\text{eff}2} = -7.58 \times 10^4$ J/m³ based on Eq. (2),

$$K_{\text{eff}} = \frac{\mu_0 M_s^2}{2} - K_A, \quad (2)$$

where μ_0 is the vacuum permeability.

Next, in order to model the experimental $f(H)$ dependencies for the entire range of t_{Ta} , the coupling was adjusted. However, it was found that changing the IEC energy [Fig. 4(b)] alone results in the values of an order of magnitude higher than in previous studies Refs. [42,43] and deviation of the FMR frequency of the thick CoFeB. Therefore, the best fits were obtained by adjusting both the coupling and the anisotropy energies for all t_{Ta} 's investigated. We note that neighboring layer thickness can influence the anisotropy of CoFeB as presented in Ref. [44]. In a similar material system it was found that the anisotropy field of the perpendicularly magnetized FeCoB layer was influenced by the Ta underlayer thickness [45], which was crucial for STT-magnetic random access memory (MRAM) cells based on a similar structure [46]. The detailed simulations based on the Landau-Lifshitz-Gilbert equation together with experimental data are presented in the Supplemental Material [37]. The simulation results are gathered in Figs. 4(a) and 4(b).

C. SOT induced switching

After the analysis of the coupling energy, we now turn to the SOT induced switching experiments. Similar to the previous work [27] we used the HM both as a spacer and as a source of the spin current. Unlike in the Co/Pt/Co case where strong ferromagnetic coupling [47] and field-free magnetization switching [27] were observed, the CoFeB/Ta/CoFeB did not result in a field-free switching in the antiferromagnetic

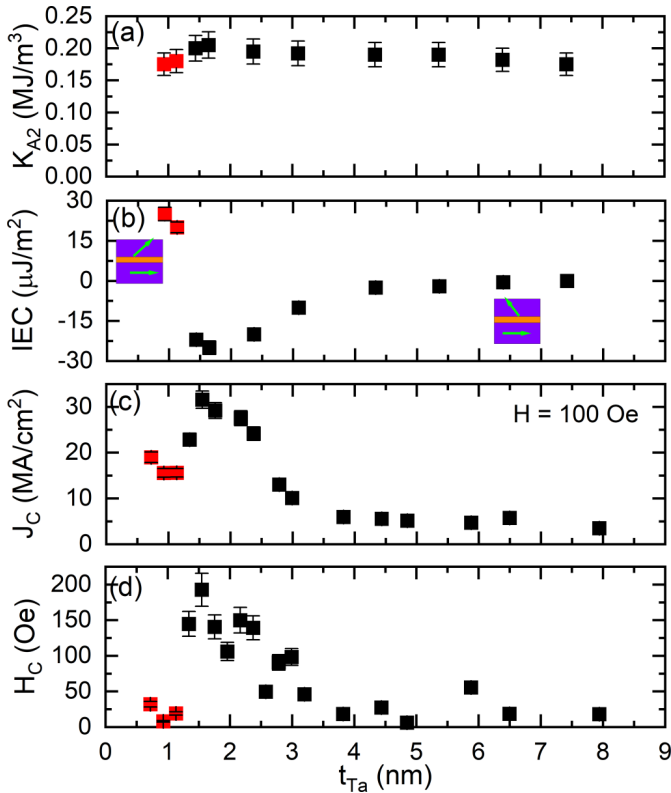


FIG. 4. Dependence of the magnetic anisotropy of the (a) top CoFeB- K_{A2} , (b) IEC energy via Ta spacer, (c) critical current density J_C , and the (d) top CoFeB coercive field H_C as a function of t_{Ta} . The red point corresponds to the ferromagnetic IEC range.

coupling region. The example of the switching process with the assistance of the external magnetic field is presented in Fig. 5(a). The J_C dependence on t_{Ta} in the external field $H_x = 100$ Oe applied along the long axis of the Hall bar is presented in Fig. 4(c). The behavior closely resembles the coercive field dependence on t_{Ta} .

J_C needed to switch the top CoFeB magnetization in the presence of an external magnetic field is increasing with decreasing Ta spacer thickness along with a rise in negative coupling energy until the transition to the ferromagnetic coupling for $t_{Ta} = 1.3$ nm occurs. The Hall-bar

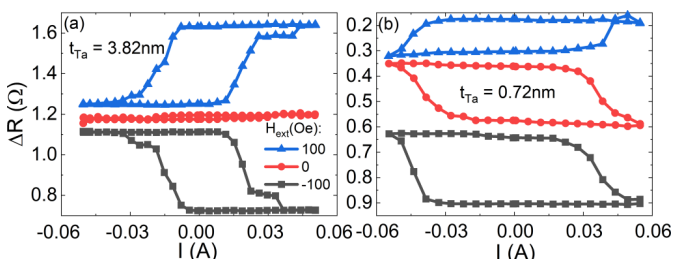


FIG. 5. SOT induced switching with (a) t_{Ta} corresponding to the antiferromagnetic coupling and (b) ferromagnetic coupling in different external magnetic fields. Field-free switching is measured only for the sample characterized by the ferromagnetic coupling between two CoFeB electrodes. The offset is artificially added for clear viewing.

switches deterministically only in the in-plane magnetic field ($H = \pm 100$ Oe in the presented example). On the contrary, in the ferromagnetic coupling region, we observed current induced switching without any external magnetic field—Fig. 5(b)—but not fully complete—due to precisely selected ferromagnetic coupling (similar to Ref. [27]). The incomplete magnetization switching is most probably caused by the magnetic domain formation in the top CoFeB.

A ferromagnetic coupling appears only in a narrow Ta spacer thickness range. The switching process in this case may also be induced by the spin current from the bottom Ta layer. To further elucidate the field-free switching we calculated the current densities in each layer. For $t_{Ta} = 0.72$ nm, J_C in the bottom Ta layer is 1.58×10^{11} A/m², which is enough to switch the in-plane magnetized CoFeB layer [16]. Due to ferromagnetic coupling between two CoFeB layers, this leads to the magnetization change in thin CoFeB.

Alternatively, the spin current generated by the anomalous Hall effect [48] in thick CoFeB or its interface with Ta may also lead to a field-free switching of the perpendicular magnetized top CoFeB [28]. Nevertheless, in both scenarios due to a limited range of Ta spacer thickness for which the ferromagnetic coupling is observed, there is a need for an additional spin-current source layer in order to realize magnetic field-free switching.

IV. SUMMARY

To sum up, the dynamics and the switching process in CoFeB/Ta/CoFeB trilayers with in-plane and perpendicular magnetic anisotropies of the two ferromagnets were investigated. The IEC, determined by the SOT-FMR technique was tuned by varying Ta spacer thickness and changes from ferromagnetic ($t_{Ta} < 1.3$ nm) to antiferromagnetic ($1.3 \text{ nm} < t_{Ta}$). In the antiferromagnetic regime, a small external magnetic field is needed to achieve the SOT switching. In the ferromagnetic regime, however, the field-free SOT switching is obtained, but the range of change in resistance is slightly reduced. The implementation of two coupled FM layers with mixed anisotropies separated by a HM spacer enables determination of the fundamental SOT mechanisms and could advance the development of field-free SOT-MRAM devices in the future.

ACKNOWLEDGMENTS

This work was supported by the National Science Centre, Grant No. UMO-2015/17/D/ST3/00500, Poland. W.S. acknowledges Grant No. LIDER/467/L-6/14/NCBR/2015 from the Polish National Centre for Research and Development. S.Ł., K.G., and T.S. acknowledge National Science Centre Grant No. Spinorbitronics UMO-2016/23/B/ST3/01430. Nanofabrication was performed at the Academic Centre for Materials and Nanotechnology of AGH University of Science and Technology. We would like to express our gratitude to Prof. F. Stobiecki, Dr. M. Czapkiewicz, and Dr. S. Ziętek for helpful discussions on data analysis.

- [1] S. Ikiegawa, F. B. Mancoff, J. Janesky, and S. Aggarwal, Magnetoresistive random access memory: Present and future, *IEEE Trans. Electron Devices* **67**, 1407 (2020).
- [2] S. Bhatti, R. Sbiaa, A. Hirohata, H. Ohno, S. Fukami, and S. N. Piramanayagam, Spintronics based random access memory: A review, *Mater. Today* **20**, 530 (2017).
- [3] J. C. Slonczewski, Current-driven excitation of magnetic multilayers, *J. Magn. Magn. Mater.* **159**, L1 (1996).
- [4] L. Berger, Emission of spin waves by a magnetic multilayer traversed by a current, *Phys. Rev. B* **54**, 9353 (1996).
- [5] H. Ohno, D. Chiba, F. Matsukura, T. Omiya, E. Abe, T. Dietl, Y. Ohno, and K. Ohtani, Electric-field control of ferromagnetism, *Nature (London)* **408**, 944 (2000).
- [6] S. Kanai, M. Yamanouchi, S. Ikeda, Y. Nakatani, F. Matsukura, and H. Ohno, Electric field-induced magnetization reversal in a perpendicular-anisotropy CoFeB-MgO magnetic tunnel junction, *Appl. Phys. Lett.* **101**, 122403 (2012).
- [7] I. M. Miron, K. Garello, G. Gaudin, P.-J. Zermatten, M. V. Costache, S. Auffret, S. Bandiera, B. Rodmacq, A. Schuhl, and P. Gambardella, Perpendicular switching of a single ferromagnetic layer induced by in-plane current injection, *Nature (London)* **476**, 189 (2011).
- [8] L. Liu, O. J. Lee, T. J. Gudmundsen, D. C. Ralph, and R. A. Buhrman, Current-Induced Switching of Perpendicularly Magnetized Magnetic Layers Using Spin Torque from the Spin Hall Effect, *Phys. Rev. Lett.* **109**, 096602 (2012).
- [9] S. Emori, U. Bauer, S. M. Ahn, E. Martinez, and G. S. D. Beach, Current-driven dynamics of chiral ferromagnetic domain walls, *Nature Mater.* **12**, 611 (2013).
- [10] S. Ikeda, J. Hayakawa, Y. Ashizawa, Y. M. Lee, K. Miura, H. Hasegawa, M. Tsunoda, F. Matsukura, and H. Ohno, Tunnel magnetoresistance of 604% at 300K by suppression of Ta diffusion in CoFeB/MgO/CoFeB pseudo-spin-valves annealed at high temperature, *Appl. Phys. Lett.* **93**, 082508 (2008).
- [11] Y. Huai, F. Albert, P. Nguyen, M. Pakala, and T. Valet, Observation of spin-transfer switching in deep submicron-sized and low-resistance magnetic tunnel junctions, *Appl. Phys. Lett.* **84**, 3118 (2004).
- [12] M. Nakayama, T. Kai, N. Shimomura, M. Amano, E. Kitagawa, T. Nagase, M. Yoshikawa, T. Kishi, S. Ikiegawa, and H. Yoda, Spin transfer switching in TbCoFe/CoFeB/MgO/CoFeB/TbCoFe magnetic tunnel junctions with perpendicular magnetic anisotropy, *J. Appl. Phys.* **103**, 07A710 (2008).
- [13] S. Ikeda, K. Miura, H. Yamamoto, K. Mizunuma, H. D. Gan, M. Endo, S. Kanai, J. Hayakawa, F. Matsukura, and H. Ohno, A perpendicular-anisotropy CoFeB-MgO magnetic tunnel junction, *Nature Mater.* **9**, 721 (2010).
- [14] P. K. Amiri, Z. M. Zeng, J. Langer, H. Zhao, G. Rowlands, Y.-J. Chen, I. N. Krivorotov, J.-P. Wang, H. W. Jiang, J. A. Katine, Y. Huai, K. Galatsis, and K. L. Wang, Switching current reduction using perpendicular anisotropy in CoFeB-MgO magnetic tunnel junctions, *Appl. Phys. Lett.* **98**, 112507 (2011).
- [15] K. Watanabe, B. Jinnai, S. Fukami, H. Sato, and H. Ohno, Shape anisotropy revisited in single-digit nanometer magnetic tunnel junctions, *Nat. Commun.* **9**, 663 (2018).
- [16] L. Liu, C.-F. Pai, Y. Li, H. W. Tseng, D. C. Ralph, and R. A. Buhrman, Spin-torque switching with the giant spin hall effect of tantalum, *Science* **336**, 555 (2012).
- [17] M. DC, R. Grassi, J.-Y. Chen, M. Jamali, D. R. Hickey, D. Zhang, Z. Zhao, H. Li, P. Quarterman, Y. Lv, M. Li, A. Manchon, K. A. Mkhoyan, T. Low, and J.-P. Wang, Room-temperature high spin-orbit torque due to quantum confinement in sputtered $Bi_xSe_{(1-x)}$ films, *Nature Mater.* **17**, 800 (2018).
- [18] E. Grimaldi, V. Krizakova, G. Sala, F. Yasin, S. Couet, G. S. Kar, K. Garello, and P. Gambardella, Single-shot dynamics of spin-orbit torque and spin transfer torque switching in three-terminal magnetic tunnel junctions, *Nat. Nanotechnol.* **15**, 111 (2020).
- [19] J. B. S. Mendes, R. O. Cunha, O. A. Santos, P. R. T. Ribeiro, F. L. A. Machado, R. L. Rodríguez-Suárez, A. Azevedo, and S. M. Rezende, Large inverse spin Hall effect in the antiferromagnetic metal $Ir_{20}Mn_{80}$, *Phys. Rev. B* **89**, 140406(R) (2014).
- [20] Y. Ou, S. Shi, D. C. Ralph, and R. A. Buhrman, Strong spin Hall effect in the antiferromagnet PtMn, *Phys. Rev. B* **93**, 220405(R) (2016).
- [21] Y.-W. Oh, S.-H. C. Baek, Y. M. Kim, H. Y. Lee, K.-D. Lee, Ch.-G. Yang, E.-S. Park, K.-S. Lee, K.-W. Kim, G. Go, J.-R. Jeong, B.-Ch. Mim, H.-W. Lee, K.-J. Lee, and B.-G. Park, Field-free switching of perpendicular magnetization through spin-orbit torque in antiferromagnet/ferromagnet/oxide structures, *Nat. Nanotechnol.* **11**, 878 (2016).
- [22] S. Fukami, C. Zhang, S. DuttaGupta, A. Kurenkov, and H. Ohno, Magnetization switching by spin-orbit torque in an antiferromagnet-ferromagnet bilayer system, *Nature Mater.* **15**, 535 (2016).
- [23] D. Wu, G. Yu, C.-T. Chen, S. A. Razavi, Q. Shao, X. Li, B. Zhao, K. L. Wong, C. He, Z. Zhang, P. K. Amiri, and K. L. Wang, Spin-orbit torques in perpendicularly magnetized $Ir_{22}Mn_{78}/Co_{20}Fe_{60}B_{20}/MgO$ multilayer, *Appl. Phys. Lett.* **109**, 222401 (2016).
- [24] S. A. Razavi, D. Wu, G. Yu, Y.-C. Lau, K. L. Wong, W. Zhu, C. He, Z. Zhang, J. M. D. Coey, P. Stamenov, P. K. Amiri, and K. L. Wang, Joule Heating Effect on Field-Free Magnetization Switching by Spin-Orbit Torque in Exchange-Biased Systems, *Phys. Rev. Appl.* **7**, 024023 (2017).
- [25] K. Grochot, Ł. Karwacki, S. Łazarski, W. Skowroński, J. Kanak, W. Powroźnik, P. Kuświk, M. Kowacz, F. Stobiecki, and T. Stobiecki, Current-Induced Magnetization Switching of Exchange-Biased NiO Heterostructures Characterized by Spin-Orbit Torque, *Phys. Rev. Appl.* **15**, 014017 (2021).
- [26] Y. Liu, B. Zhou, and J.-G. Zhu, Field-free Magnetization Switching by Utilizing the Spin Hall Effect and Interlayer Exchange Coupling of Iridium, *Sci. Rep.* **9**, 325 (2019).
- [27] S. Łazarski, W. Skowroński, J. Kanak, Ł. Karwacki, S. Ziętek, K. Grochot, T. Stobiecki, and F. Stobiecki, Field-Free Spin-Orbit Torque Switching in Co/Pt/Co Multilayer with Mixed Magnetic Anisotropies, *Phys. Rev. Appl.* **12**, 014006 (2019).
- [28] S.-H. C. Baek, V. P. Amin, Y.-W. Oh, G. Go, S.-J. Lee, G.-H. Lee, K.-J. Kim, M. D. Stiles, B.-G. Park, and K.-J. Lee, Spin currents and spin-orbit torques in ferromagnetic trilayers, *Nature Mater.* **17**, 509 (2018).
- [29] M. Wang, W. Cai, D. Zhu, Z. Wang, J. Kann, Z. Zhao, K. Cao, Z. Wang, Y. Zhang, T. Zhang, C. Park, J.-P. Wang, A. Fert, and W. Zhao, Field-free switching of a perpendicular magnetic tunnel junction through the interplay of spin-orbit and spin-transfer torques, *Nat. Electron.* **1**, 582 (2018).
- [30] V. Krizakova, K. Garello, E. Grimaldi, G. S. Kar, and P. Gambardella, Field-free switching of magnetic tunnel junctions

- driven by spin-orbit torques at sub-ns timescales, *Appl. Phys. Lett.* **116**, 232406 (2020).
- [31] W. J. Kong, C. H. Wan, X. Wang, B. S. Tao, L. Huang, C. Fang, C. Y. Guo, Y. Guang, M. Irfan, and X. F. Han, Spin-orbit torque switching in a T-type magnetic configuration with current orthogonal to easy axes, *Nat. Commun.* **10**, 233 (2019).
- [32] G. Yu, P. Upadhyaya, Y. Fan, J. G. Alzate, W. Jiang, K. L. Wong, S. Takei, S. A. Bender, L.-T. Chang, Y. Jiang, M. Lang, J. Tang, Y. Wang, Y. Tserkovnyak, P. K. Amiri, and K. L. Wang, Switching of perpendicular magnetization by spin-orbit torques in the absence of external magnetic fields, *Nat. Nanotechnol.* **9**, 548 (2014).
- [33] L. You, O.-J. Lee, D. Bhowmik, D. Labanowski, J. Hong, J. Bokor, and S. Salahuddin, Switching of perpendicularly polarized nanomagnets with spin orbit torque without an external magnetic field by engineering a tilted anisotropy, *Proc. Natl. Acad. Sci. USA* **112**, 10310 (2015).
- [34] S. S. P. Parkin, N. More, and K. P. Roche, Oscillations in Exchange Coupling and Magnetoresistance in Metallic Superlattice Structures: Co/Ru, Co/Cr, and Fe/Cr, *Phys. Rev. Lett.* **64**, 2304 (1990).
- [35] M. Kawaguchi, D. Towa, Y.-C. Lau, S. Takahashi, and M. Hayashi, Anomalous spin Hall magnetoresistance in Pt/Co bilayers, *Appl. Phys. Lett.* **112**, 202405 (2018).
- [36] M. Cecot, Ł. Karwacki, W. Skowroński, J. Kanak, J. Wrona, A. Żywczak, L. Yao, S. van Dijken, J. Barnaś, and T. Stobiecki, Influence of intermixing at the Ta/CoFeB interface on spin Hall angle in Ta/CoFeB/MgO heterostructures, *Sci. Rep.* **7**, 968 (2017).
- [37] See Supplemental Material at <http://link.aps.org/supplemental/10.1103/PhysRevB.103.134421> for more details.
- [38] M. Harder, Y. Gui, and C.-M. Hu, Electrical detection of magnetization dynamics via spin rectification effects, *Phys. Rep.* **661**, 1 (2016).
- [39] S. S. P. Parkin, Systematic Variation of the Strength and Oscillation Period of Indirect Magnetic Exchange Coupling through the *3d*, *4d*, and *5d* Transition Metals, *Phys. Rev. Lett.* **67**, 3598 (1991).
- [40] Y. Liu, L. Hao, and J. Cao, Effect of annealing conditions on the perpendicular magnetic anisotropy of Ta/CoFeB/MgO multilayers, *AIP Adv.* **6**, 045008 (2016).
- [41] S. Serrano-Guisan, W. Skowroński, J. Wrona, N. Liebing, M. Czapkiewicz, T. Stobiecki, G. Reiss, and H. W. Schumacher, Inductive determination of the optimum tunnel barrier thickness in magnetic tunneling junction stacks for spin torque memory applications, *J. Appl. Phys.* **110**, 023906 (2011).
- [42] C.-W. Cheng, C. H. Shiue, T.-I. Cheng, and G. Chern, Observation of parallel-antiparallel magnetic coupling in ultrathin CoFeB-MgO based structures with perpendicular magnetic anisotropy, *J. Appl. Phys.* **112**, 033917 (2012).
- [43] K. Wang, L. Qian, S.-C. Ying, and G. Xiao, Manipulation of the interlayer exchange coupling in perpendicular magnetized thin films via tunable magnetic-layer and spacer thicknesses, *Phys. Rev. B* **102**, 144430 (2020).
- [44] D. D. Lam, F. Bonell, S. Miwa, Y. Shiota, K. Yakushiji, H. Kubota, T. Nozaki, A. Fukushima, S. Yuasa, and Y. Suzuki, MgO overlayer thickness dependence of perpendicular magnetic anisotropy in CoFeB thin films, *J. Korean Phys. Soc.* **62**, 1461 (2013).
- [45] V. Sokalski, M. T. Moneck, E. Yang, and J.-G. Zhu, Optimization of Ta thickness for perpendicular magnetic tunnel junction applications in the MgO-FeCoB-Ta system, *Appl. Phys. Lett.* **101**, 072411 (2012).
- [46] D. C. Worledge, G. Hu, D. W. Abraham, J. Z. Sun, P. L. Trouilloud, J. Nowak, S. Brown, M. C. Gaidis, E. J. O'Sullivan, and R. P. Robertazzi, *Appl. Phys. Lett.* **98**, 022501 (2011).
- [47] A. Bonda, S. Uba, L. Uba, W. Skowroński, T. Stobiecki, and F. Stobiecki, Laser-induced magnetization precession parameters dependence on Pt spacer layer thickness in mixed magnetic anisotropies Co/Pt/Co trilayer, *J. Magn. Magn. Mater.* **505**, 166702 (2020).
- [48] S. Iihama, T. Tanihuchu, K. Yakushiji, A. Fukushima, Y. Shiota, S. Tsunegi, R. Hiramatsu, S. Yuasa, Y. Suzuki, and H. Kubota, Spin-transfer torque induced by the spin anomalous Hall effect, *Nat. Electron.* **1**, 120 (2018).

Harmonic Hall voltage measurements in Pt-Ti/CoFeB system

The use of materials with a high SOT effect due to its high charge current j to spin current conversion j_S has been studied frequently. Nowadays this effect is quantified using the $\theta_{SH} = j_S/j$ [^{133,134}]. In order to determine its value - as mentioned before - there are several methods available such as FMR lineshape analysis¹³⁵, harmonic Hall voltage measurement^{136,137}, Kerr-effect-based optical determination¹³⁸, SMR¹³⁹ and threshold current magnetization switching¹⁴⁰. In this chapter, the author presents an experimental protocol for the detailed measurement of spin Hall efficiency based on dynamic electrical measurements. Here, the selected structure is composed of two conventional samples of Pt: Ta(1)/Pt(t_{Pt})/Fe₆₀Co₂₀B₂₀(2)/Ta(2) (thickness in nm) with t_{Pt} varying from 4 to 16 nm, and Pt-Ti: Ta(1)/[Pt(d)/Ti(0.2)] m /Pt(d)/Fe₆₀Co₂₀B₂₀(2)/Ta(2), where $(m + 1) \times d = 6$ nm for 3, 5 and 7 interlayers. Both samples were deposited and annealed at 310°C in an ultra-high vacuum chamber. Multilayers were patterned in $200 \times 30 \mu\text{m}^2$ stripes for resistance measurements and $30 \times 10 \mu\text{m}^2$ for transport characterization. The optical lithography, lift-off, and ion-beam etching processes were used. In the second step of lithography, contact electrodes consisting of Ti(5) / Au(50) were manufactured.

For transport measurement, the Hall voltage signal was measured in both out-of-plane and in-plane magnetic fields using low-frequency stimulation (2387 Hz) of 1V. Current and current density ranged from 2.2 to 10 mA and 5.2 to 7.2 MA/cm², respectively, based on the resistance of the sample. In the measurement of FMR, the 16 dBm modulated amplitude RF signal was applied to the long axis of the stripe and the measurement of V_{mix} using short axis electrodes with a synchronized lock-in amplifier with the modulating signal. As for harmonic Hall voltage measurement, it was performed in a fixed external magnetic field where the sample was laying on a rotating stage with an RF-multiprobe from T-plus attached. A stepper motor driven by a dedicated linear controller controlled the mechanical rotation of the stage.

Patterned devices with different thicknesses of HM were used to determine the resistivity. As in the previous structures, the resistance (R) was transformed into the sheet conductance:

$$G_S = \frac{l}{wR} \quad (41)$$

where l and w are the length and width of the stripe, respectively. The resistivity of HM was then calculated as follows:

$$\rho_{HM} = \frac{t_{HM}}{G_S - G_0} \quad (42)$$

where $G_0 = 0.0011$ S is the sheet conductance of the multilayer without HM buffer. The results can be seen in the Tab.3.

SD-FMR measurements allowed for the determination of the damping parameter α . In plane magnetic field was swept for different in-

θ_{SH} - spin Hall angle

¹³³ I. M. Miron et al. *Nat.*, 476(189-193), 2011a

¹³⁴ L. Liu et al. *Sci.*, 336(55), 2012

¹³⁵ L. Liu et al. *Phys. Rev. Lett.*, 106(036601), 2011c

¹³⁶ J. Kim et al. *Nat. Mater.*, 12(240-245), 2013a

¹³⁷ M. Hayashi et al. *Phys. Rev. B*, 89(144425), 2014b

¹³⁸ C. Stamm et al. *Phys. Rev. Lett.*, 119(087203), 2017b

¹³⁹ H. Nakayama et al. *Phys. Rev. Lett.*, 110(206601), 2013c

¹⁴⁰ Q. Hao et al. *Phys. Rev. Appl.*, 3(034009), 2015a

$t_{Pt}/$ Pt-Ti intf.	Pt			Pt-Ti			units
		5.6	10	14	3	5	7
ρ_{HM}	52	34	24	54	60	95	$\mu\Omega cm$

put frequencies ranging from 4 to 12 GHz, which as a result gave the family of Lorentz-shaped curves fitted to formula Eq.37 (see Fig.37a). The Kittel relation (the resonance frequency vs resonance magnetic-field dependence) which can be seen in Fig.37b was fitted using the Kittel formula from Eq.31.

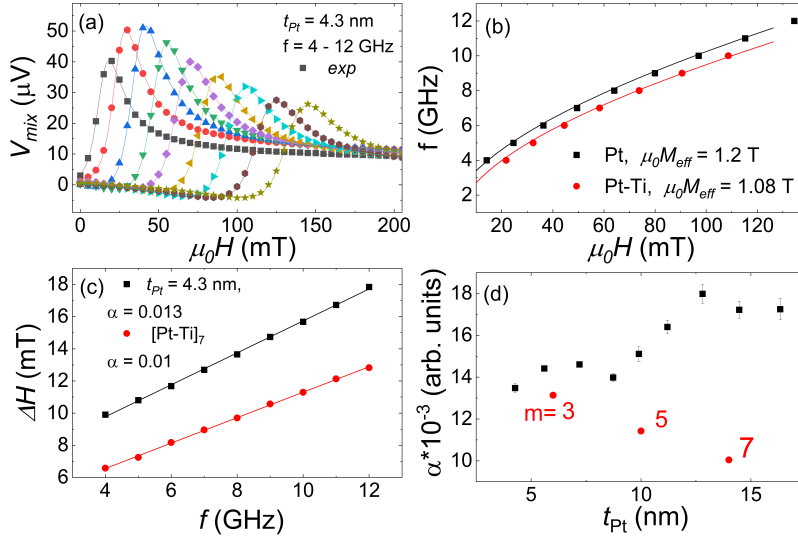


Figure 37: (a) Example of the SD-FMR measured for different excitation frequency for the Hall-bar with $t_{Pt} = 4.3$ nm. (b) Dispersion relation for Pt ($t_{Pt} = 4.3$ nm) and Pt-Ti ($m = 7$) underlayers modeled using Kittel formula. (c) FMR linewidth in function of frequency together with a line fit. (d) α reliance on t_{Pt} and number of Pt-Ti interfaces.

Harmonic Hall voltage measurements were performed in the rotating in-plane magnetic field to determine the spin Hall efficiency¹⁴¹. To describe the Hall spin efficiency, the following formula was incorporated¹⁴²:

$$\zeta_{DL(FL)} = \frac{2e\mu_0 M_S t_{FeCoB} H_{DL}(FL)}{j\hbar} \quad (43)$$

The spin Hall efficiencies as a function of the HM layer were obtained. In the case of Pt, ζ_{DL} reaches a maximum at 5 nm and decreases with thickening of the HM layer similarly to [143,144]. The Oersted field was determined by $H_{Oe} = Jt_{Pt}/2$. From the calculation it is shown that the determined ζ_{DL} overtop the field-like contribution what implicate that the amplitude of both H_{FL} and H_{Oe} is similar but of opposite signs. ζ_{FL} is smaller than ζ_{DL} for thin Pt but rises with thickening Pt layer.

For the purpose of determining the θ_{SH} , the interface transparency is needed, however, firstly, the absorption of the spin current should be calculated from:

$$g_{eff}^{\uparrow\downarrow} = \frac{4\pi M_S t_{FeCoB}}{g\mu_B} (\alpha_{eff} - \alpha_0) \quad (44)$$

where g is the Lande factor, μ_B is the Bohr magneton and $\alpha_0 =$

Table 3: Exemplary resistivity extracted from samples.

¹⁴¹ A. O. Avci et al. *Phys. Rev. B*, 90 (224427), 2014e

¹⁴² M.-H.Nguyen et al. *Phys. Rev. Lett.*, 116(126601), 2016d

¹⁴³ M.-H.Nguyen et al. *Phys. Rev. Lett.*, 116(126601), 2016d

¹⁴⁴ C. F. Pai et al. *Phys. Rev. B*, 92 (064426), 2015d

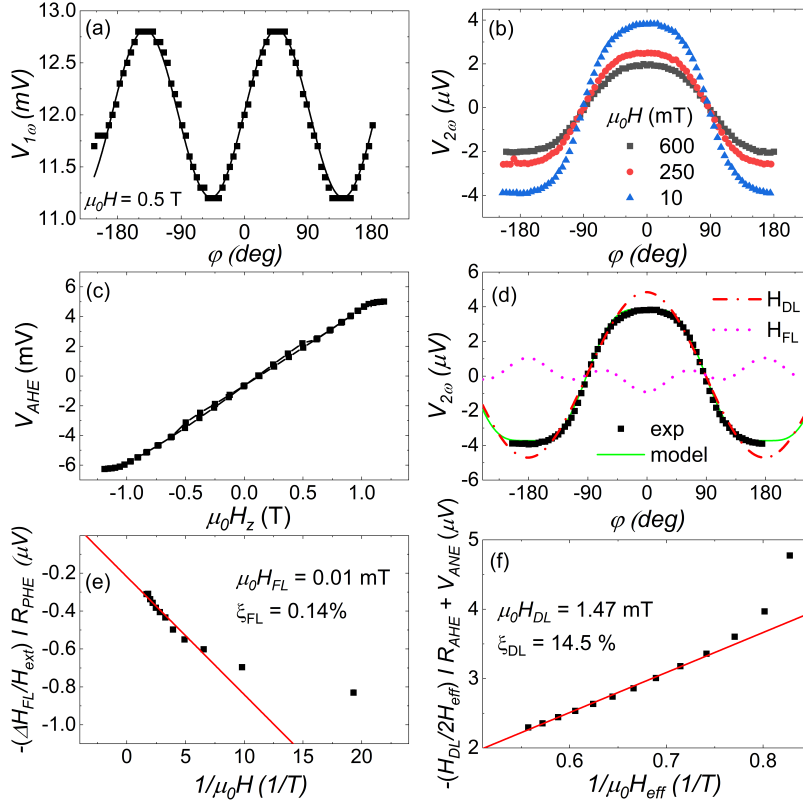


Figure 38: (a) First and (b) second harmonic component in function of in plane magnetic field for $t_{Pt} = 4.3$ nm. (c) AHE measurement. (d) Modeled using Eq. 28 second harmonic Hall voltage. (e) H_{FL} in function of inversed applied magnetic field. (f) H_{DL} in function of inversed effective magnetic field.

0.004 is the intrinsic damping of the FM layer. As the results show, $g_{eff}^{\uparrow\downarrow}$ factor increases with thickening t_{Pt} and decreases with a number of Pt-Ti interfaces, which is the reason for the increase (decrease) of the damping value. As mentioned, the interface transparency formula is as follows:

$$T = \frac{g_{eff}^{\uparrow\downarrow} \tanh \frac{t_{HM}}{2\lambda_{HM}}}{g_{eff}^{\uparrow\downarrow} \coth \frac{t_{HM}}{2\lambda_{HM}} + \frac{h}{\rho_{HM}\lambda_{HM}2e^2}} \quad (45)$$

where λ_{HM} is the spin diffusion length and h is the Planck constant. The calculated transparency varies between 0.42 and 0.5 for Pt/FeCoB and Pt-Ti/FeCoB interfaces. Lastly, the spin Hall angle was calculated: $\theta_{SH} = \zeta_{DL}/T$, and the spin Hall conductivity was calculated as follows: $\sigma_{SH} = \zeta_{SH}/\rho_{HM}$. The spin Hall efficiencies range from 0.17 to 0.05 depending on the HM thickness and results are presented in Fig. 39.

SOT-FMR signal line-shape analysis which was based on [145] showed similar values. The intrinsic spin Hall angle depends on the spin diffusion length and spin mixing conductance, as it is a function of the interface transparency. As was shown, T varies from 0.5 and 0.4 and therefore the results of θ_{SH} range from 0.35 to 0.12 - see below Tab. 4.

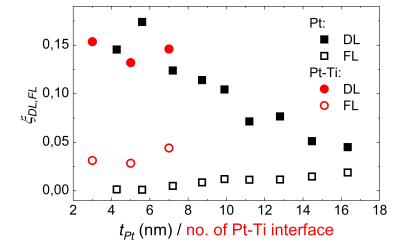


Figure 39: The spin Hall efficiencies for all devices.

¹⁴⁵ D. MacNeill et al. *Nat. Phys.*, 13(300-305), 2017c

$t_{Pt}/$ Pt-Ti intf.	Pt			Pt-Ti			units
	5.6	10	14	3	5	7	nm/no.
T	0.5	0.46	0.42	0.48	0.44	0.51	
θ_{HM}	0.35	0.23	0.12	0.36	0.34	0.32	
σ_{HM}	3.3	3.07	2.13	3.2	2.6	1.75	$10^5/(\Omega m)$

Table 4: Summary of interface transparency, spin Hall angle and spin Hall conductivity.

Summary and Outlook

One of the key issues in the field of spintronics is to switch the magnetization without any external magnetic field to make it usable in a practical application. To do so, an understanding of magnetization dynamics at the nanoscale is essential. The conducted research presented in this thesis aimed to focus on the understanding of the field-free magnetization switching and dynamics of the designed and fabricated spintronic multilayers. The obtained results in the presented work and by many other laboratories in the world show a great potential for spin electronics in the application in the future computing devices. Nevertheless, this relatively young scientific field still needs to develop experimental tools for studying magnetization dynamic properties, which in the future will allow these phenomena to be applied to various technologies. Presented experimental techniques, such as VNA-FMR or SD-FMR allowed detection of multiple resonance peak in different multilayer system and thus, supported by theoretical analysis, extraction of important magnetic and electric parameters of the prototype devices. The influence of IEC on the magnetization dynamics was observed. Successfully used the SD-FMR technique in the region of 5-12 GHz, even up to 20 GHz, for research on the dynamics of magnetization. One of the main highlights of the research was utilization of two FM layers with different anisotropy, coupled by a material that also serves as the source of the spin current, to experimentally show the field-free-switching. Further study, should lead to miniaturization of the devices to nm-scale and reducing the time and switching current, which allows for application in the real, high-density memory devices.

The low-frequency harmonic Hall voltage measurement and its analysis of the spin-dependent phenomena in HM/FM bilayer system enabled careful analysis of the spin-orbit torques. This setup allowed for examining an intrinsic spin Hall angle along with spin Hall conductivity which were among the highest values reported. Good agreement was achieved between the experimental data and the theoretical predictions. Moreover, research confirmed the fact that Pt continues to be one of the most attractive materials for spintronics use. Nevertheless, further improvement of the spin-to-charge conversion should be reached in order to enable switching energy reduction. One possible direction is the utilization of the topological insulators¹⁴⁶, 2D van der Waals materials¹⁴⁷ or oxide materials¹⁴⁸.

¹⁴⁶ Y.T. Fan et al. *Sci. Rep.*, 12(2998), 2022b

¹⁴⁷ H. Yang et al. *Nat.*, 606(663), 2022c

¹⁴⁸ F. Trier et al. *Nat. Rev. Mat.*, 7(258), 2022d

Appendix

SD-FMR setup measurements comparison

For the purpose of obtaining field-free switching along with comparing both sets of more, the following structure was measured $\text{Si}/\text{SiO}_2/\text{Ta}(2)/\text{CoFeB}(5)/\text{W}(t_W)/\text{CoFeB}(1)/\text{MgO}(2)/\text{TaOx}(1)$ where t_W ranged from 0 to 10 nm. First, there are two extreme regions taken into account for the thicknesses of HM of 1.16nm and 9.15nm , which makes it possible to see the difference for both measurement systems. For the first case (Fig.41a), where both FM layers are strongly coupled, the first large peak can be seen for the thick layer with in-plane anisotropy. The second peak for the thin layer is shifted to the upper fields for a 2-point system, and it is small, barely visible. With even higher fields and a smaller sample signal, it may happen that it is not noticed. For comparison, the second measurement system (Fig.41b) shows that the signal from the second peak is quite substantial, demonstrating the advantage of this technique for thin FM layers. As can also be seen, for the thicker HM layer, the signal difference begins to decrease, although we can see that the signal from the first peak is slightly reduced, but not so much that this has a significant difference in reading the signal. The signal from the second peak is still greater than that of the basic measuring system, despite the already considerable layer thickness, the separation of both FMs due to thick HM.

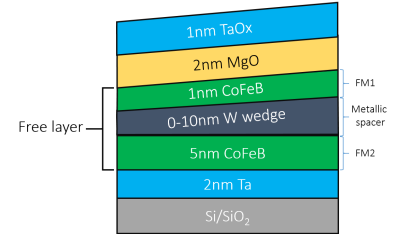
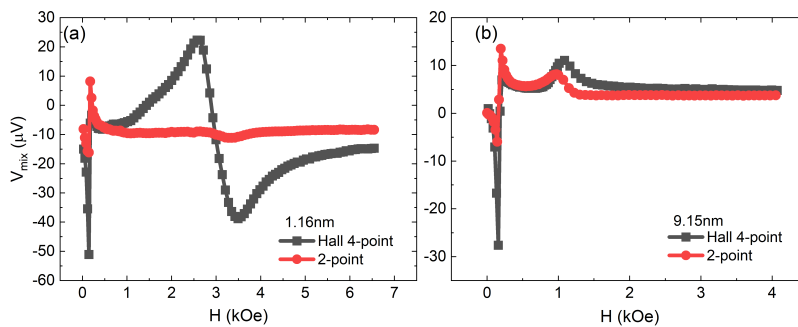


Figure 40: Structure of sample with W as HM and CoFeB as FM.

Figure 41: Comparison between two setup measurements. (a) for 1.16nm of HM and (b) for 9.15nm. Both measurements' frequency was set at 5GHz. 2-point setup was measured at 45° and for 4-point at 0° in azimuth angle.

Next, the angular measurement was then made for the 4-point method. In Fig.42 the exemplary signal for SD-FMR measurement as a function of the azimuth angle. The strongest signal is achieved when the angle is 0° or 180° while the lowest is at 90° and -90° .

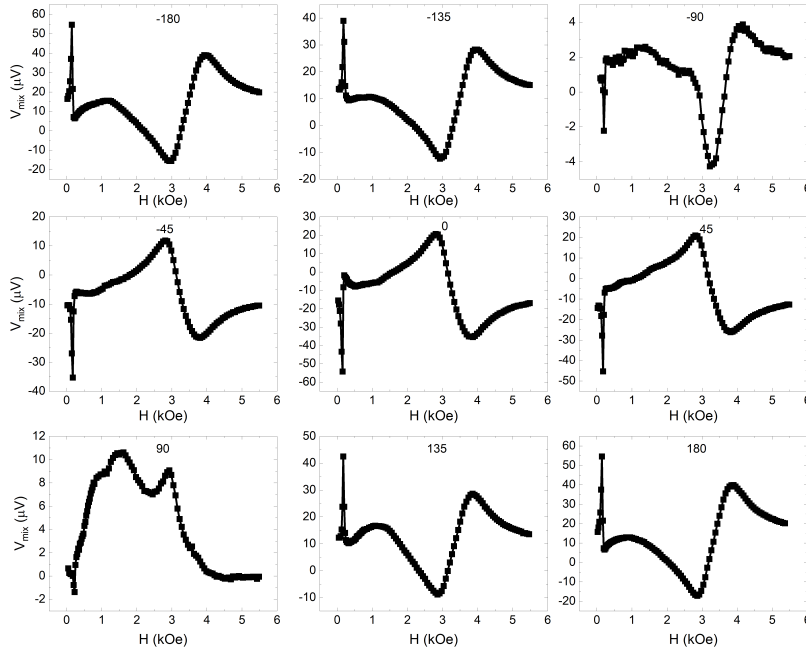


Figure 42: Exemplary angle measurements of 4-point SD-FMR measurement.

The resonance fields were obtained along with the components of the symmetric and asymmetric parts of the Lorentz curve depending on the angle of the sample plane - Fig.43. Separately, for the thicker and thinner layers, it can be seen that both the resonance field and both Lorentz component parts are quite characteristic. However, it should be mentioned that the magnetic field in which the measurement was performed was not the saturating field for the thinner layer.

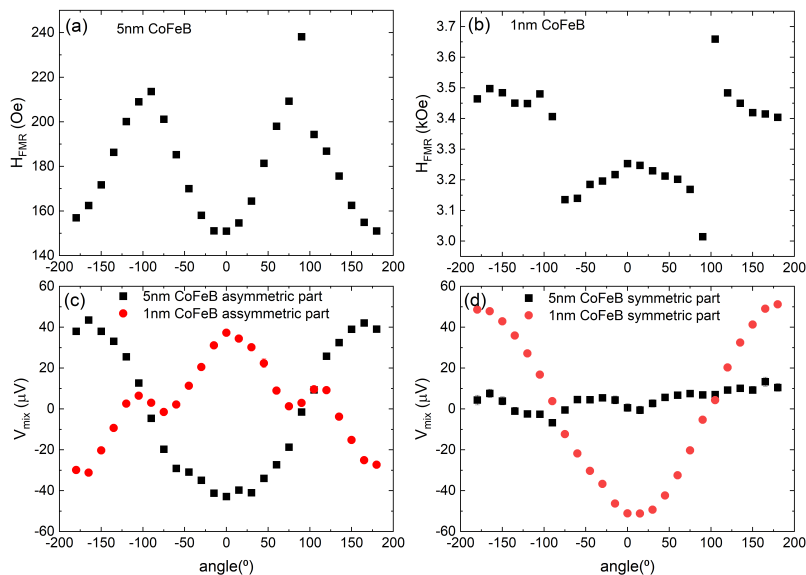


Figure 43: For 4-point measurements. Changing resonance field in azimuth angle for thick (a) and thin (b) FM layer in trilayer structure. (c) and (d) are symmetric and asymmetric part for both FM layers, respectively. All measurements were held at 5GHz.

Clearly, for measurements at such thin layers, one can see a better signal and resolution for this variation of the setup. The resistivities for W and CoFeB were extracted the same as for the rest structures

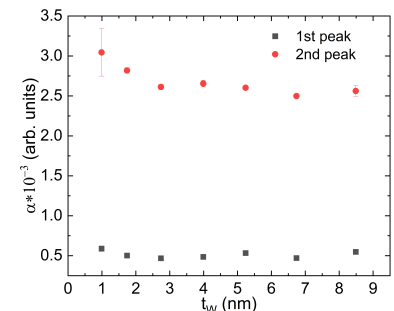


Figure 44: Damping parameter extracted from SD measurements.

and were $\rho_W = 110\mu\Omega cm$ and $\rho_{CoFeB} = 171\mu\Omega cm$. Moreover, the damping parameter was extracted for both FM layers and is stable for all thicknesses of the W wedge (see Fig.44) As written before, here the measurement setup for SD-FMR was 4-point Hall which allowed for better peak resolution in this layer regime and the measurements show two peaks, which come from both CoFeB layers. In the case of switching measurements without the use of an external magnetic field, the obtained results were not sufficient for any further investigation.

Lithography

The microfabrication and nanofabrication laboratories available at the AGH Academic Center for Materials and Nanotechnology are made up of two clean rooms certified by ISO-5 and ISO-7 standards equipped with the Raith eLINE Plus Electron Beam lithography system, Durham Magneto Optic Ltd. MicroWriter ML3 and IonSYS 500 for magnetron sputtering and ion etching integrated in one machine from Roth & Rau microsystems. In addition, a wet bench with spin coater, ultrasonic washer, and hot plate integrated in the chemical processing bench is present. In most microfabrication and nanofabrication processes, the dust content in the air is an important factor in the success of the manufacturing process.

The eLINE Plus system (see Fig.45) contains an interferometry feedback sample stage, which allows the position of the sample to be controlled with a repeat of up to 1 nm. Six different apertures are available (7.5, 10, 20, 30, 60, 120 μm), allowing an appropriate selection of the accuracy and speed of exposure, which are directly proportional to the beam current. The eLINE Plus system allows both the imaging of a sample and the exposure of a mask previously designed, but to operate properly, a high vacuum is needed.

The MicroWriter ML3 (see Fig.46) which uses computer-controlled optics to project the exposure pattern directly onto the photoresist, is an option on the eLINE Plus system. In comparison, it allows for much faster exposure and, moreover, does not need any vacuum to operate, but at the cost of accuracy. It is also possible to mix the different sample-structuring steps between the two exposure systems.

The IonSYS 500 (see Fig.47) has a load lock chamber, thereby significantly reducing the waiting time of the process vacuum. After the pumping process, the sample is transferred to the main chamber using a mechanical robotic arm and placed on a rotating head. During the deposition or etching processes, the head can rotate around its normal axis and its azimuth angle can be tilted, which is particularly useful during an etching procedure. In addition, the system has an integrated mass spectrometer that allows the depth of etching to be controlled over time. In the case of multilayer stacks, mass spectrometers act as end-point detectors, allowing accurate stopping of etching at the required depth. In deposition mode, deposition of



Figure 45: eLINE Plus Electron Beam lithography system from Raith.



Figure 46: MicroWriter ML3 from Durham Magneto Optic Ltd.



Figure 47: IonSYS 500 with integrated etching and magnetron sputtering system from Roth & Rau microsystems.

Al, Ti and Au elements is accessible or insulators when oxygen flows through the chamber. The typical microfabrication process consists of several steps and is described below:

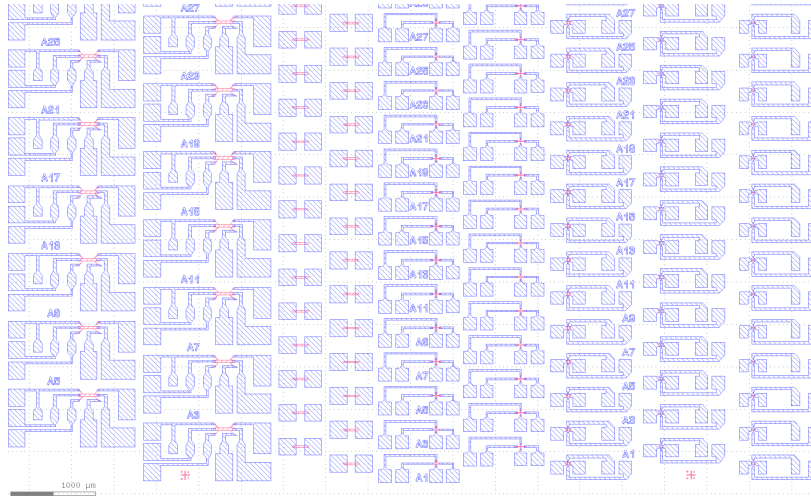


Figure 48: Exemplary mask developed for nanolithography process. Red and blue color correspond to an active area and contact electrodes respectively

The samples are cleaned with ethanol to remove surface contamination. Then in the next step, depending on the structure and intent of the sample, whether it is an MTJ junction or other multilayer structure, the process is carried out in a two- or three-step technique, with electron lithography or photolithography used separately for each step.

In the standard two-step method, the sample is covered with negative photoresist (AR-N 4340) and centrifuged in a spin coater using 6000 RPM. Then, the photoresist on the sample is hardened on the hot plate at 90°C for 1 min. The next step is light exposure of the design pattern in MicroWriter ML3 - see the exemplary design in Fig.48. The developed pattern is exposed to $140\text{ mJ}/\text{cm}^2$ with a dose of 4. To determine the appropriate dose to be exposed, dose tests have been performed before. After the procedure has been completed, the sample is placed again on a hot plate in 95°C for 2 min. The patterned mask has special corners markings that allow positioning in the next manufacturing step using a four-point correction method. The development process of the photoresist is performed in AR 300 475 for 20s. Subsequently, the physical ion-beam etching of the sample is being held under the power of 200 W with an Ar flow of 8 sccm. As mentioned above, control of the depth of etching is done using a mass spectrometer. Complete removal of the remaining photoresist is carried out in 1-methyl-2-pyrrolidinone or simply called Sigma with ultrasounds at 70°C from 15 min up to 1 hour. After microscopic examination, the second step of lithography starts with the application of a mask of electric contact pads. This time positive photoresist (3740 P) is applied and baked on a hot plate at 100°C for 1 min. Then after exposure at a dose of 0.5, AR 300 47 removes the exposed photoresist for 10 s. The etching procedure takes about half a minute, and then the contact pads of Ti/Au are sput-

tered. The magnetron sputtering Ti has an Ar flow rate of 50 sccm and a magnetron power of 50 W while Au has an Ar flow of 69 sccm and a power of 40 W lasting 4 min and 8 min, respectively. Finally, the sample is placed again in Sigma with ultrasounds at 70°C and cleaned in ethanol and dried in stream of nitrogen.

The three-step technique starts similarly to the previous. The first step differs mainly because the sample structure in MTJs is typically thicker, and to avoid overheating the sample with photoresist, the etching procedure is done with a few rests - usually 5 min etching with 1 min rest. It is worth noting that the observation with the mass spectrometer is very important, as it allows in the second step to know exactly when the tunnel barrier is. The second step is to make the pillars and grommets vias to the bottom electrode. As it needs as much accuracy and resolution as it can, this step is done with the Raith eLINE Plus electron beam lithography system. Negative photoresist (AR-N 7520.17) is placed on the sample and heated at 85°C for 2 min. The pillars are exposed using the 30 μ m aperture with a dose of 90 and the grommets with the 120 μ m aperture. After exposure, the chemical per (AR300-47) is used for 5 min. The etching procedure follows up to the tunnel barrier, and then Al₂O₃ is sputtered. Again, in order to remove the photoresist along with a part of oxide on the top of it, the sample is placed in Sigma with ultrasound at 70°C. The third step is exactly the same as in the two-step technique.

Bibliography

- N. Jones. *Nat.*, 561(163), 2018.
- James Prescott Joule. *The Royal Society Publishing*, 4, 1843.
- M. N. Baibich. *Phys. Rev. Lett.*, 61(2472), 1988.
- G. Binasch. *Phys. Rev. B*, 39(4828(R)), 1989.
- K. Jabeur et al. *World Academy of Science, Engineering and Technology*, 7(8), 2013a.
- S. N. Piramanayagam. *J. Appl. Phys.*, 102(011301), 2007.
- Jeongmin Hong et al. *Appl. Phys. Lett.*, 114(243101), 2019.
- J. C. Slonczewski. *JMMM*, 159(1-2):L1-L7, 1996.
- P.K. Amiri et al. *J. Appl. Phys.*, 113(013912), 2013b.
- L. You et al. *Proc. Natl. Acad. Sci. USA*, 112(10310), 2015.
- W.J. Kong et al. *Nat. Commun.*, 10(223), 2019a.
- V. Nabaie H. Heidari. *Magnetoresistive Sensors*. Wiley Online Library, November 2019. ISBN 9781119552215.
- S. Zuo et al. *Adv. Mat. Techno.*, 5(2000189), 2020a.
- T. Chen et al. *Proceedings of the IEEE*, 104(10):1919-1945, 2016a.
- M. Harder et al. *Phys. Rep.*, 661(0370-1573):1-59, 2016b.
- J. Holanda et al. *Phys. Rev Appl.*, 16:014051, 2021a.
- T. Takahashi et al. *AIP Advances*, 10(085218), 2020b.
- S. Sayed et al. *Appl. Phys. Lett.*, 118(0052408), 2021b.
- K. L. Wang et al. *IEEE Transactions on Nanotechnology*, 14(6):992-997, 2015a.
- K. Munira et al. *J. Appl. Phys.*, 120(203902), 2016c.
- A. E. Clark et al. *Phys. Rev. A*, 42(2), 1972.
- A. Singh et al. *JMMM*, 493(165737), 2020.
- A. J. Sellmyer et al. *Mat. Sci. and Eng. B*, 6(137-145), 1990.

- A. A. Kusov et al. *Phys. Rev. B*, 46(3123), 1992.
- H. Chiriac et al. *Phys. Rev. B*, 52(10104), 1995.
- A. Zhukov et al. *Nanos. Res. Lett.*, 7(223), 2012.
- AW. H. Meiklejohn and C.P. Bean. *Phys. Rev.*, 102(1413), 1956.
- AW. H. Meiklejohn and C.P. Bean. *Phys. Rev.*, 105(904), 1957.
- AW. H. Meiklejohn. *J. Appl. Phys.*, 33(1328), 2004.
- R. Engel-Herbert et al. *J. Appl. Phys.*, 97(074504), 2005a.
- J. L. O'Connell et al. *IEEE Transactions on Magnetism*, 56(1-8), 2020.
- P. Grünberg et al. *Phys. Rev. Lett.*, 57(2442), 1986.
- S. S. P. Parkin et al. *Phys. Rev. Lett.*, 64(2304), 1990.
- M.A. Ruderman and C. Kittel. *Phys. Rev.*, 96(99), 1954.
- T. Kasuya. *Prog. of Theor. Phys.*, 16(45), 1956.
- K. Yoshida. *Phys. Rev.*, 106(893), 1957.
- S.S.P. Parkin and D. Mauri. *Phys. Rev. B*, 44(7131(R)), 1991.
- J. E. Hirsch. *Phys. Rev. Lett.*, 83(1834), 1999.
- T.S. Ghiasi et al. *Nano Lett.*, 19(5959), 2019b.
- Y. Tserkovnyak et al. *Rev. of Mod. Phys.*, 77(1375), 2005b.
- J. C. Slonczewski. *Phys. Rev. B*, 39(6995), 1989.
- Y. Tserkovnyak et al. *Phys. Rev. Lett.*, 88(117601), 2002.
- E. H. Hall. *American Journal of Mathematics*, 2:287–292, 1879a.
- E. H. Hall. *Philosophical Magazine*, 12(157), 1879b.
- L. Berger. *Phys. Rev. B*, 2(4559), 1970.
- Y. Omori et al. *Phys. Rev. B*, 99(014403), 2019c.
- M. I. Dyakonov and V.I. Perel. *Phys. Lett. A*, 35(6):459–460, 1971.
- M. Ueda E. Saitoh and H. Miyajima. *Appl. Phys. Lett.*, 88(182509), 2006.
- V.M. Edelstein. *Solid State Comm.*, 73(233), 1990.
- Y. Du et al. *Phys. Rev. Appl.*, 13(054014), 2020a.
- W. Thomson. *Proceedings of the Royal Society of London*, 8(546-550), 1857.
- J. Hayakawa. *Appl. Phys. Lett.*, 89(232510), 2006.
- J.-P. Jan. *Solid State Phys.*, 5(1-96), 1957.

- R. Potter T. McGuire. *IEEE Transactions on Magnetics*, 11(4):1018–1038, 1975.
- H. Nakayama et al. *Phys. Rev. Lett.*, 110(206601), 2013c.
- Y. T. Chen et al. *Phys. Rev. B*, 87(144411), 2013d.
- M. Althammer et al. *Phys. Rev. B*, 87(224401), 2013e.
- J. Kim et al. *Phys. Rev. Lett.*, 116(097201), 2016a.
- G. Feher and E. A. Gere. *Phys. Rev.*, 114(1245-1256), 1959.
- Z. G. Yu. *Phys. Rev. B*, 77(205439), 2008.
- M. Isasa et al. *Phys. Rev. B*, 91(024402):7, 2015b.
- T. G. S. M. Rijks et al. *J. Appl. Phys.*, 76(1092), 1994.
- M. Julliere et al. *Phys. Lett.*, 51A(225), 1975.
- T. Miyazuki and N. Tezuka. *JMMM*, 139(L231-L234), 1995.
- J. S. Moodera et al. *Phys. Rev. Lett.*, 74(3273), 1995.
- J. Nogués and I. K. Schuller. *JMMM*, 192:203–232, 1999.
- J. Z. Sun. *Phys. Rev. B*, 62(570), 2000.
- M. Baumgartner et al. *Nat. Nanotech.*, 12(980), 2017a.
- S. Ikeda et al. *Nat. Mat.*, 9(721-724), 2010.
- L. Berger. *Phys. Rev. B*, 54(9353), 1996.
- E. B. Myers et al. *Sci.*, 285(867), 1999.
- I. M. Miron et al. *Nat.*, 476(189-193), 2011a.
- L. Liu et al. *Sci.*, 336(55), 2012.
- A. Manchon et al. *Nat. Mat.*, 14(871-882), 2015c.
- D. Jo et al. *Phys. Rev. B*, 98(214405), 2018.
- G. Géranton et al. *Phys. Rev. B*, 91(014417), 2015d.
- Y. A. Bychkov and E.I. Rashba. *JETP. Lett.*, 39(78), 1984.
- P. M. Haney et al. *Phys. Rev. B*, 87(174411), 2013.
- V. E. Demidov et al. *Phys. Rev. Lett.*, 107(107204), 2011b.
- S. Fukami et al. *Nat. Nanotech.*, 11(621), 2016b.
- H. Kurebayashi et al. *Nat. Nanotech.*, 9(211), 2014a.
- I. M. Miron et al. *Nat. Mater.*, 9(230), 2010a.
- L. Liu et al. *Phys. Rev. Lett.*, 106(036601), 2011c.
- J. Kim et al. *Nat. Mater.*, 12(240-245), 2013a.

- M. Hayashi et al. *Phys. Rev. B*, 89(144425), 2014b.
- C. Stamm et al. *Phys. Rev. Lett.*, 119(087203), 2017b.
- Q. Hao et al. *Phys. Rev. Appl.*, 3(034009), 2015a.
- K. Fritz et al. *Phys. Rev. B*, 98(094433), 2018a.
- D. MacNeill et al. *Nat. Phys.*, 13(300-305), 2017c.
- W. Skowroński et al. *Phys. Rev. Appl.*, 11(024039), 2019d.
- H. Liu et al. *J. Magn. Magn. Mater*, 358-359(233-258), 2014c.
- T. Devolder et al. *Appl. Phys. Lett.*, 108(172409), 2016c.
- M. Wang et al. *Nat. Electron.*, 1(582-588), 2018b.
- K. Garelo et al. *Appl. Phys. Lett.*, 105(212402), 2014d.
- K. Lee et al. *Appl. Phys. Lett.*, 102(112410), 2013b.
- S. Emori et al. *Nat. Mat.*, 12(611-616), 2013.
- W. Legrand et al. *Appl. Phys. Lett.*, 3(064012), 2015b.
- N. Mikuszeit et al. *Phys. Rev. B*, 92(144424), 2015c.
- L. Zhu et al. *Adv. Electron. Mater.*, 6(1901131), 2020b.
- J. H. E. Griffiths. *Nat.*, 158(670-671), 1946.
- E. Zavoisky. *Zhurnal Eksperimental'noi i Teoreticheskoi Fiziki*, 16(7), 1946.
- C. Kittel. *Phys. Rev.*, 73(155), 1948.
- L. D. Landau and E. Lifshitz. *Physikalische Zeitschrift der Sowjetunion*, 100(1243), 1935.
- T. Gilbert. *Phys. Rev.*, 8(153), 1955.
- S. Ziętek et al. *accepted for PRB. Arxiv*, 2202.00364, 2022a.
- D. Apalkov et al. *IEEE Trans. Magn.*, 46(2240-2243), 2010b.
- W. Skowroński et al. *Sci. Rep.*, 7(10172), 2017d.
- J. Kanak et al. *J. Appl. Phys.*, 113(023915), 2013.
- M. Kawaguchi et al. *Appl. Phys. Lett.*, 112(202405), 2018.
- A. Yamaguchi et al. *Phys. Rev. B*, 78(104401), 2008.
- P. T. Moseley and C.J. Seabook. *Acta Crystal.*, B29(1170), 1973.
- S. Serrano-Guisan et al. *J. Appl. Phys.*, 110(023906), 2011d.
- S. Karimeddiny et al. *Phys. Rev. Appl.*, 14(024024), 2020c.
- A. O. Avci et al. *Phys. Rev. B*, 90(224427), 2014e.

M.-H.Nguyen et al. *Phys. Rev. Lett.*, 116(126601), 2016d.

C. F. Pai et al. *Phys. Rev. B*, 92(064426), 2015d.

YT. Fan et al. *Sci. Rep.*, 12(2998), 2022b.

H .Yang et al. *Nat.*, 606(663), 2022c.

F. Trier et al. *Nat. Rev. Mat.*, 7(258), 2022d.